Sub-monolayer Deposited InGaAs/GaAs Quantum Dot Heterostructures and Lasers

Xu, Zhangcheng

Publication date:
2004

Document Version
Publisher's PDF, also known as Version of record

Citation (APA):
Xu, Z. (2004). *Sub-monolayer Deposited InGaAs/GaAs Quantum Dot Heterostructures and Lasers*. Technical University of Denmark.

Sub-monolayer Deposited InGaAs/GaAs Quantum Dot Heterostructures and Lasers

Thesis for the Doctor of Philosophy Degree
in Electrical Engineering

Zhangcheng Xu

Research Center COM (Communication, Optics and Materials),
Technical University of Denmark, DK-2800 Lyngby, Denmark

February 2004

Preface

This Ph. D. thesis is the summary of a material science project financed by the Danish Technical Research Council (STVF). The project is on “MBE growth and characterization of self-assembled semiconductor quantum dots”. The work presented in this thesis was mainly carried out at Research Center COM (Communication, Optics and Materials), Technical University of Denmark and III-V Nanolab, Niels Bohr Institute, Copenhagen University, under the principal supervision of Prof. Jørn M. Hvam, from February 2001 to February 2004. It is Prof. Jørn M. Hvam who offered me the opportunity of studying in the field of semiconductor science and technology. I am very grateful to him for his support, help and supervision.

In the beginning of this project, Dr. Claus Birger Sørensen taught me how to operate the Varian Gen II Molecular Beam Epitaxy system to grow III-V semiconductor compounds. Dr. Kristjan Leosson, Dr. Dan Birkedal and Prof. Vadim Lyssenko helped me with optical characterization techniques, including photoluminescence, photoluminescence excitation spectroscopy, and time-resolved photoluminescence. It was due to their help that I could start the project successfully. I greatly appreciate their help. Dr. Dan Birkedal is further acknowledged for his stimulated discussion and suggestions. I would like to thank Dr. Janusz Sadowski for the discussions on MBE growth, Mr. Nader Payami for his guidance in semiconductor process technique, Ms. Alexandra Boltasseva for her assistance in using E-beam lithography and Mr. Michael Juhl for his assistance in processing semiconductor lasers. I am also very thankful to Prof. Zongyan Zhao for his XRD measurements, and Dr. Kanjilal

Aloke for his TEM observations. Many other colleagues who helped me are also acknowledged.

Many thanks are given to Ms. Lone Bjørnstjerne and Ms. Aline Møller, who are the secretaries at COM, for their help during my stay in Denmark.

Finally, I am very grateful to my wife Qingxue, who has been accompanying and supporting me for many years.

Zhangcheng Xu

Zhangcheng Xu
Lyngby, Denmark
February 2004

Abstract

The fabrication, characterization and exploitation of self-assembled quantum dot (QD) heterostructures have attracted much attention not only in basic research, but also by the promising device applications such as QD lasers. The Stranski-Krastanow (SK) growth and the submonolayer (SML) deposition are two different methods of growing self-assembled QDs. In the case of SK growth, which has been widely used for lattice mis-matched materials, such as In(Ga)As/Ga(Al)As, coherent three dimensional (3D) islands form on top of a wetting layer to relax the strain energy. However, in the case of SML deposition, the deposition of a short-period InAs/GaAs superlattice on a GaAs (100) surface, with an InAs effective thickness of less than 1 monolayer (ML), results in the formation of nanometer scale (In,Ga)As QDs of a non-SK class.

In this thesis, the SML InGaAs/GaAs QDs are formed by 10 cycles of alternate deposition of 0.5 ML InAs and 2.5 ML GaAs. The growth, structure, and optical properties of SML InGaAs/GaAs QD heterostructures are investigated in detail. SML InGaAs/GaAs QD lasers lasing even at room temperature have been successfully realized. The gain properties of SML InGaAs QD lasers are studied.

The growth temperature of SML InGaAs/GaAs QDs in one sample was as low as 480 ^{o}C. Plan-view transmission electron microscopy observation shows that SML QDs are slightly elongated along the [1 –1 0] crystal direction, and the QD density is extremely high (> 10^{11} cm^{-2}). By using lower temperature micro-photoluminesence (PL), selective PL with excitation energy below the GaAs band gap, the temperature-dependent PL, ***for the first time, the***

SML InGaAs/GaAs QD heterostructure is verified to be a quantum-dot-quantum-well structure, i.e., the Indium rich QDs are embedded in a lateral quantum well (QW) with lower Indium content. This conclusion was further confirmed in the high-resolution x-ray diffraction analysis, which shows that the vertical lattice mismatch of the InAs monolayer with respect to GaAs is around 1.4%, while the lattice mismatch in the QW is negligible. As the temperature increases, a sigmoidal behavior of the PL peak energy and a narrowing of the PL linewidth of the SML QD ensemble are observed, and explained by carrier transfer from smaller dots to larger dots via QW states. At room temperature, the PL signal of QDs quenches due to the thermal escape of carriers from QD to QW states. In the edge geometry, strong contribution of the TM mode to PL signal has been observed, indicating the vertical coupling of the SML InAs islands in the GaAs matrix. The PL rise time (~ 35 ps) and decay time (~ 700 ps) of the ground states of SML QDs, at 5 K, are found to be comparable to those of typical SK QDs.

The SML InGaAs/GaAs QDs in another sample was grown at 500 ^{o}C. For this sample, the PL signal of QD ground states is still observable even at room temperature. Furthermore, strong contribution of the TM mode to PL signal is also observed in the edge geometry, at room temperature. In our SML InGaAs/GaAs QD lasers, the growth conditions of QDs are the same as those of this sample.

The lasing wavelength, the threshold current density, and the characteristic temperature of a SML InGaAs/GaAs QD broad area laser with a 628 μm-long cavity and a 100 μm-wide stripe, are 965 nm, 373 A/cm^2 and 81 K, respectively, at 30 ^{o}C. The gain spectra at 30 ^{o}C were measured, by using the Hakki-Paoli method. It is found that ***the maximum modal gain of QD ground states is 43.9*** cm^{-1}***, which is the highest value obtained for a single sheet of self-assembled In(Ga)As/GaAs QDs, to the best of our knowledge.*** Furthermore, no gain saturation takes place below the threshold at the lasing wavelength, and the gain spectrum becomes symmetric with respect to the lasing wavelength when the injection current is about 0.98 I_{th} . The zero linewidth-enhancement-factor at the lasing wavelength has been observed, when the injection current is about 0.98 I_{th}. ***This is the first time for the zero linewidth- enhancement-factor to be observed for a QD laser.*** These properties are attributed to the high density and the high uniformity of SML QDs in our laser diodes, which are very useful for the application of SML QDs in high power lasers or vertical cavity surface emitting lasers.

Contents

Chapter 1 Introduction

A semiconductor quantum dot (QD) represents a semiconductor crystal with a size comparable to the Bohr radius of an electron-hole pair (excition), ranging from several nanometers to tens of nanometers, coherently inserted in a larger bandgap semiconductor matrix. In QDs, the carriers (electron or holes) are confined three-dimensionally, which results in the discrete energy states for carriers. The QDs are often referred to as "artificial atoms", due to their delta-function-like density of states. QDs present the utmost challenge and point of culmination of semiconductor physics [1]. Semiconductor lasers with a uniform array of QDs as the active medium, are called QD lasers.

In 1982, Arakawa and Sakaki theoretically predicted that, the delta-function-like density of states and the enhanced overlap of electron and hole wavefunction in a QD may result in decreased threshold current densities, higher temperature stability of the threshold current, as well as higher material and differential gain, for a QD laser [2]. In 1986, Aseda et al. derived the basic theory of the gain characteristics of QD lasers and predicted a decreased linewidth enhancement factor (LEF), which is responsible for the wavelength chirp under injection current modulation [3]. After these predictions, two approaches have been tried to realize QD lasers. The first one is a precise patterning technique. It involves patterning of quantum wells by etching and overgrowth on patterned structure, or selective growth on a patterned substrate [4,5]. In 1994, Hirayama et al. realized InGaAs-InGaAsP QD lasers by using e-beam lithography and etching techniques [5]. However, the threshold current density was as high as 7.6 kA/cm^2 even at 77 K. In this approach, the nonradiative recombination, especially at the surface of etched sidewalls where the active region is exposed to air, severely limits laser performance. The second approach is self-organization of quantum dots during highly strained heteroepitaxy, which has been very successful. In 1994, Kirstaeder et al. reported the first demonstration of InAs-GaAs QD laser grown in the Stranski-Krastonow (SK) mode [6]. At 77 K, the threshold current density for a 1 mm cavity length and uncoated facets was 120 A/cm^2. A large characteristic temperature $T_0 = 350$ K between 50 and 120 K was found. Since the first demonstration of SK QD lasers, further improvements have been achieved, which are summarized in a recent review paper by D. Bimberg and N. Ledentsov [7]. In the SK growth mode, which has been widely used for lattice mis-matched materials, such as In(Ga)As/Ga(Al)As, coherent three-dimensional (3D) islands form on top of a wetting layer to relax the strain energy. Another way of growing self-organized QDs is sub-monolayer (SML) deposition [8]. In this case, the deposition of a short-period InAs/GaAs superlattice on a GaAs (100) surface, with an InAs effective thickness of less than 1 monolayer (ML), results in the formation of nanometer scale (In,Ga)As QDs of a non-SK class [9,10,11]. High power lasers with the stacked SML InAs/GaAs QDs as the active region have recently been demonstrated [10,11,12]. The structure, optical properties and carrier dynamics of SK InGaAs/GaAs QDs have been intensively studied [1], but few papers have been reporting on SML InGaAs/GaAs QDs [13]. In addition, the gain properties of SML InGaAs/GaAs QD lasers have not been reported until now.

The focus of this thesis is to investigate the structure, optical properties and carrier dynamics of SML InGaAs/GaAs QDs and to study the gain properties of SML InGaAs/GaAs QD lasers. Chapter 2 introduces the MBE growth of self-assembled InGaAs/GaAs quantum dots either in the SK mode or by SML deposition. The structure of SML InGaAs/GaAs QDs grown at low temperature is analyzed by using transmission electron microscopy and high-resolution x-ray diffraction, in Chapter 3. In Chapter 4, the optical properties and carrier dynamics of SML InGaAs/GaAs QDs grown at low temperature are presented. The optical characterization of SML InGaAs/GaAs quantum dots grown at high temperature is given in Chapter 5. The characterization and the gain properties of SML InGaAs/GaAs QD lasers are presented in Chapter 6. Finally, the main results presented in this thesis will be summarized.

Chapter 2 Molecular Beam Epitaxy Growth of Self-Assembled InGaAs/GaAs Quantum Dots

In this chapter, molecular beam epitaxy (MBE) growth of self-assembled InGaAs/GaAs quantum dots (QDs) either in the Stranski-Krastow (SK) mode or by sub-monolayer (SML) deposition, will be introduced.

2.1 Molecular Beam Epitaxy

2.1.1 Basics of Molecular Beam Epitaxy

The word epitaxy designates the adsorption of one crystal by another, with a well-defined relative orientation of the two crystals. Among all the advanced semiconductor growth techniques, MBE provides the greatest ease of growing complex semiconductor multilayer structures with a precise control of the thickness (up to the monolayer scale accuracy), the composition of the involved layers [14]. Since its conception in the 1960s [15,16], MBE has experienced a tremendous development. Nowadays, the field of MBE includes the growth of group IV, III-V and II-VI semiconductors, metals, magnetic materials, nitrides, oxides and fluorides using solid and gasous as well as metal-organic sources. In this technique, growth proceeds under ultrahigh vacuum conditions by the condensation of thermal energy molecular beams on an underlying single-crystal substrate. Generally, the deposited film adopts as far as possible the orientation and crystallographic characteristics of the substrate. As a matter of fact, when thermal atoms or molecules arrive on a substrate, they diffuse until they reach an adequate crystallographic site where they can be incorporated.

In the case of growing III-V compound via MBE, the substrate temperature and the V/III ratio are chosen in such a way that the growth rate is controlled by the group-III element incorporation rate (close to one), the group-V element being incorporated only if chemically reacting with group III-elements. Thus, increasing the group-III element deposition rate increases the growth velocity. On the other hand, an increase of the V-element beam rate decreases the surface diffusion constant. In this case, the choice of a particular V/III ratio associated with a particular substrate temperature corresponds to the choice of particular growth kinetics. Since the group V element evaporates when it is not at once incorporated, the MBE growth of III-V compounds can be described with a reasonable approximate by models in which atoms of a single species are considered [17-19]. This species is the group III element, whose deposition and diffusion on the surface determines the growth rate and the type of growth.

The merit of MBE is the possibility to prepare a wide range of III-V semiconductor materials [20], with tailor-made lattice constants or electronic properties. For instance, in a ternary compound $A_xB_{1-x}C$, the choice of x allows for tuning the lattice constant so as to make possible epitaxy on a given substrate. In addition to the lattice constant, one can tune the electronic band gap in order to obtain the desired optic or electronic properties.

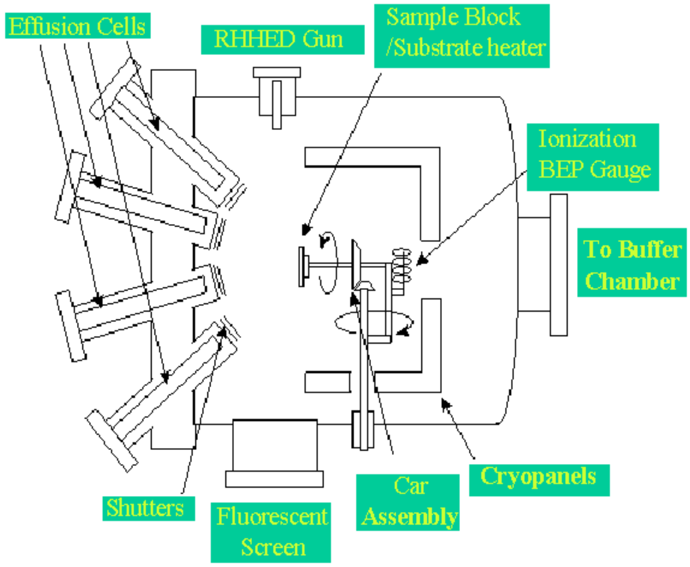

(a)

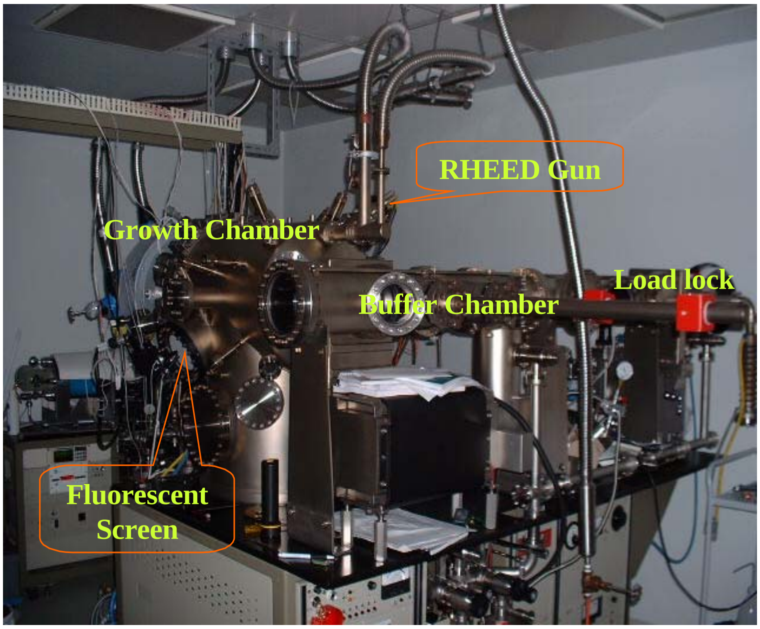

(b)

Fig. 2.1 (a) Diagram of a typical MBE system growth chamber; (b) Varian GEN II MBE system, at Niels Bohr Institute, Copenhagen University.

The main components of an MBE system are shown in Fig. 2.1 (a). The source materials, in elemental form, are evaporated from the liquid or sublimed from the solid phase. The sources are electrically heated with a temperature stability of typically 0.1^{o}C. The molecular and atomic beams can be switched on and off by shutters in front of the crucibles, which are actuated by computer-controlled motors. The Varian Gen II MBE system at Niels Bohr Institute (NBI), Copenhagen University consists of three main vacuum chambers: a growth chamber, a buffer chamber and a load lock, as shown in Fig. 2.1 (b). The load lock is used to bring samples into and out of the vacuum environment while maintaining the vacuum integrity of the other chambers. The buffer chamber is used for preparation and storage of samples. Samples are loaded onto the growth chamber sample holder/heater via a magnetically coupled transfer rod. The sample holder is flipped around from the loading position so that the sample faces the material sources. For improved layer uniformity, the sample holder is designed for continual azimuthal rotation of the sample, and is thus commonly termed the ‘CAR’. The CAR also has an ion gauge mounted on the side opposite the sample which can read the chamber pressure, or be placed facing the sources to measure beam equivalent pressure (BEP) of the material sources. A liquid nitrogen cooled cryoshroud is located between the chamber walls and the CAR and acts as an effective pump for many of the residual gasses in the chamber. Two cryopumps are used to remove gasses which aren’t pumped by the cryopanels. This pumping arrangement can keep the partial pressure of undesired gasses, such as H_2O, CO_2, and CO to less than $\sim 10^{-11}$ Torr. The substrate holder and all other parts that are heated are made of materials such as Ta, Mo, and pyrolytic boron nitride (PBN) which do not decompose and our gas impurities even when heated to 1400 ^{o}C. To monitor the residual gasses, analyze the source beams, and check for leaks, a quadrupole mass spectrometer (QMS) is mounted in the vicinity of the CAR.

The sources in the NBI Varian Gen II system are designed specially to grow GaAs and other arsenic containing compound semiconductors. The system contains cells for As, Ga, Al, In, Be (p-doping), and Si (n-doping). The arsenic source in our system is a valved cracker [21], in which the flux from a heated As ingot is controlled with a valve. After passing through the valve, the As flux moves through a cracking tube which converts the molecular species from As_4 to As_2. One of the primary reasons for using As_2 instead of As_4, is to reduce the consumption of As, since As_2 incorporates more efficiently into GaAs. It has been suggested that using As_2 should result in better crystal growth since the incorporation mechanism is simpler than for As_4 [22].

2.1.2 Reflection High Energy Electron Diffraction

One of the most useful tools for *in-situ* monitoring of the growth is reflection high energy electron diffraction (RHEED). It can be used to calibrate growth rates, observe removal of oxides from the surface, calibrate the substrate temperature, monitor the arrangement of the surface atoms, determine the proper arsenic overpressure, give feed back on surface morphology, and provide information about growth kinetics. At typical growth temperatures, the surface atoms of an As terminated (100) GaAs layer rearrange themselves into a what is called a (2×4) reconstruction. RHEED images with the electron beam pointed along the $[011]$ and $[01\bar{1}]$ crystal directions are shown in Fig. 2.2. The appearance of the RHEED diffraction pattern can be used to provide qualitative feedback on surface morphology. If the surface is smooth, then the RHEED diffraction patterns appear streaky, similar to what is seen in Fig. 2.2. If the samples are rough, then the streaks are more 'spotty' and diffraction pattern is not as clear. An amorphous surface, such as an oxide layer, shows a haze instead of a diffraction pattern and polycrystalline surface results in rings circling the straight-through beam. Such information, although only qualitative, can be a useful check of the surface condition. In addition, RHEED intensity oscillations can be used as an accurate, quick, direct measure of the growth rate in MBE. The oscillation frequency corresponds to the monolayer growth rate [23]. In the case of growing 3-dimensional QDs in the SK mode, RHEED is very useful for monitoring the formation of QDs.

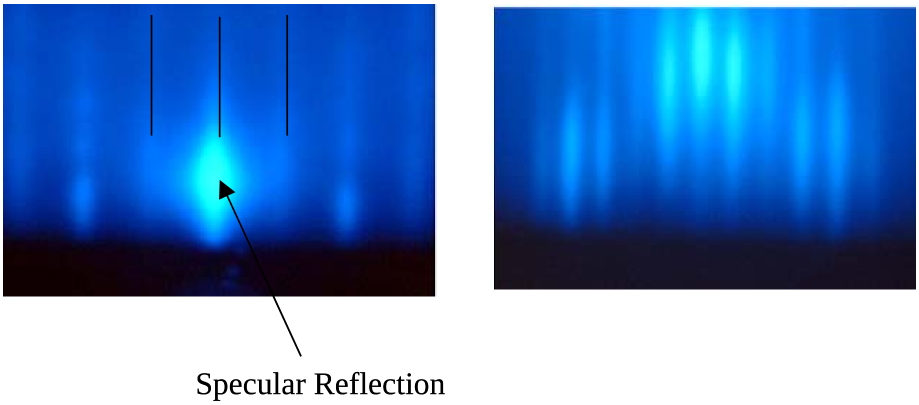

a) '2×' pattern (b) '4×'pattern

Fig. 2.2 Images on the RHEED screen with the electron beam pointed along the $[011]$ (a) and $[01\bar{1}]$ (b) directions on an As-terminated GaAs surface at 600 ^{o}C. The voltage is 12 kV.

2.2 Growth of Quantum Dots in the Stranski-Krastonow Mode

As we know, there are three modes of heteroepitaxial growth: Frank-van der Merwe (FM), Volmer-Weber (VW) and Stranski-Krastonow. They represent layer-by-layer growth (FM, 2D), island growth (VW, 3D), and layer-by-layer plus island growth (SK), as shown in Fig. 2.3. The particular growth mode for a given system depends on the interface energies and on the lattice mismatch. For a strained epilayer with small interface energy, initial growth may occur layer by layer, but a thicker layer has large strain energy and can lower its energy by forming isolated islands in which strain is relaxed. Thus the SK growth mode occurs. For many material systems the island formation is preferred to dislocation formation [24]. However, when the critical layer thickness is only slightly exceeded, dislocation-free islands (dots) can be formed. Experiments on InAs/GaAs (001) [25] and on Ge/Si(001) [26,27] have demonstrated the formation of three-dimensional coherently strained islands. In the beginning of our project, we succeeded in growing InGaAs/GaAs QDs via the SK growth mode.

During the formation of SK QDs, the RHEED pattern will change from streaky into spotty, as shown in Fig. 2.4. When the incident electron beam points along the $\left[1\bar{1}0\right]$ direction, RHEED pattern of QDs shows pairs of streaks known as chevrons (or alternatively as arrowheads). However, when the incident electron beam points along the $\left[110\right]$ direction, RHEED pattern shows only spots. This difference originates from the structure anisotropy of QDs.

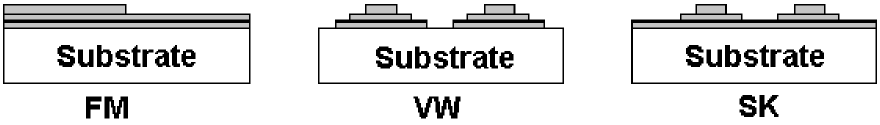

Fig. 2.3 Schematic diagrams of the three possible growth modes: Frank-van der Merwe (Fvdm), Volmer-Weber (VW), and Stranski-Krastanow (SK).

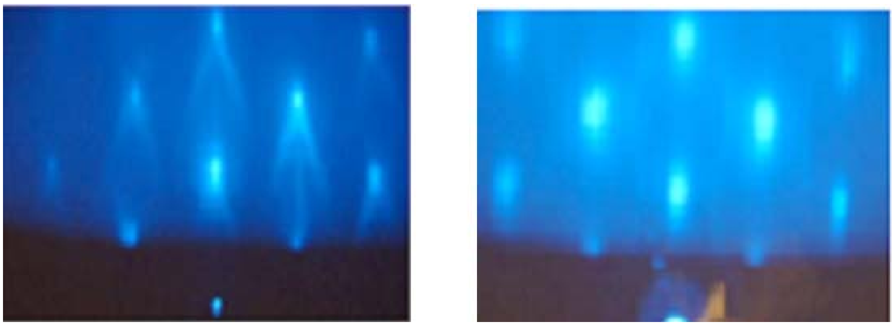

Fig. 2.4 RHEED patterns from approximately 6.1 ML of $In_{0.6}Ga_{0.4}As$ on GaAs (0 0 1): (left) $[1\bar{1}0]$ azimuth; (right) $[1\,1\,0]$ azimuth (12 kV beam). Substrate temperature was set to be 500 °C.

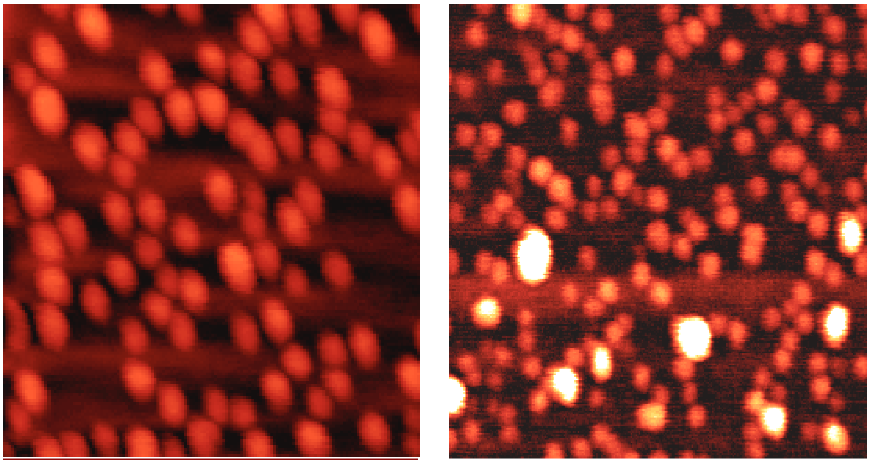

(a) (b)

Fig. 2.5 AFM images of SK InGaAs QDs on: (a) GaAs surface at 500 ^{0}C; (b) GaAs surface at 485 ^{0}C. Each image corresponds to an area of $(500\times 500)nm^2$.

The final structure, size and composition of QDs strongly depends on the growth conditions, such as growth rate, substrate (material, temperature and orientation), and deposition amount, etc.[28] Fig. 2.5 shows the AFM images of 6.1 ML of $In_{0.6}Ga_{0.4}As$ QDs grown on GaAs surface at 500 ^{0}C (a), at 485 ^{0}C (b). It can be seen that the QDs are larger while the density is lower when the growth temperature is higher, in agreement with the results in Ref. 29.

Nowadays, a main part of the research on quantum dots is performed on SK QDs. The application of SK QDs enables the realization of low-threshold high-CW-power GaAs-based lasers [30].

2.3 Growth of Quantum Dots by Sub-monlayer Deposition

Another way to fabricate self-assembled QDs has been proposed by using sub-monolayer narrow gap insertion in traditional III-V materials systems [9,31,32]. It is shown that such islands having a height of 1 ML provide a uniform size (width of about 4 nm for InAs elongated islands on GaAs (100) substrate) [9]. The formation of ordered structures on crystal surfaces has been shown to occur when two phases with different values of intrinsic surface stress (τ_{ij}) are coexisting on the surface [33]. For strained above-monolayer-high 2D island having a two-dimensional shape the total energy minimum for particular island size always exists as it was stressed [34].

In the case of stacked arrays of 2D nano-islands it was predicted that correlated growth prevail at small spacer layer thicknesses, while anticorrelated growth occur for thicker spacer [35]. This effect has been observed experimentally using processed high-resolution transmission electron microscopy [36]. The sequence of SML InGaAs/GaAs quantum dots formation is schematically shown in Fig. 2.6 [11]. The evolution of RHEED pattern during the growth of SML InGaAs/GaAs QDs is shown in Fig. 2.7. The spotty pattern as in the SK mode can not be observed, though the RHEED pattern becomes unclear after 0.5 ML InAs and 2.5 ML GaAs are alternately deposited for 10 times. As the density of quantum dots can be much higher in the case of SML deposition than that in the SK mode, SML QD arrays may be used in high power lasers, or low finesse vertical cavity surface emitting lasers (VCSELs), and in other applications [13].

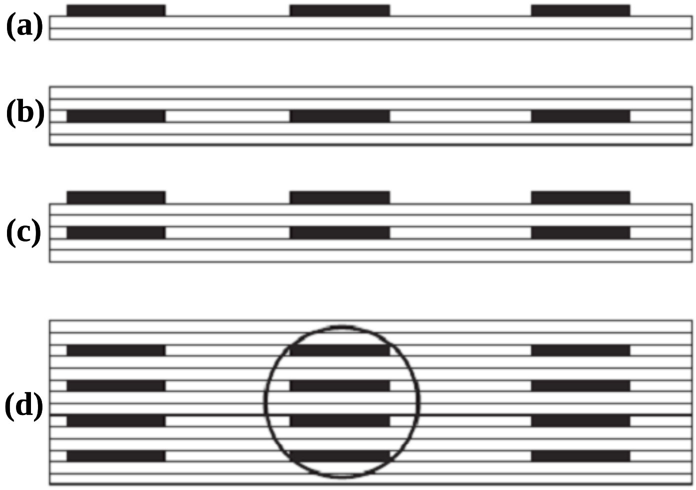

Fig. 2.6 Scheme of SML quantum dot formation: (a) deposition on InAs (<1 ML) on GaAs to give 1 ML high islands, (b) flat surface after deposition of several ML thick GaAs cap, (c) vertical correlation of InAs islands, (d) InGaAs QDs formed by SML deposition.

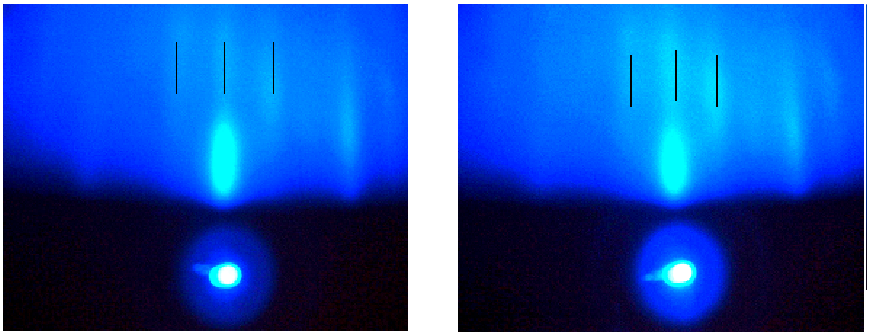

(a) (b)

Fig. 2.7 RHEED patterns during the formation of SML InGaAs/GaAs quantum dots, (a) after growing 0.5 ML InAs on GaAs surface. (b) after growing 2.5 ML GaAs on 0.5ML InAs. The electron beam is incident onto the surface along the $[110]$ azimuth. The substrate temperature is set to be 480 °C.

2.4 Summary

SML deposition is an alternative approach to the widely used SK mode of growing self-assembled QDs. Ultra-dense QD arrays formed by SML deposition are quite useful for the application of QDs in high power laser diodes. Compared with SK QDs, SML QDs, especially the stacked SML QDs have not been studied intensively. In the next chapters, the structure and optical properties of SML InGaAs/GaAs QDs will be studied in detail.

Chapter 3 Structure Characterization of Sub-monolayer InGaAs/GaAs Quantum Dots Grown at Low Temperature

In this Chapter, the structure of sub-monolayer (SML) InGaAs/GaAs quantum dots (QDs) grown at low temperature, will be investigated by using plan-view transmission electron microscopy (TEM) and high-resolution x-ray diffraction (HRXRD).

3.1 Sample Growth

The SML InGaAs/GaAs QD sample (HCØ737) was MBE-grown on a semi-insulating GaAs (001) substrate. After oxide desorption, a 500 nm GaAs buffer layer, 20 nm AlAs, and 82 nm GaAs were grown at 600 ^{0}C. After the substrate temperature was lowered to 480 ^{0}C, 10 cycles of InAs(0.5ML)/GaAs(2.5ML) were deposited to form an SML QD layer, with 2 nm of GaAs covering the SML QD layer. Then the substrate temperature was again increased to 600 ^{0}C to grow 20 nm of AlAs and a 106 nm GaAs cap layer.

3.2 TEM Observation

TEM studies were performed using a Philips CM20 instrument operating at 200 keV, at Department of Physics, University of Aarhus, Denmark. Fig.3.1 shows a plan-view TEM image of the SML InGaAs/GaAs QDs. The contrast is mainly due to strain fields. 10% of the surface is covered by QDs and the area density of QDs is around $5.2 \times 10^{11} cm^{-2}$, much higher than the conventional SK InAs/GaAs QDs [28]. Most of the QDs are slightly elongated along $[1\bar{1}0]$ direction, and the size of QDs is around 5 – 10 nm in diameter. However, the actual QD size could be smaller since the strain field may extend beyond the QD boundary.

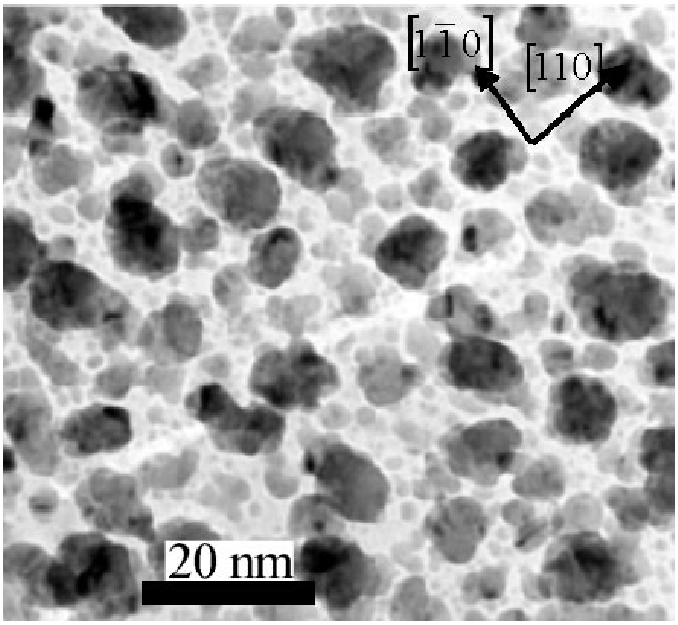

Fig. 3.1 (011) bright field plan-view TEM image of the structure with SML InAs/GaAs QDs.

3.3 X-ray Diffraction Characterization

The determination of the strain in QDs is useful not only for understanding the QD growth but also for the calculation of the energy diagram of QDs[28,37,38]. HRXRD is an important non-destructive method of determining the interface morphology and the strain of buried films. The measured rocking curves are the "fingerprints" of the investigated structure and can be analyzed by using the dynamical x-ray diffraction theory, i.e., the Tagaki-Taupin equations [39,40] .

3.3.1 Experimental Set-up

The HRXRD rocking curve near the (004) reflection peak of GaAs (001) substrate was measured using a MAC Science HRXRD instrument with a Cu Kα x-ray source and a Ge (004) monochromator (perfect crystal), at Department of Physics, Anhui University, China. The experimental setup is shown in Fig. 3.2. The X-rays from the source are first monochromated by the Ge (004) monochromator and then incident to the QD sample, which is mounted onto a high-resolution goniometor. The diffracted beam is detected by a scintillation counter.

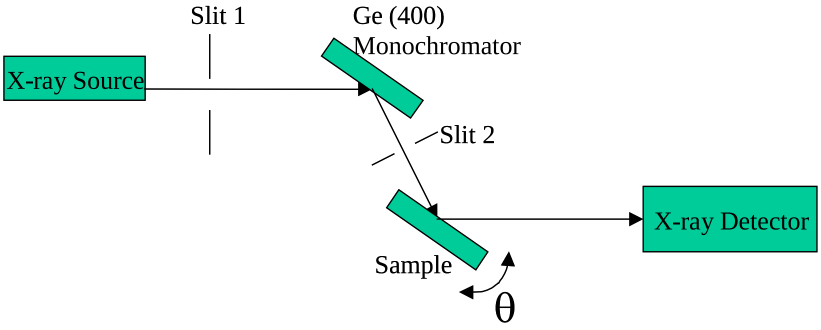

(a)

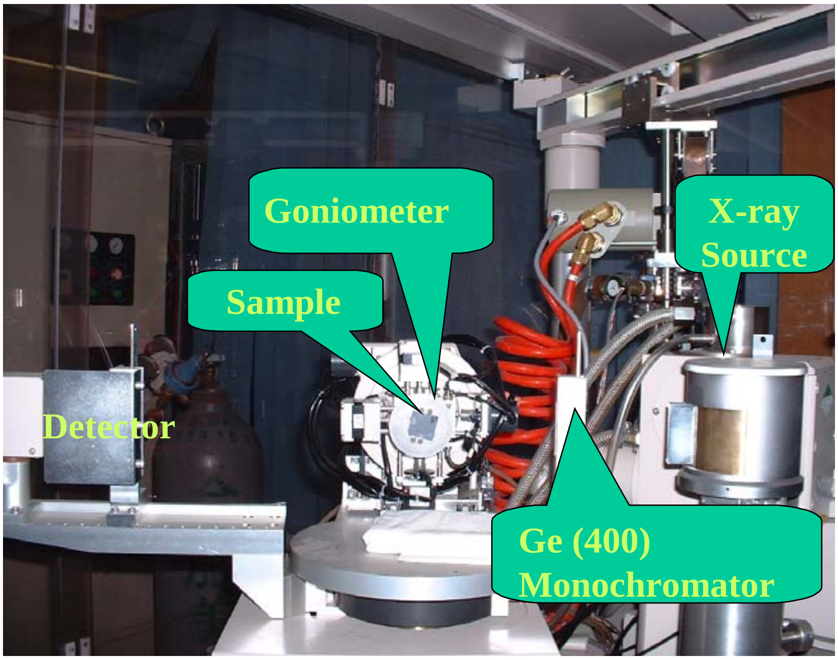

(b)

Fig. 3.2 (a) Setup for high-resolution XRD measurements; (b) The high-resolution XRD instrument at Department of Physics, Anhui University, China.

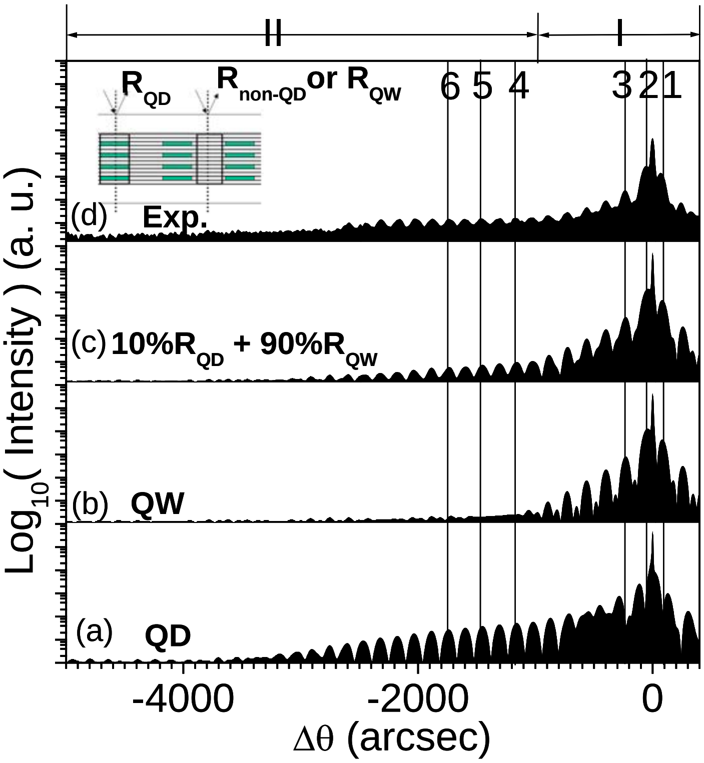

Fig. 3.3 High resolution X-ray diffraction rocking curves in the vicinity of the GaAs (004) refection, (a) the simulated curve of R_{QD}, assuming $a^{\perp}_{InAs} = 5.7324\AA$; (b) the simulated curve of R_{QW}, assuming $a^{\perp}_{In_{0.15}Ga_{0.85}As} = 5.6533\AA$; (c) the combination of (a) and (b), assuming the QD coverage percentage is 10%; (d) the experimental data. The curves are shifted vertically for clarity. The inset shows the different contributions from the QD parts and the lateral non-QD parts to the reflection coefficient of an SML QD sample. The lines 1 to 6 are the guides for the eye.

3.3.2 Results and Discussion

Due to the structural complexity of a QD heterostructure, the average strain of the QD plane rather than of the QDs themselves has been determined for the SK QDs[41,42]. In the case of the SML QDs, the contribution from the QD parts and the lateral non-QD parts to the finally measured reflection rocking curve can be considered separately, as shown in the inset of Fig. 3.3. According to the growth mechanism of stacked SML InGaAs QD heterostructure [11], the SML QD in our sample can be described as 10 cycles of GaAs(2ML)/InAs(1ML), while the lateral non-QD part can be described as a 30 ML GaAs and 50% of the surface should be covered by the SML QDs. However, QDs only fill about 10% of the surface in the plan-view TEM image (Fig. 3.1). This means that 40% of the SML InAs is in the lateral non-QD part, possibly due to In-Ga intermixing or because vertical correlation does not occur for all the SML QDs. Therefore, the lateral non-QD part is an InGaAs alloy rather than pure GaAs, and our sample is a quantum-dot-quantum-well (QDQW) heterostructure. The average In composition in the lateral QW is calculated to be around 15%, according to the 10% QD coverage on the surface.

Fig. 3.3 shows the experimental data and simulated results based on Tagaki-Taupin equations. The total reflection coefficient $R(\Delta\theta)$ of the sample can be written as:

$$R(\Delta\theta) \approx xR_{QD}(\Delta\theta) + (1-x)R_{QW}(\Delta\theta), \tag{1}$$

where $\Delta\theta$ is the angular deviation from the Bragg angle of the (004) peak of the GaAs substrate, x is the QD coverage percentage on the surface, $R_{QD}(\Delta\theta)$ and $R_{QW}(\Delta\theta)$ are the reflection coefficients from the part of the sample with only the SML QDs and the part with only the lateral QW, respectively. Note that Eq. (1) is valid only when $xR_{QD}(\Delta\theta)$ is so small that the multiple scattering of x-rays between the QD and the QW parts is negligible. In the angular range from –1000 to +500 acrsecs (Range I), the reflectivity is much higher than outside this range and mainly depends on the $R_{QW}(\Delta\theta)$ because QW covers 90% of the surface. Only when the lattice mismatch is negligible between the lateral 8.48 nm $In_{0.15}Ga_{0.85}As$ QW and GaAs, do the calculated interference fringes (curve b, lines 1 to 3) match the experimental ones in Range I. At the same time, no inference fringes in the range from –1000 to –4000 (Range II) in curve b can be comparable to the experimental data. Therefore, the interference fringes in Range II are mainly from $R_{QD}(\Delta\theta)$. By varying the lattice constant $a^{\perp}_{InAs}$ of the InAs monolayer inside the SML QDs, $R_{QD}(\Delta\theta)$ is calculated and found to match the interference fringes (curve a, lines 4 to 6) only when $a^{\perp}_{InAs} \approx 5.7324\AA$, i.e. $a^{\perp}_{InAs}$ is around 1.4% higher than the lattice constant of GaAs. With $x = 10\%$ determined from the TEM image (Fig. 3.1), curve c) is calculated from Eq. (1). It can be seen that all the interference fringes in curve c) can match the experimental ones very well. The macroscopic continuum elasticity theory (MCET) predicts that for a pseudomorphic InAs layer buried in GaAs (001), the strain normal to the (001) plane would be 7.26%, corresponding to $a^{\perp}_{InAs} \approx 6.4981\AA$ [43,44]. However, the validity of the MCET in the monolayer limit is a long debated issue [45-47]. In the case of SML InGaAs QDs, the InAs islands with 1ML in height and around 5-10 nm in diameter are surrounded by a GaAs matrix, and the MCET cannot be applied directly. Our HRXRD gives an experimental determination of the strain in the SML InGaAs QDs.

3.4 Conclusions

The structure of SML InGaAs/GaAs quantum dots, are studied by using plan-view TEM and HRXRD. The HRXRD (004) rocking curve was simulated using the Tagaki-Taupin equations. Excellent agreement between the experimental curve and the simulation is achieved assuming that Indium-rich SML QDs are embedded in a quantum well (QW) with lower Indium content and an observed QD coverage of 10%. In the SML QDs, the vertical lattice mismatch of the InAs monolayer with respect to GaAs is around 1.4%, while the lattice mismatch in the QW is negligible. The optical properties and carrier dynamics of SML InGaAs/GaAs QDs grown at low temperature will be studied in Chapter 4.

Chapter 4 Optical Properties and Carrier Dynamics of Sub-monolayer InGaAs/GaAs Quantum Dots Grown at Low Temperature

In this chapter, the optical properties of SML InGaAs/GaAs QDs grown at low temperature (Sample HCØ737) will be investigated by using low-temperature micro-Photoluminescence (PL), selective PL at different excitation energies, temperature-dependent PL, and polarization-dependent PL, with continuous-wave (CW) excitation sources. The carrier capture to and recombination in the SML QDs are studied by using time-resolved (TR) PL.

4.1 Continuous-wave Photoluminescence

4.1.1 Experimental set-up

The experimental set-up for CW PL measurements in the back-scattering geometry is shown in Fig. 4.1(a). The sample is mounted in a closed-cycle He cryostat and the temperature of the sample can be tuned from 10 K to 300 K. A He-Ne laser at the wavelength of 632.8 nm or a Ti-Sapphire laser is used as the excitation source. The Ti-Sapphire laser is pumped by an Ar^+ laser, and the wavelength can be tuned from 700 nm to 950 nm. The PL signal is dispersed by a 0.65-meter spectrometer and detected with a Peltier-cooled Si CCD. An attenuator is used to adjust the intensity of the incident laser beam.

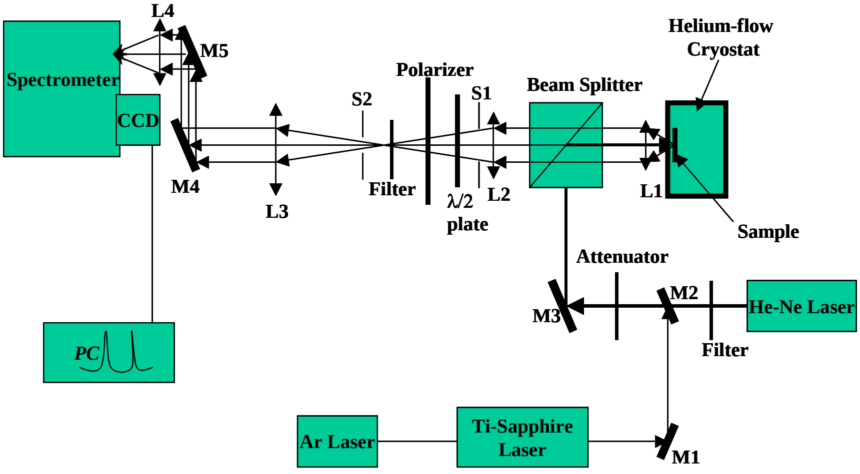

(a)

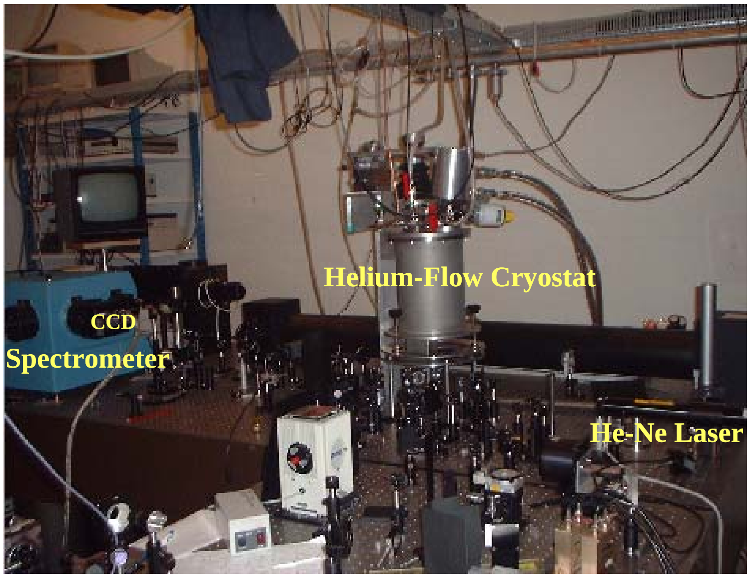

(b)

Fig. 4.1 (a) The experimental set-up for CW PL experiments in the back-scattering geometry, M1 ~ M5 are mirrors, L1 ~ L4 are lenses, S1 and S2 are small holes used to limit the collection angle of PL; (b) The instruments for CW PL experiments at Research Center COM, Technical University of Denmark.

A half-wavelength plate and a polarizer are used to investigate the polarization properties. Fig. 1(b) shows the CW PL instruments at Research Center COM, Technical University of Denmark.

4.1.2 Low Temperature Micro-Photoluminescence

4.1.2.1 Excitation-Power Dependence

Three-dimensional (3D) confinement of excitons in a QD produces discrete emission spectra [48]. This property was used to confirm the formation of QDs in our sample, with low-temperature micro-photoluminescence. For the μPL experiments, Lens L1 in Fig. 4.1(a) was put inside the cryostat and the focus size is only 2 μm in diameter. A He-Ne laser at the wavelength of 632.8 nm is used for excitation. The μPL spectra of the sample at 10 K are depicted in Fig. 4.2. At a low excitation intensity of 0.382 kW/cm^2, sharp emission lines can be seen in the broad PL band centered at 1.26 eV. The individual sharp emission lines give direct evidence of the delta-function-like discrete density of states in QDs. As the excitation density increases, the high-energy side of the broad μPL band becomes smoother than the low energy side, gradually a peak centered at 1.326 eV dominates the whole PL band. As will be discussed Section 4.1.3 and 4.1.4, this peak is attributed to the QW states.

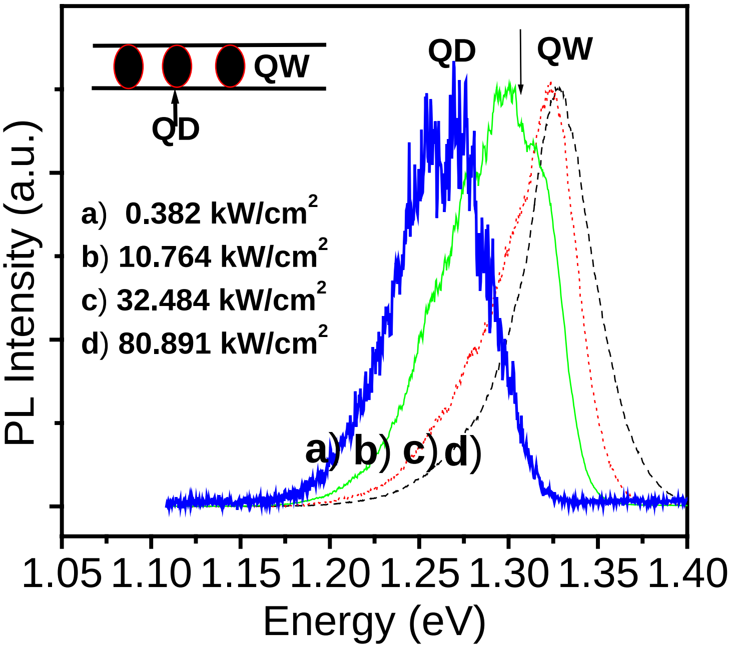

Fig 4.2 μPL spectra of the SML-grown InGaAs/GaAs quantum dots at 10 K, at different excitation intensities (a) 0.381 kW/cm^2, (b) 10.764 kW/cm^2 , (c) 32.484 kW/cm^2 , (d) 80.891 kW/cm^2 . The PL intensities are normalized to facilitate comparison.

Fig. 4.3 shows the PL intensity behaviour with respect to the excitation power density. The PL intensity at 1.26 eV increases with the increase of the excitation density but the slope gradually decreases, due to the limited density of states of QDs. However, the PL intensity at 1.326 eV increases almost linearly with the increase of excitation power and no saturation of the slope can be found, indicating higher density of states.

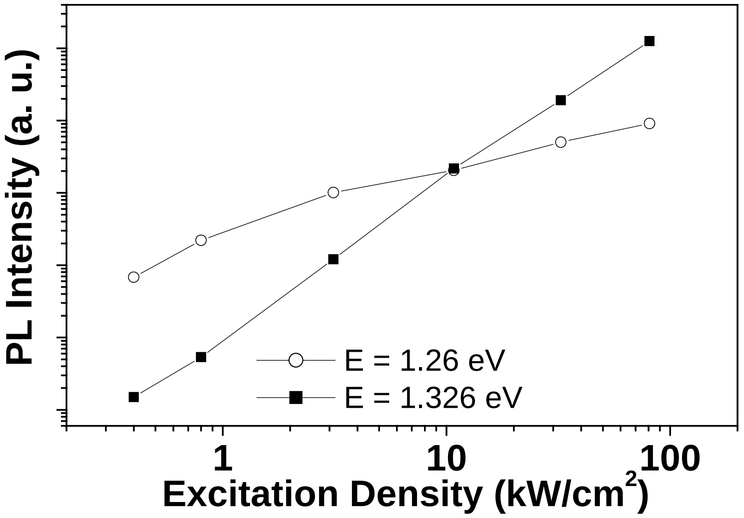

Fig. 4.3 Evolution of the PL intensities at 1.26 eV and 1.326 eV with respect to excitation density.

4.1.2.2 Excitation-Position Dependence

The size distribution of QD ensembles at different places of the wafer could be different. This effect is clearly shown in Fig. 4.4(a). It can be seen from Fig. 4.4(a) that at relatively low excitation density, the shape of the PL spectra at three different points about 1 mm apart from each other, are different. For Position A, two sub-peaks and one shoulder on the high energy side can be clearly seen, while for Point C and B, the whole spectrum is characterized only by one broad peak. In addition, the fine structures for the three spectra are different from each other. On the other hand, when the peak at 1.326 eV dominates the whole spectrum at high excitation power density, the peak energies for the three excitation-positions are consistent with each other, as shown in Fig. 4.4(b). This property implies that the peak at

1.326 eV originates from the delocalized states of the studied structure.

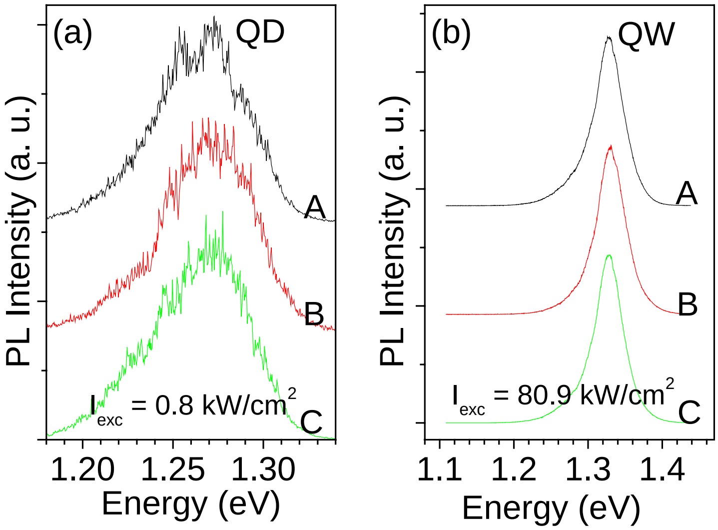

Fig. 4.4 Micro-Photoluminecence spectra at three different points at 10 K, at lower excitation power density (a), and at higher excitation power density (b).

4.1.3 Excitation-Energy Dependence of Photoluminescence

4.1.3.1 Presence of Continuous States Below the GaAs Band Gap

To confirm the presence of QW states in our sample, selective PL at different excitation energies is measured at 10 K. The wavelength-tuneable Ti-Sapphire laser is used as the excitation source and the excitation size is about 50 μm in diameter, so a large number of QDs are excited simultaneously.

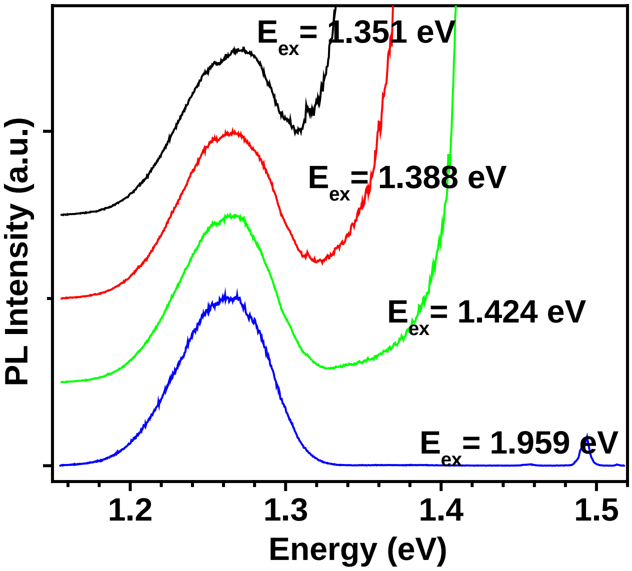

Fig. 4.5 Selective PL spectra of SML QD structure at 10 K at different excitation energies (a) 1.959 eV, (b)1.424 eV, (3)1.388 eV, (4)1.351 eV. The spectra are shifted for clarity.

As shown in Fig. 4.5, the PL band shape of the QD ensemble is not sensitive to the excitation energies even when the excitation energy is as low as 1.351 eV on the high-energy tail of curve *d* in Fig. 4.2. This property supports the existence of QW states, because if QW states had no role in the energy transfer to the QD states, then excitation with energy below the GaAs bandgap would not be able to excite the totality of QDs as if they were excited with radiation above the GaAs bandgap. The QW in the SML QD heterostructure is formed by In-Ga intermixing either during the alternating deposition of the InAs/GaAs superlattice, or during growth of the final layers at higher growth temperature. Full lateral intermixing would result in an extended quantum well of composition $In_{0.17}Ga_{0.83}As$. Assuming an 8.5 nm square-well QW potential, i.e., neglecting vertical intermixing, this QW would have a ground-state transition at 1.307 eV, marked by the arrow in Fig. 4.2. With the same assumption the observed QW transition at 1.326 eV corresponds to an alloy composition $In_xGa_{1-x}As$ with x = 0.15 < 0.17, indicating the formation of In-rich QDs.

4.1.3.2 Phonon–Assisted Transitions

When the excitation energy E_{ex} is tuned near to the edge of the density of states in the QW (E_{ex} = 1.336 eV), a few sharp resonant lines and a resonant PL band appear on the continuous broad PL band, near to the 1 longitudinal optical (LO, 31 ~ 36 meV) and 2LO (66 meV) phonon energies below the excitation energy, respectively, as shown in Fig. 4.6. To confirm that these sharp lines are not attributed to resonant Raman scattering, the polarization directions of the incident laser beam and the detected PL signal were set to be along the $[110]$ and the $[1,\bar{1},0]$ directions, respectively, in the back-scattering geometry, as in Ref. 49. Raman signal cannot be detected in such geometry, according to the selection rules of Raman scattering [50].

The phonon-enhanced bands were also reported for the SK QDs with excited states, and multi-phonon intra-dot energy relaxation was used to account for the observed PL enhancement [51-53]. When E_{ex} is much higher than the lowest transition energy E_{WL} of the 2D wetting layer, the multi-phonon processes in the photoluminescence spectra are generally masked by the inhomogeneous broadening due to dot size and shape fluctuations. Instead, for $E_{ex} \leq E_{WL}$, only the small subset of QDs whose excited states coincide with E_{ex} contribute to the emission, leading to multi-phonon resonance.

However, in the SML-grown QD structure, when the excitation energy is less than one GaAs LO-phonon energy above the lateral QW ground state, the probability for the photon-excited carriers (excitons) to relax within the QW states by emission of only longitudinal acoustic (LA) phonons is less than the carrier (exciton) capture probability from QW to QDs by emission of LO phonons. Dots which can be accessed by emission of LO phonons are populated more efficiently, since their delta-function-like DOS can be accessed directly from the excited energy level in the QW by LO phonon emission.

The complex structure in the 1LO resonant peaks consists of several optical phonon modes whose energies are 36.7 meV, 34.5 meV, 32.9meV and 31.3 meV, respectively, as shown in the inset of Fig. 4.6. We assign these lines to the LO phonon modes in the GaAs barrier, the GaAs/InAs interface, the InGaAs lateral QW, and the InGaAs QDs, respectively. The 2LO resonance occurs at the energy of 66 meV below the excitation energy, nearly two times the LO phonon energies of QW. The co-existence of several optical phonon modes indicates the complex structure of SML QDs.

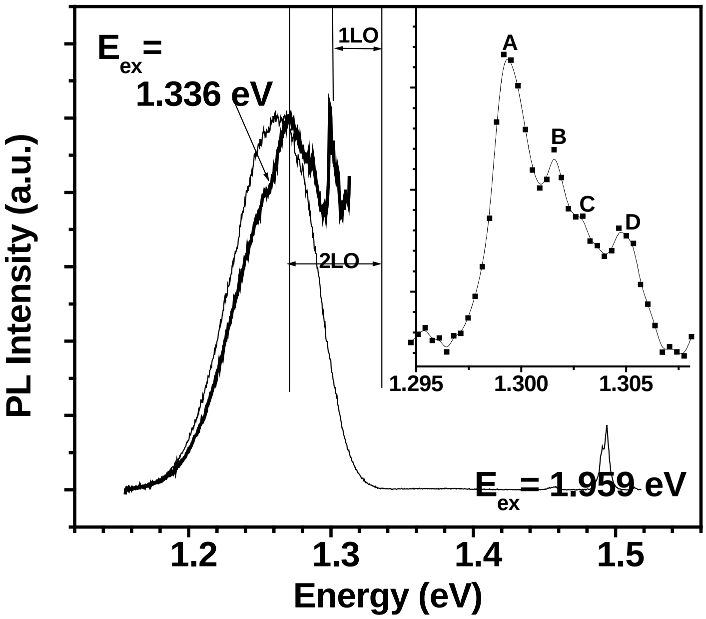

Fig. 4.6 The PL spectra of the SML QD structure at the excitation energies of 1.959 eV above the GaAs barrier band gap, and 1.336 eV just above the edge energy of the QW, at 10 K. The inset zooms in the 1LO parts, and the solid line is a guide for the eye.

4.1.3.3 Resonant Peaks of Defect States in GaAs Layers

When the excitation energy varies across the GaAs band gap, i.e. 1.515 eV, at 10K, a clear reduction of QD PL emission is observed. When $E_{ex} = 1.545$ eV, besides the broad PL band from QDs centered at 1.26 eV, three additional peaks appear at 1.458 eV (A), 1.494 eV (B) and 1.513 eV (C), as shown in Fig. 4.7(a). Peak B is attributed to a conduction band-to-acceptor recombination, and Peak A is the phonon replica of Peak B, as their energy difference is exactly the

GaAs-like LO energy of 36 meV. Peak C is due to the excitons bound to neutral point defects [54]. When $E_{ex} = 1.504$ eV, Peak A and B are enhanced, and the 2LO replica of Peak B appears at 1.42 eV (E). Peak F is due to the Raman scattering of the incident laser beam. Furthermore, a strong asymmetric PL band appears at 1.360 eV (D) with FWHM of 34 meV. Its phonon replica (1.325 eV, G) can also be identified.

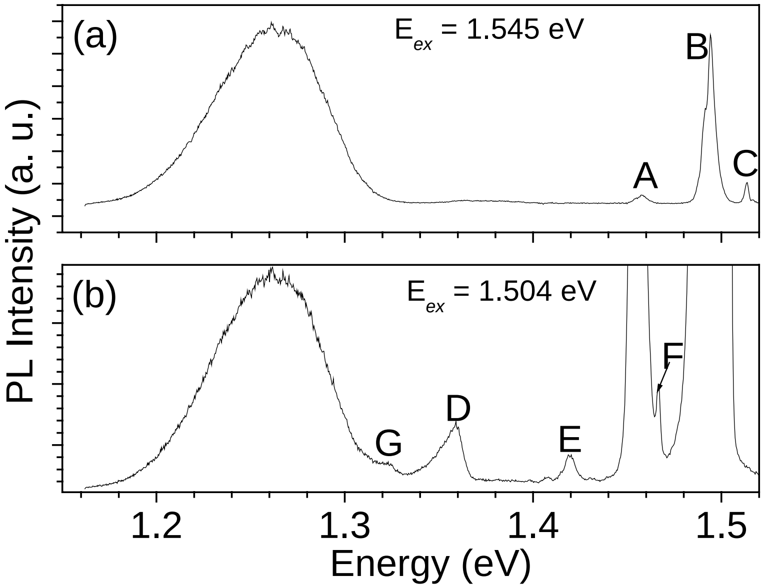

Fig. 4.7 PL spectra of SML InGaAs/GaAs QD structures at 10 K for two different excitation energies across the GaAs band gap, at 10 K.

The variation of the intensity ratio between Peak D and the QD PL peak, with respect to the excitation power density, is shown in Fig. 4.8. It can be seen that the ratio decreases with the increase of the excitation power density, indicating the low density of states (DOS) for Peak D. This property rules out of the possibility of Peak D being induced by the lateral QW states.

Fig. 4.9 shows the variation of the intensity ratio between Peak D and the QD PL peak, with respect to the excitation energy. The excitation density was set to be as low as $0.14W/cm^2$, in order not to saturate the signal of Peak D. From Fig. 4.9, an asymmetric resonance peak can be clearly seen at $E_{ex} = 1.508$ eV. This energy is likely to correspond to the excited states related to Peak D. In addition, the ratio at the exaction energy above 1.515 eV is much smaller than that below 1.515 eV, indicating the competition in the carrier capture between QD states and the states corresponding to Peak D.

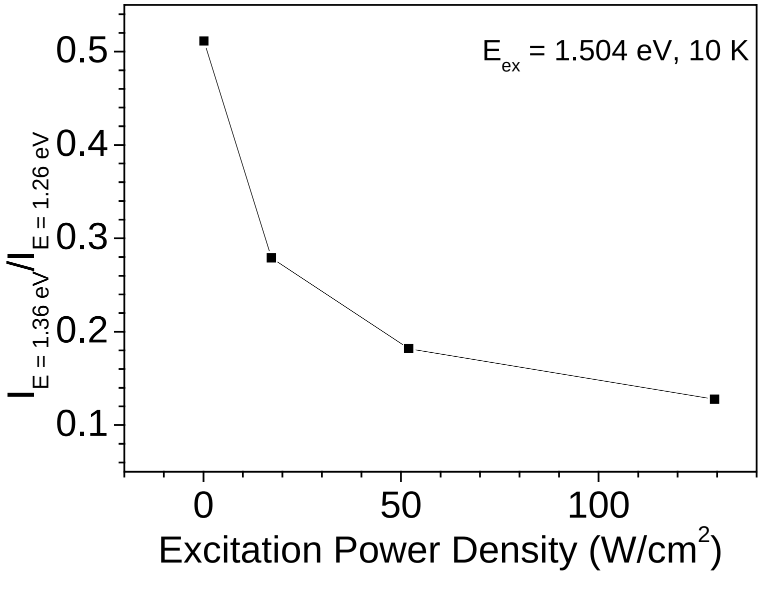

Fig. 4.8 The intensity ratio between the peak at 1.360 eV and the peak of QD PL band versus the excitation power density.

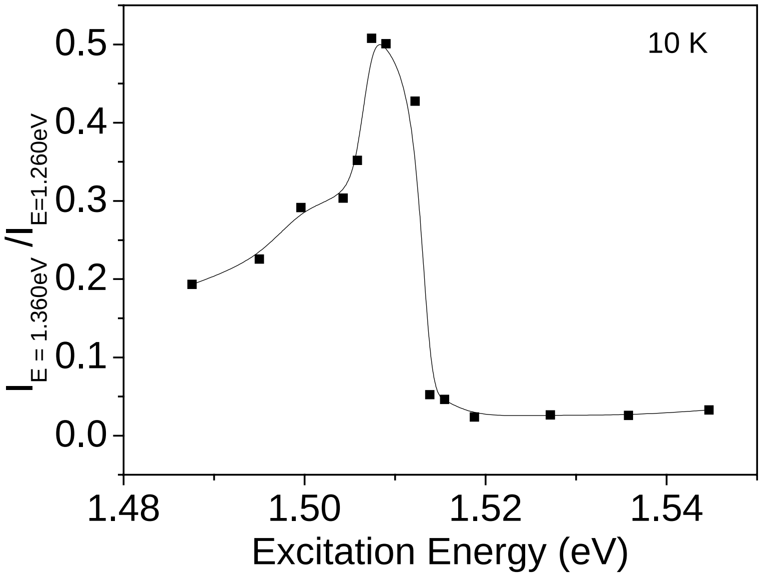

Fig. 4.9 The intensity ratio between the peak at 1.360 eV and the peak of QD PL band versus the excitation energy.

The same phenomenon was also observed in our SK-grown InGaAs/GaAs QD samples and a sample with MBE-grown GaAs on GaAs substrates. Therefore, the peak at 1.36 eV is likely to be directly related to the deep defects in GaAs layers produced by our MBE system. It probably results from the radiation transition between the conduction band or shallow donors and the 0.156-eV Cu_{Ga} acceptors in the GaAs layers [55-57]. The photon-generated carriers in the QW can either relax into to the excited state of the substitutional Cu_{Ga} defects or be captured by the QDs. The fact that Peak D cannot be detected in the spectra excited above the GaAs band gap, implies that the density of Cu_{Ga} defects is very low in our samples and Cu could be unintentionally contaminated during the epitaxial growth.

4.1.4 Temperature Dependence of Photoluminescence

A crucial issue for the realization of room temperature efficient photonic devices is the understanding of the temperature dependence of PL. The temperature dependence of PL for SK InAs/GaAs QDs has been reported by several groups [58-60], but not for SML InGaAs/GaAs QDs, which will be studied in this section. Here, a He-Ne laser at the wavelength of 632.8 nm is used as the excitation source. The excitation power density is 129 W/cm^2 , and the excitation size is about 50 μm in diameter.

4.1.4.1 Narrowing of FWHM at Intermediate Temperatures

The PL spectra of the SML-grown QD ensemble in the temprature range of 10 – 300 K are plotted in Fig. 4.10. The spectrum at 10K is asymmetric, and centered at 1.260 eV with a full width at half maximum (FWHM) of 78 meV. As the temperature increases, it can be seen from Fig. 4.10, that the high energy side of the PL spectrum of the QD ensemble red-shifts at a higher rate than the low energy side, because the photo-carriers escape more easily from smaller dots with shallower confinement potential and higher energy emissions than from larger dots with deeper confinement potential and lower energy emissions. This effect results in the reduction of the FWHM as the temperature increases. After having reached a minimum value at T = 80 K, the FWHM slowly recovers to the low-T value, as shown in Fig. 4.11. At temperatures higher than 170 K, the

PL intensity from the QW is stronger than that from the QD ensemble, due to the increased probability of thermal escape of carriers from QD states to QW states and the higher density of states in the QW.

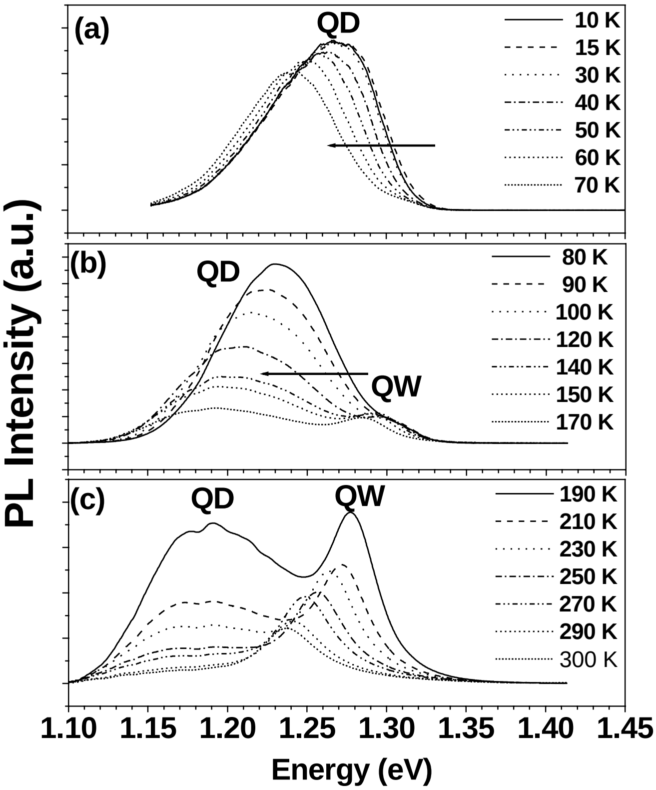

Fig. 4.10 PL spectra of the SML InGaAs/Ga QD ensemble measured at different temperatures.

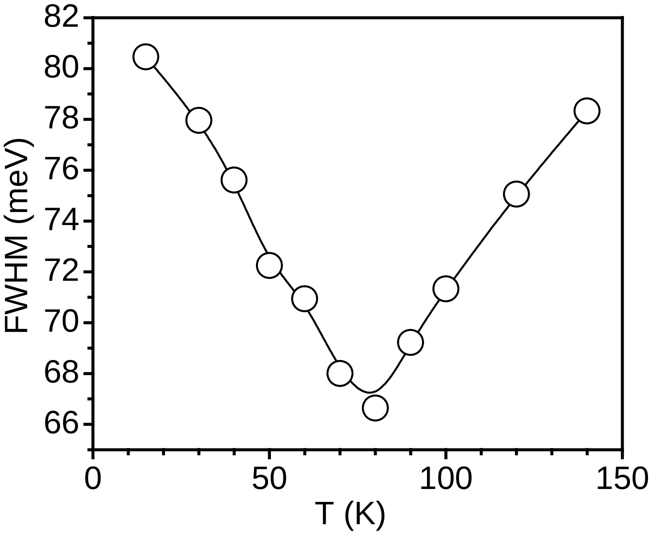

Fig. 4.11 FWHM of PL spectra versus temperature, the solid line is a guide for the eye.

4.1.4.2 Sigmoidal Behaviour of Peak Energy

Here, we present the temperature dependence of the peak position of the PL band. As shown in Fig. 4.12, the peak energy of the QD emission band follows the Varshni law [61], in the ranges of 10 K to 40 K, and 150 K to 300K, but in the range of 50 K to 150 K, the peak energy red-shifts faster than given by the Varshni law. In contrast, the variation of the peak energy of the QW states with temperature obeys the Varshni law. This property confirms that the peak at 1.326 eV in Fig. 4.1 is from QW states rather than the excited states of the QD ensemble. The sigmoidal change of the peak energy of the QD PL band can be attributed to the carrier transfer from smaller QDs to the lager QDs via the QW states. For SK InAs/GaAs QDs, the sigmoidal dependence of the peak energy of PL band on temperature was reported by L. Brusaferri et al. [58]. In the SK QD ensemble, the carriers transfer between QDs via the wetting layer states.

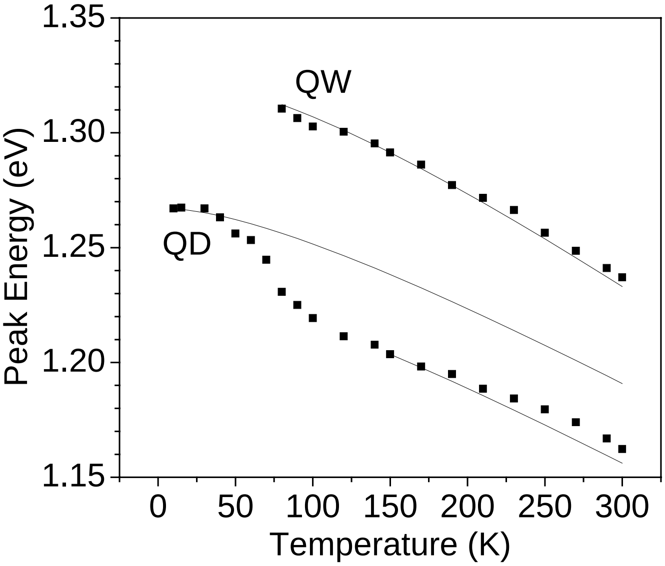

Fig. 4.12 Temperature dependence of the peak energies of the QD (square) and QW (triangle) spectra of the SML InGaAs/GaAs QDs sample. The continuous lines are calculated according to the Varshni law using parameters of InAs, i.e., $E_g(T) = E_g(0) - 2.5\times10^{-4}T^2/(T+75)$ [62,63] and are shifted along the energy axis.

4.1.4.3 Carrier Transfer Between Different Quantum Dots

In order to illustrate the carrier transfer between different quantum dots at intermediate temperatures, we chose a certain energy position on the spectrum at 10 K and then investigated the intensity variation at a photon energy that follows the movement of the band gap of bulk InAs when temperature changes, assuming the PL line of a single QD shifts with temperature as the bandgap does [64]. Three curves are plotted for three energies at 1.20eV(A), 1.26 eV (B) and 1.30 eV (C) on the PL spectrum at 10 K, respectively, as shown in Fig. 4.13. It can be seen from Fig. 4.13 that, the PL intensity decreases monotonically with increasing temperature, for the QDs corresponding to energy point C. For the QDs corresponding to energy point B, the PL intensity is almost constant from 10 K to 60 K and then decreases with increasing temperature. Most interestingly, the PL intensity for the QDs corresponding to energy point A is almost constant from10 K to 60 K and then increases until a maximum is reached at around 100 K, and finally decreases with increasing temperature. Because the larger emission energy corresponds to the smaller QD size, the enhancement of PL intensity for the QDs corresponding to energy point A at intermediate temperatures is a sign of the transfer of carriers from smaller QDs to larger ones.

When temperature increases, electron-hole pairs in smaller QDs can thermally escape into the QW states more easily because of their shallower potential confinement. The thermally escaped carriers will preferentially populate the larger QDs with lower energy states, resulting in an enhancement of the PL intensity for larger QDs at the intermediate temperatures.

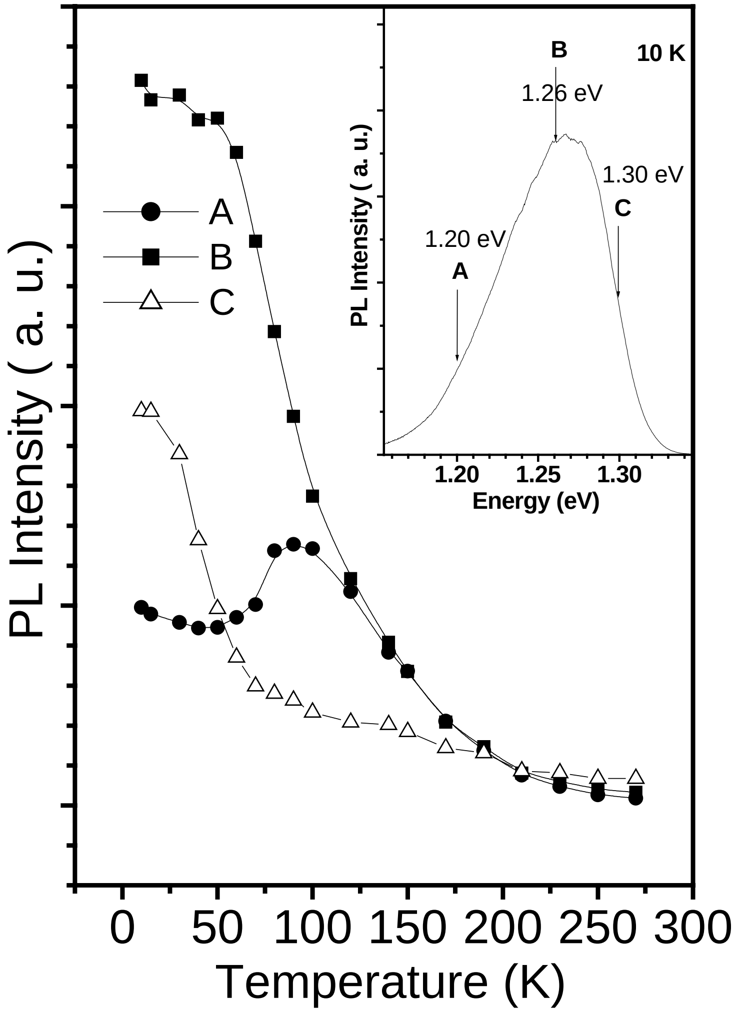

Fig. 4.13 PL intensity at different energy positions versus temperature. The arrows in the inset give the energy positions at 10 K and the temperature-induced energy variation to follow the band of InAs.

4.1.5 Polarization of Photoluminescence

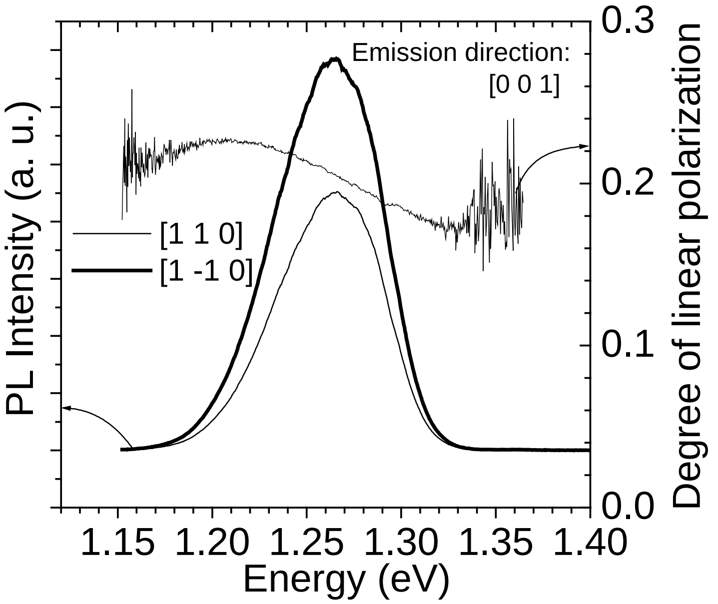

Fig. 4.14 Photoluminescence spectra and degree of linear polarization measured in the backscattering geometry at 10K, collecting light polarized along the $[110]$ (thin line) and $[1\bar{1}0]$ (thick line) lattice directions.

Shape anisotropy effects on the electronic properties of SML InGaAs/GaAs QDs are investigated here by measuring the polarization dependence of the optical transitions. The PL was excited at 10K by a He-Ne laser at 632.8 nm with excitation density ~ 10 W/cm^2. The polarization of PL was analyzed using a fixed polarizer and a broadband $\lambda/2$ plate. The polarization of PL is not influenced by the polarization of the excitation laser, since the excitation photon energy is above the band gap of GaAs, and the initial polarization is lost during the carrier relaxation into the QD's. The PL polarization anisotropy is defined as $P = (I_{\perp} - I_{//})/(I_{\perp} + I_{//})$, where $I_{\perp}$ is the vertically polarized intensity and $I_{//}$ is the horizontally polarized intensity in the laboratory coordinate system.

4.1.5.1 In the Backscattering Geometry

Fig. 4.14 shows the PL spectra and the degree of linear polarization of PL measured in the backscattering geometry. The light propagates in the $[001]$ direction (surface emission), $I_{\perp}$ and $I_{//}$ are polarized along the $[1\bar{1}0]$ and $[110]$ directions, respectively. The broad peak centered at 1.26 eV with a line width of 55 meV is assigned to the ground state transitions of the SML InGaAs/GaAs QDs. PL emission from the QDs is predominantly polarized along the $[1\bar{1}0]$ direction in the whole energy range, $P \approx 0.2 \pm 0.02$ due to the elongation of the QDs along the $[1\bar{1}0]$ direction, as shown in the plan-view TEM image of SML InGaAs/GaAs QDs in Chapter 3.

4.1.5.2 In the Edge Geometry

In the edge geometry, the spectra are obtained exciting and detecting at the sample edges, the light propagates in $[110]$ or $[1\bar{1}0]$ direction, $I_{\perp}$ and $I_{//}$ are polarized along the $[1\bar{1}0]$ or $[110]$ and the $[001]$ directions, respectively. These polarizations are, respectively, referred to as transverse electric (TE) and transverse magnetic (TM) modes. To suppress the PL emission from the $[001]$ sample surface, the edge emission was spatially selected in near and far fields. The experimental setup and a near-field image for the PL excited and collected from the edge of an SML QD sample in the edge geometry are shown in Fig. 4.15 and Fig. 4.16, respectively.

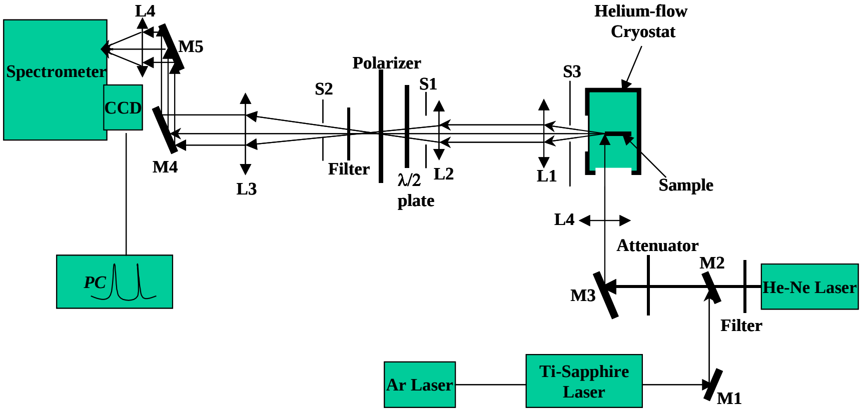

Fig. 4.15 The experimental set-up for CW PL experiments in edge geometry, M1 ~ M5 are mirrors, L1 ~ L4 are lenses, S1,S2 and S3 are small holes used to limit the collection angle of PL.

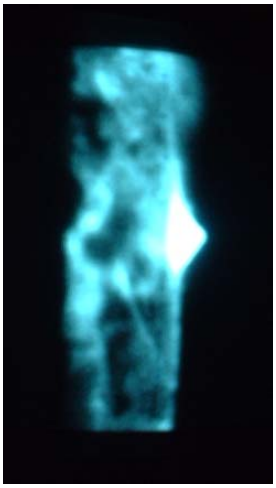

Fig. 4.16 A near-field image for the PL excited and collected from the edge of an SML QD sample in the edge geometry. The bright triangle-shaped spot shows the excitation point.

It is well known that, in a lattice-matched quantum well, the ground state has the heavy hole character and the first excited state has the light hole character. When the quantum well is compressively strained the energy splitting between the heavy and light hole is enlarged [65] and the ground state is more purely a heavy-hole state. According to Kane's selection rule, the heavy-hole exciton luminescence in zinc-blend QWs grown on a high-symmetry (100) surface must be *completely TE-polarized*, i.e. the ground state luminescence observed in the edge geometry is only polarized in the plane of quantization. This was confirmed experimentally in numerous studies, for example in Ref. [66]. However, contrary to the QW case, a significant contribution of the TM-polarized emission has been observed, as shown in Fig. 4.17, pointing to a significant role of the lateral exciton confinement. A slightly higher anisotropy of $P \approx 0.17 \pm 0.02$ for emission along the $[1\bar{1}0]$ direction (Fig. 4. 17(b)) than that of $P \approx 0.09$ along the $[110]$ direction (Fig. 4.17(a)) is due to the fact that the lateral dimensions of SML QDs along the $[1\bar{1}0]$ direction are nearer to the QD heights. A similar result has been observed in the case of SML CdSe/ZnSSe QDs [13]. This feature is not only of the fundamental interest for electronic structure and optical properties, but also important in its applications in polarization-independent devices.

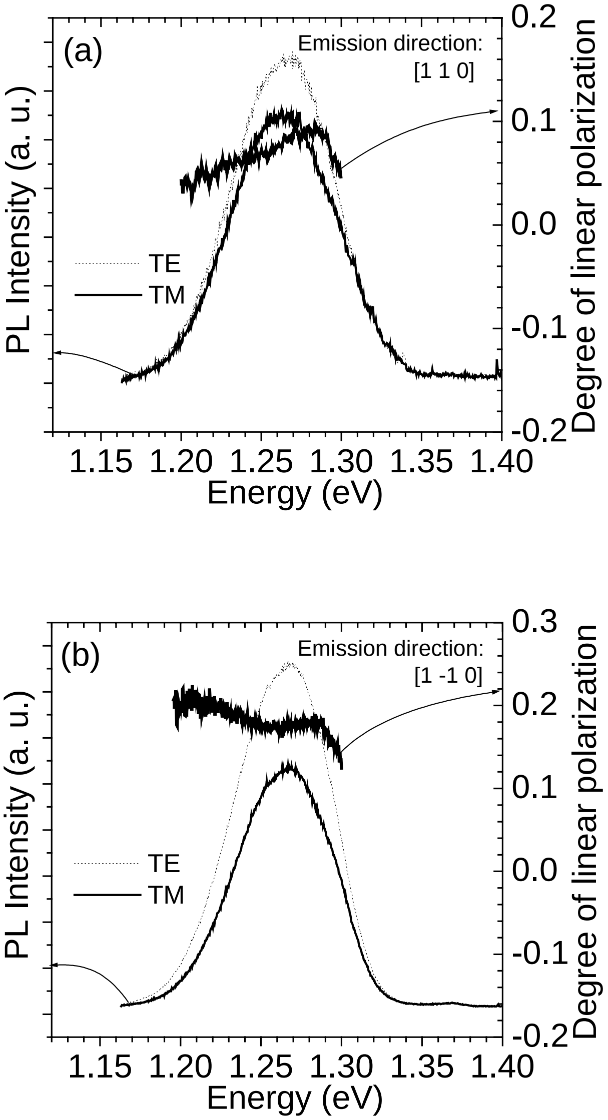

Fig. 4.17 Photoluminescence spectra and degree of linear polarization measured in the edge geometry at 10K, (a) collecting light polarized along the $[1\bar{1}0]$ (dotted line) and $[001]$ (continuous) lattice directions; (b) collecting light polarized along the $[110]$ (dotted line) and $[001]$ (continuous) lattice directions.

4.2 Time-resolved Photoluminescence

To evaluate the carrier capture, relaxation and recombination dynamics of SML InGaAs/GaAs QD structures, TRPL experiments were performed at 5 K. In the TRPL setup, the sample was cooled in a liquid helium cryostat and excited in the GaAs barriers with 120 fs pulses from a Ti:sapphire laser and the PL signal was collected, dispersed, and synchronously detected using a streak camera with 2.5 ps time resolution. The excitation size is about 50 μm in diameter.

4.2.1 Spectrum Evolution

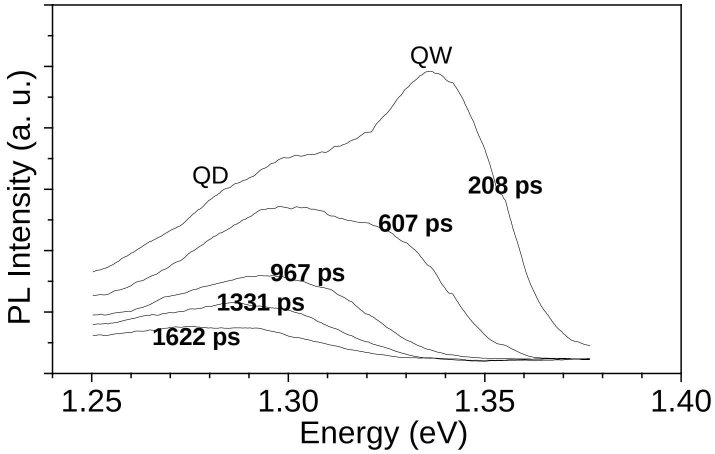

Fig. 4.18 Time-resolved PL spectra from SML InGaAs/GaAs QD structures, at different delay times after the laser pulse. The excitation power density is $224 W / cm^2$.

The spectrally resolved signal provides a good illustration of the temporal evolution of the carrier distribution among the energy levels.

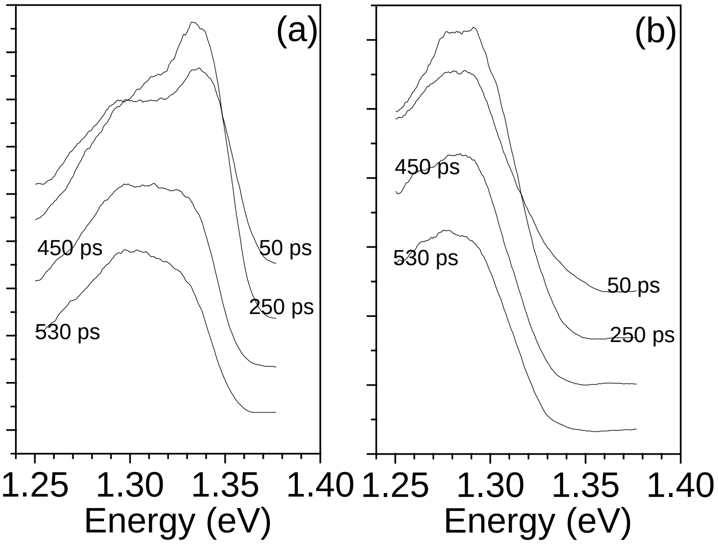

Fig. 4.19 Time-resolved PL spectra from SML InGaAs/GaAs QD structures at different delay times after the laser pulse. The excitation power density is $224W/cm^2$ (b) and $45W/cm^2$, respectively.

Fig. 4.18 shows the PL spectra at different delays after the laser pulse, at the excitation power density of $224W/cm^2$. It can be seen that the QW peak dominates the whole PL spectrum at 208 ps and then decay rapidly, while the QD peak lasts even at 1622 ps. When the excitation power density is as low as 45 W/cm^2, the QW can not be observed and only the QD peak dominates the whole PL spectrum, even at 50 ps delay after the laser pulse, as shown in Fig. 4.19. The electron-hole (e-h) pairs (or excitons) generated in the GaAs barrier are captured directly into the QW and then relax in the QW and finally captured by the QDs. It is also possible that the e-h pairs (or excitons) are directly captured by the QDs. If the carrier density is much higher than the QD density, the excess e-h pairs (or excitons) will recombine in the QW, leading to the appearance of the QW peak.

4.2.2 Radiative Lifetime

A quantity closely related to the dimensionality of semiconductors is the intrinsic radiative lifetime τ_0 of excitions (i.e., the transformation time of an exciton into a photon at low temperature). In bulk materials, the mixed state of exctions and photons, the exciton-polariton, is a stationary state and has therefore an infinite τ_0 [67]. A photon will leave the crystal only in the presence of imperfections, such as surfaces, phonons, or impurities which relax energy and momentum conservation [68]. In contrast, τ_0 in a 2D structure, i.e., a quantum well, is only several tens of picoseconds due to the reduction of the translational invariance down to two directions [69-71]. In 1D structures or quantumn wires, τ_0 increases again. A reduction of coherence length of the excitons due to lower dimensionality is responsible for this effect [72]. A further reduction of dimensionality to 0D once more causes an increase in τ_0 [73,74].

The QD exciton lifetime can be estimated from the PL transients at long times, where feeding from highly-lying states is negligible. Fig. 4.20 shows the PL transient of QD states in SML InGaAs/GaAs QD structures, at excitation density of 45 W/cm^2. The detection energy is set to be 1.250 eV. The PL decay can be well fitted by a mono-exponential function. The decay time τ_d is found to be as long as 768 ps, which depends only slightly on the excitation density. The long decay time is a characteristic of a high-quality semiconductor material. The measured decay time for the QW states in SML InGaAs/GaAs QD structure is about 309 ns, as shown in Fig. 4.21, in good agreement with values measured for InGaAs/GaAs QWs [75,76].

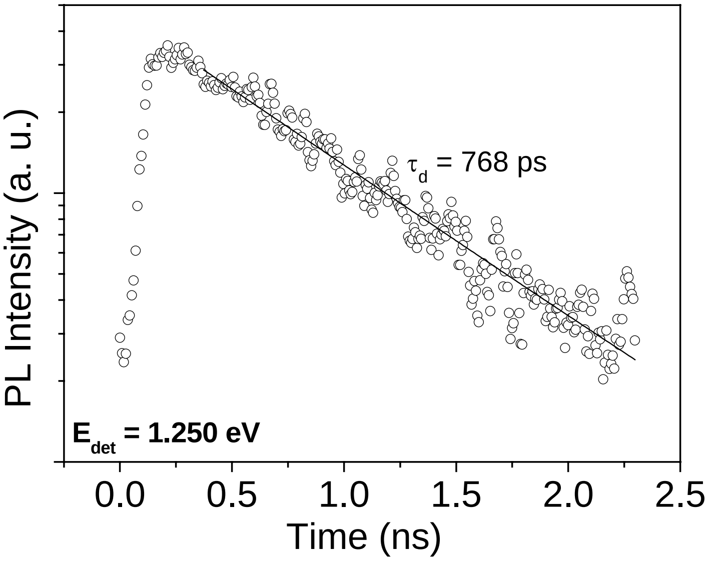

Fig. 4.20 PL decay transient for the QD states in SML InGaAs/GaAs QD structures at excitation density of $45 W/cm^2$. The dots show the experimental data, and the solid line shows the fitting data.

Fig. 4.22 shows the values of τ_d plotted against the QD emission energy. With increasing QD transition energy and therefore decreasing QD size, the decay time decreases. This can be due to nonradiative contributions or can have an intrinsic reason [1]. Recently it has been pointed out that the differences in QD-PL lifetimes have to be assigned to variation of the electron-hole overlap induced by different QD morphology [77]. The smaller lifetime for smaller QDs can be attributed to a larger e-h overlap in QDs. The increase of oscillator strength (decrease of lifetime) is connected with a reduction of confinement effect [78]. In the model of Sugawara et al., the lifetime converges against the limit for small-sized quantum dots when infinite barriers are used. In actual quantum dots with finite confinement potential, the lifetime will decrease again for smaller quantum dots because the wavefunction penetrates into the barrier and strong confinement is lost. On the other hand, lateral phonon-asisted tunnelling from smaller to larger QDs has been proposed to explain the shorter lifetime of the smaller QDs [79,80]. This is possible for SML QD samples, as the density of QDs in our samples is very high.

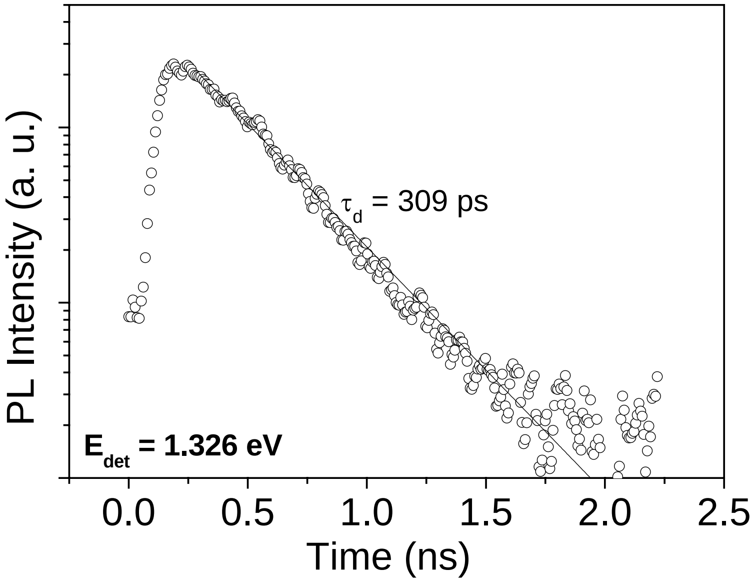

Fig. 4.21 PL decay transient for the QW states in SML InGaAs/GaAs QD structures at excitation density of $224 W / cm^2$. The dots show the experimental data, and the solid line shows the fitting data.

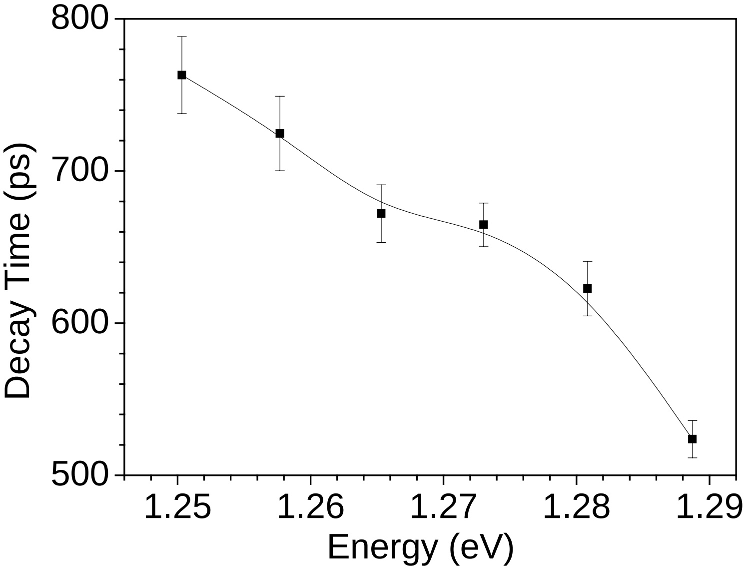

Fig. 4.22 Low temperature (5K) radiative lifetimes for the QD states in SML InGaAs/GaAs QD structures, plotted against the QD emission energy. The excitation intensity is 45 W/cm^2.

4.2.3 Carrier Capture and relaxation

The rise time τ_r of PL transients can provide information on carrier capture to and relaxation in the QDs. Since thermalization and relaxation processes with the three dimensional GaAs and the two dimensional QW occur on a much faster time scale [81], the rise time mainly reflects the capture process into the QD.

Carrier capture into the QDs has been examined by measuring PL rise times at the energies of QD transitions. As shown in Fig. 4.2.6, the PL transients were fit by the expression [82]

$$I(t) \propto \left[\exp(-t/\tau_r) - \exp(-t/\tau_d)\right]/(\tau_r - \tau_d), \tag{4.1}$$

where the decay time τ_d was taken from Fig. 4.22. The rise time at 1.25 eV is found to be 35 ps when the excitation density is 45 W/cm^2. The capture is mediated by Coulomb scattering (Auger process) and LO-phonon emission [82,83]. The rate of both of the processes depends on the carrier density in the QW, and the capture process becomes inefficient at low carrier densities in the QW.

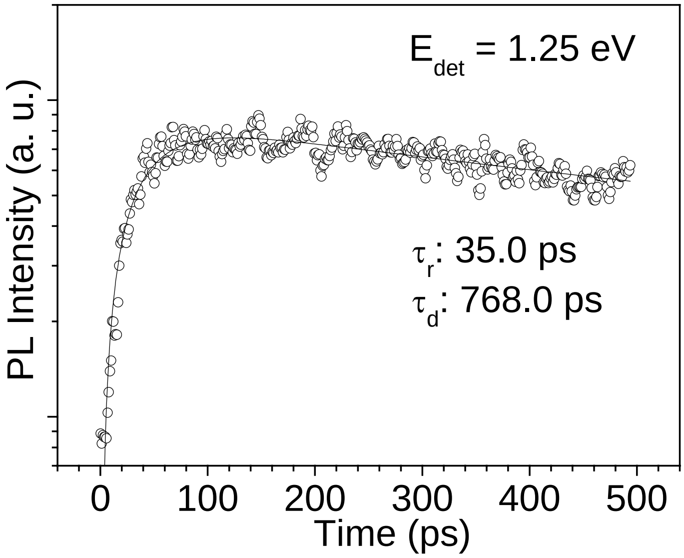

Fig. 4.23 The PL transient measured in short time-scale for the determination of rise time. The excitation intensity is 45 W/cm^2. The solid line shows the fitting data.

In order to separate the effects of carrier-phonon and carrier-carrier scattering in the capture dynamics, a detailed analysis of the PL rise time is performed as a function of excitation power. As shown in Fig. 4.24, we observe two different density regimes at low temperature (5K): 1) for excitation densities below 110 W/cm^2 (corresponding to $\approx 10^{17}$ electron-hole pairs per cm^3 per pulse), the PL rise time does not depend on the excitation power and 2) for excitation densities above 110 W/cm^2, the rise time decreases from 35 ps to 17 ps. This shows that at high excitation power carrier-carrier scattering leads to an acceleration of the low-temperature carrier capture into the QD states [84]. In case of Auger processes, the electron (hole) is assumed to be immediately captured into the QD state by transferring its energy to a second barrier electron (hole).

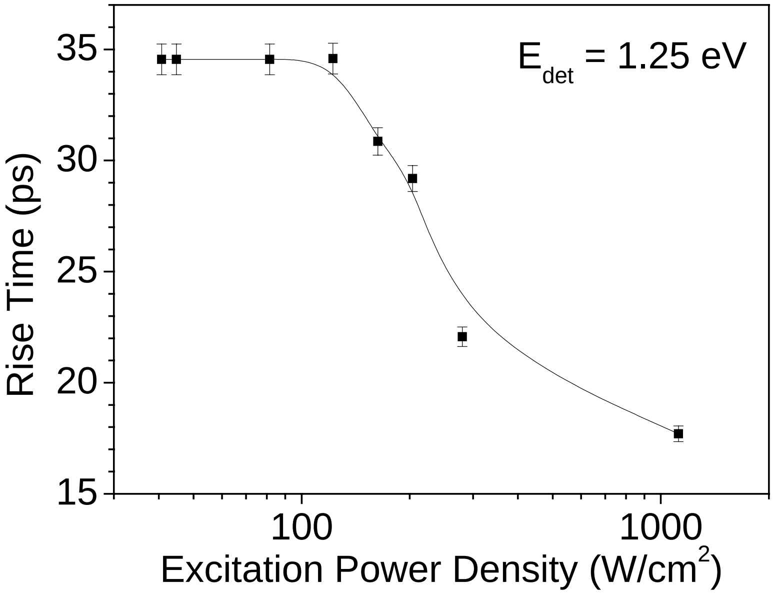

Fig. 4.24 Excitation power dependence of the rise time for SML InGaAs/GaAs QDs at 5 K. The solid line is a guide for the eye.

4.3 Conclusions

SML InGaAs/GaAs QD heterostructures grown at low temperatures were characterized by using low-temperature micro-PL, selective PL and temperature dependent PL techniques. ***The SML-grown QD heterostructure is verified to be a quantum-dot-quantum-well structure.*** Discrete emission lines from QDs have been observed in micro-PL spectra at 10 K. As the temperature increases, a sigmoidal behavior of the PL peak energy and a narrowing of the PL linewidth of the SML-grown QD ensemble are observed, and explained by carrier transfer from smaller dots to larger dots via QW states. Phonon-resonant PL bands and different local phonon modes, from the lateral QW, the QDs, the interfaces and the GaAs barrier are observed in the resonantly excited PL peaks. In the edge geometry, strong contribution of the TM mode to PL signal was observed, indicating the vertical coupling of the SML InAs islands in SML QD structures. The PL rise time (~ 35 ps) and the PL lifetime(~ 700 ps) of the QD state in the low excitation regime are comparable with those of typical SK QDs. As the excitation power increases, the Auger effect will be the dominant mechanism for the carrier capture to the QDs, resulting a decrease of the PL rise time.

Chapter 5 Optical Characterization of Sub-monolayer InGaAs/GaAs Quantum Dots Grown at High Temperature

In Chapter 4, the optical properties of SML InGaAs/GaAs quantum dots (QDs) grown at low temperature (480 ^{o}C) were investigated. At room temperature, the PL signal of QDs quenches and the QW peak dominates the whole spectrum, due to the thermal escape of carriers from QD to quantum well (QW) states Therefore, it is not suitable to use this kind of QDs for QD lasers working at room temperature. In this chapter, the optical properties of SML InGaAs/GaAs QDs (Sample HCØ809) grown at different conditions from those in Chapter 4, especially at higher growth temperature (500 ^{o}C), will be presented. The PL signal of QDs can be observed even at room temperature for HCØ809. A He-Ne laser at the wavelength of 632.8 nm is used for excitation. For the details of PL measurements, refer to Chapter 4.

5.1 Layer Structure of the Sample

The layer structure for HCØ809 is depicted in Fig. 5.1. The SML QD layer was formed with 10 cycles of alternate deposition of 0.5 ML InAs and 2.5 ML GaAs, at 500 ^{o}C**.**

GaAs 20 nm, 600 ^{o}C
AlAs 8nm, 600 ^{o}C
GaAs 15 nm, 600 ^{o}C
GaAs 5 nm, 500 ^{o}C
10 times (0.5 ML InAs – 2.5 ML GaAs), 500 ^{o}C,**QDs**
GaAs 100 nm, 600 ^{o}C
AlAs 8 nm, 600 ^{o}C
GaAs 140 nm, 600 ^{o}C
5 times (AlAs 2nm – GaAs 10 nm), 600 ^{o}C
GaAs Substrate

Fig. 5.1 The layer structures of Sample HCØ809.

5.2 Low Temperature Photoluminescence

The low-temperature PL spectra and the degree of the in-plane polarization of PL of SML InGaAs/GaAs QDs grown at high temperature are shown in Fig. 5.2. A strong sharp peak at 1.366 eV (7 meV in FWHM) and a weak broad peak at 1.347 (18 meV in FWHM) can be clearly seen in Fig. 5.2. The relative intensity between the two peaks does not depend on the excitation power density, indicating the bimodal distribution of QDs. Increase in substrate temperature causes shrinkage of the size of the islands due to the higher equilibrium concentration of atoms [85]. Therefore, the lateral size of QDs in HCØ809 could be smaller than that in HCØ737, leading to higher emission energy for HCØ809.

The intensity polarized along the [1 –1 0] direction is higher than that along the [1 1 0] direction, showing the in-plane optical anisotropy. The degree of linear polarization is 0.12, indicating the QDs in HC0809 are also slightly elongated along the [1 –1 0] direction.

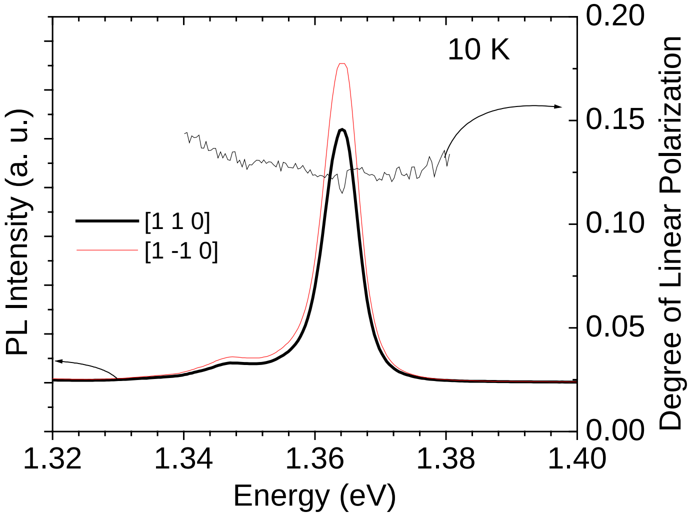

Fig. 5.2 PL spectra and the degree of the in-plane polarization of PL of SML InGaAs/GaAs QDs grown at high temperature. The measurement was carried out in the back-scattering geometry, at 10 K.

5.3 Temperature-Dependent Photoluminescence

As the temperature increases, the two peaks in Fig. 5.2 redshift. But at room temperature, the weak broad peak at the lower energy side disappears, only the strong sharp peak at the higher energy side remains to be observable, as shown in Fig. 5.3. The temperature dependence of the peak energy follows the Varshni law, as shown in Fig. 5.4. The sigmoidal behaviour of the peak energy has not been observed in this sample, due to the narrow FWHM of PL band.

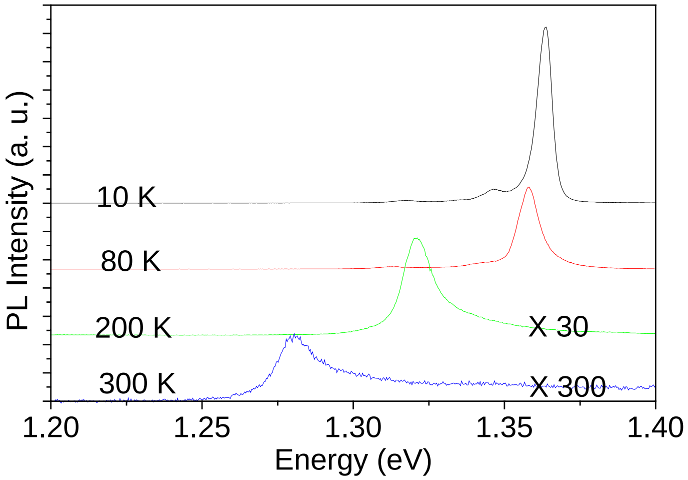

Fig. 5.3 Temperature-dependent PL spectra of SML InGaAs/GaAs QDs grown at high temperature.

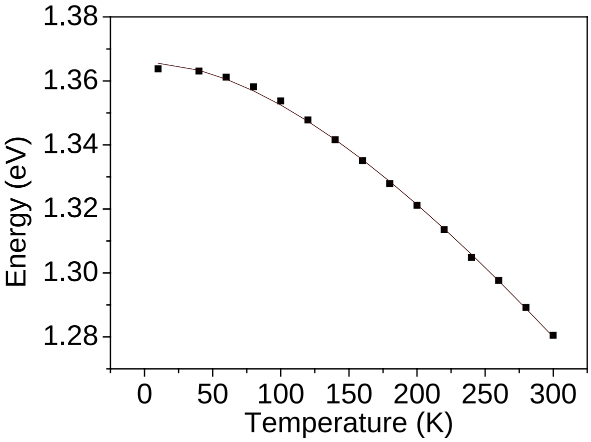

Fig. 5.4 Temperature dependence of the PL peak energy. The continuous line is calculated according to the Varshni law.

Compared with the QDs (HCØ737) grown at lower temperature, the lateral confinement for the QDs grown at higher temperature (HCØ810) could be stronger and the probability of the thermal escape of carriers from QD states to higher states is smaller. Therefore, the PL signal can be still observable at elevated temperatures.

5.4 Photoluminescence in the Edge Geometry

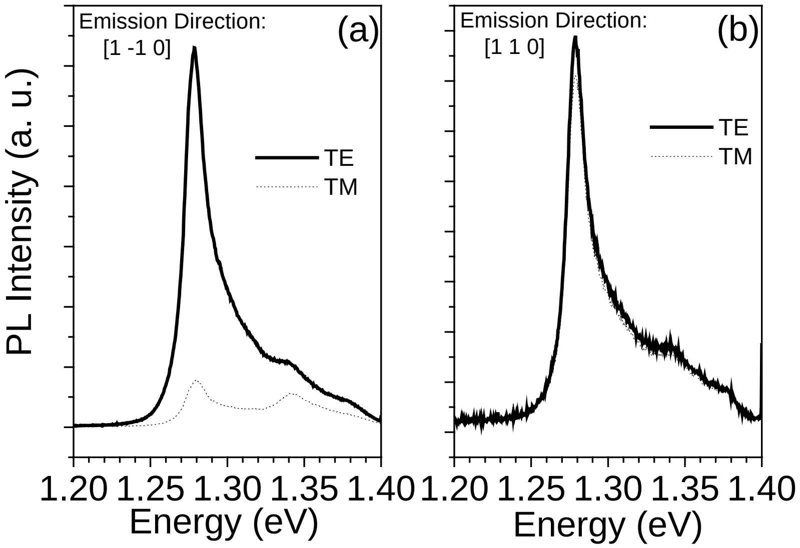

Fig. 5.5 Polarized PL spectra in the edge geometry at room temperature. The emission directions are along the [1 –1 0] (a) and [1 1 0] (b) directions, respectively.

The polarization of PL in the edge geometry was investigated at room temperature. As shown in Fig. 5.5, when the emission direction is along the $[1\,\bar{1}\,0]$ direction, the intensity in the TE mode is about 8 times the intensity in the TM mode. However, when the emission direction is along the $[1\,1\,0]$ direction, the intensity in the TE mode is nearly the same as the intensity in the TM mode. This property clearly proves that SML InGaAs/GaAs QD heterostructure grown at high temperature is quite different from an InGaAs/GaAs quantum well structure, in which only the TE mode can be observed for the ground state transitions, in the edge geometry [66]. In addition, the peaks corresponding to the first (1.34 eV) and second (1.38 eV) excited states can be seen in the PL spectra.

5.5 Conclusions

In summary, the temperature-dependent PL and optical anisotropy of SML InGaAs/GaAs QDs grown at high temperature (500 ^{o}C) show that the PL signal of QD ground states remains to be observable even at room temperature. Strong contribution of the TM mode to PL signal is also observed in the edge geometry. A laser diode whose active region consists of such a QD heterostructure would be a real QD laser lasing from the QD ground states at room temperature, which will be investigated in Chapter 6.

Chapter 6 Sub-monolayer InGaAs/GaAs Quantum-dot Lasers with High Modal Gain and Zero Linewidth Enhancement Factor

In this chapter, sub-nomolayer (SML) InGaAs/GaAs quantum-dot (QD) lasers are introduced and characterized. The growth of the epitaxial structures, room temperature photoluminescence (PL) from the SML QDs inside the eptaxial structures for lasers, and device fabrication are presented in Section 6.1 to 6.3. Section 6.4 gives the basic characterization of an SML InGaAs/GaAs QD laser device. In Section 6.5, the gain spectra and the linewidth enhancement factor of SML InGaAs/GaAs QD lasers will be measured. Fourier analysis of the amplified spontaneous emission spectra for different SML InGaAs/GaAs QD lasers fabricated from the same wafer is demonstrated in Section 6.6. Section 6.7 summarizes the main results of this chapter.

6.1 Device Growth

The expitaxial structure (Sample HC0819) was grown by solid-source molecular beam epitaxy (MBE) on an n^+-doped GaAs (100) substrate. It consists of an n-type ($10^{18}cm^{-3}$) 0.5 μm thick GaAs buffer, a 1.5μm thick n-type ($10^{18}cm^{-3}$) $Al_{0.2}Ga_{0.8}As$ lower cladding layer, a 200 nm thick GaAs confining layers ($n = 10^{17}cm^{-3}$ and $p = 10^{17}cm^{-3}$) surrounding the laser active region, a 1.5 μm p-type ($10^{18}cm^{-3}$) upper

GaAs cap, 0.2 μm, $p = 10^{19} cm^{-3}$
$Al_{0.2}Ga_{0.8}As$ cladding , 1.5 μm, $p = 10^{18} cm^{-3}$
GaAs, 0.1 μm, $p = 10^{17} cm^{-3}$
SML InGaAs QD active region
GaAs, 0.1 μm, $p = 10^{17} cm^{-3}$
$Al_{0.2}Ga_{0.8}As$ cladding, 1.5 μm, $n = 10^{18} cm^{-3}$
GaAs buffer 0.5 μm, $n = 10^{18} cm^{-3}$
GaAs substrate, $n = 10^{18} cm^{-3}$

(a)

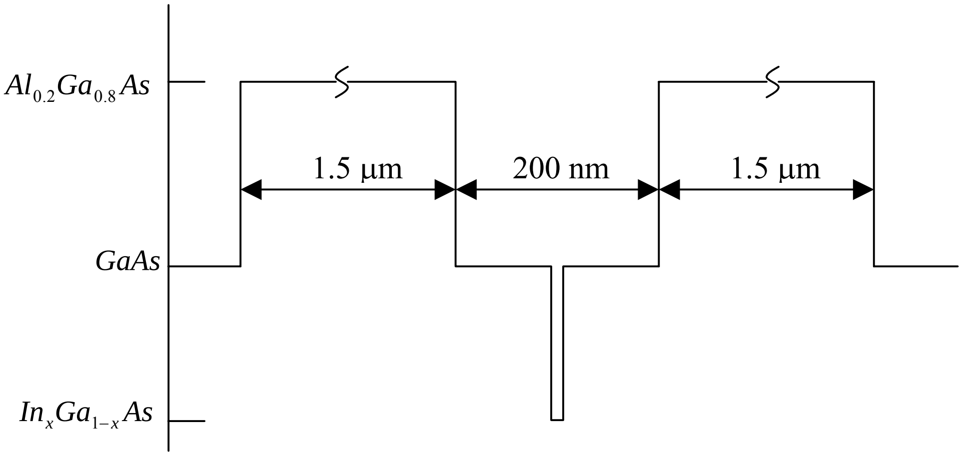

(b)

Fig. 6.1 (a) Epitaxial layer structure and (b) conduction band diagram of the separate confinement heterostructure, HC0819.

cladding layer, and a p^+-doped ($10^{19} cm^{-3}$) 200 nm thick GaAs cap for Ohmic contact. In the active region, 0.5 ML InAs and 2.5 ML GaAs were alternately deposited for 10 times at 500 $^\circ C$, to form the SML QD layer. The growth conditions of SML QDs are the same as those of HCØ809 studied in Chapter 5. During the growth of 100 nm GaAs confining layer after the active region, the temperature of the substrate was gradually increased from 500 $^\circ C$ to 600 $^\circ C$. All the other layers were grown at 600 $^\circ C$, as measured by an optical pyrometer. The wafer was not rotated during the growth. The growth rates were calibrated by using the RHEED intensity oscillations from the center of the wafer. A schematic diagram of the epitaxial layers and the conduction band diagram for such a device are shown in Fig. 6.1.

6.2 Room Temperature Photoluminescence

In this section, room temperature PL from the SML InGaAs/GaAs QDs inside the laser structure is investigated. A He-Ne laser at the wavelength of 632.8 nm is used as the excitation source. This excitation size is about 50 μm in diameter. The excitation power is $136 W / cm^2$, if there is no further explanation.

6.2.1 Sample Preparation

In order to observe PL from the SML QDs inside the laser structure, the thick top layers including the contact layer and the cladding layer, were removed by wet chemical etching. The etchant that we used was

$1\,H_3PO_4$: $1\,H_2O_2$: $38\,H_2O$. The etching rate of $Al_{0.2}Ga_{0.8}As$ is around 170 nm per minute. The optimum etching time was found to be 10.5 mins, which corresponds to the maximum PL intensity from the SML QDs, as shown in Fig. 6.2. The PL peaks from SML QDs and GaAs are clearly shown in the inset of Fig. 6.2.

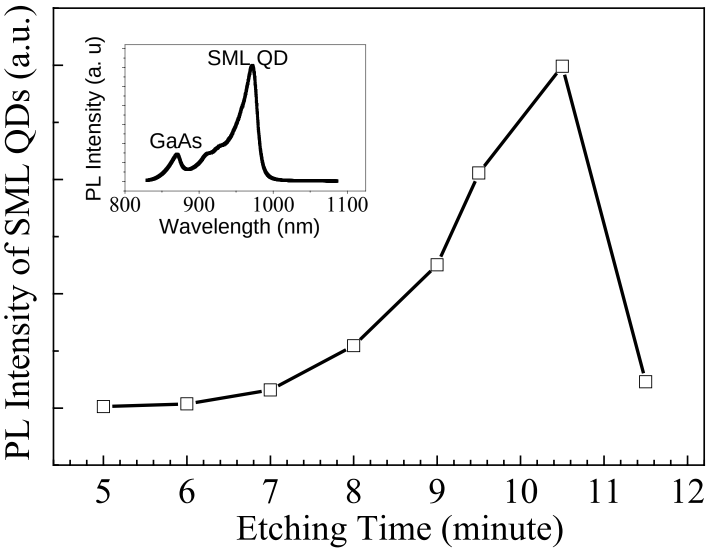

Fig. 6.2 PL intensity of SML QD structures as a function of etching time. The inset shows the PL spectrum after etching the laser structure for 10.5 minutes.

6.2.2 Power Dependence of Photoluminescence

As shown in Fig. 6.3, the PL spectra evolve into a continuum band from 830 nm to 1050 nm, when the excitation power density decreases to 1.27 W/cm^2. As the PL experiments were carried out in the back-scattering geometry, with a He-Ne laser at 632.8 nm as the excitation source, the photon-carriers are mainly generated by absorption of the incident laser light inside the Si-doped GaAs layers beneath the SML QD layer. The photon-generated carriers will first be captured by the deep-level states in GaAs and then excess carriers will be diffused into and captured by SML QDs. When the excitation is too low, few photon-generated carriers can reach QDs and only the emission from the Si-doped GaAs, i.e., the broadband emission can be detected. This broadband emission has been extensively studied and is attributed to the Si-Ga vacancy complex (Si_{Ga}-V_{Ga}) [86]. The presence of these deep-level defect states would lead to large internal losses and high threshold current, which will be studied in Section 6.5.

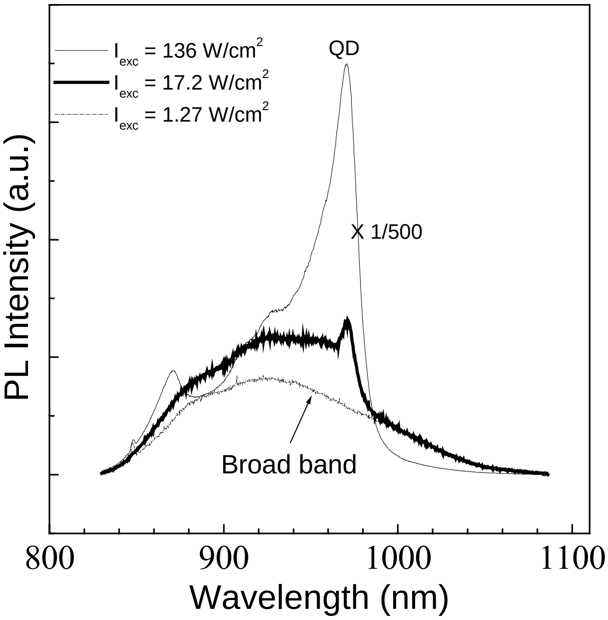

Fig. 6.3 Power dependence of PL from the SML QD structures, and the doped GaAs wave-guide in HC0819

6.2.3 Position Dependence of Photoluminescence

As the wafer was not rotated during the growth, the emission wavelength changes gradually across the wafer, depending on the wafer azimuth with respect to the sources, as shown in Fig. 6.3. Point A is the nearest to Ga and In sources, corresponding to the longest emission wavelength. Note that not only the emission wavelength varies across the wafer, but the full width at half maximum (FWHM) is also position dependent. The center wavelengths (FWHMs) for A, B, and C are 977.7 nm (17.8 nm), 963.2 nm (22.5 nm), and 952.7 nm (20.3 nm), respectively. Different FWHMs indicate that the size distribution of QDs can be different at different positions on the wafer.

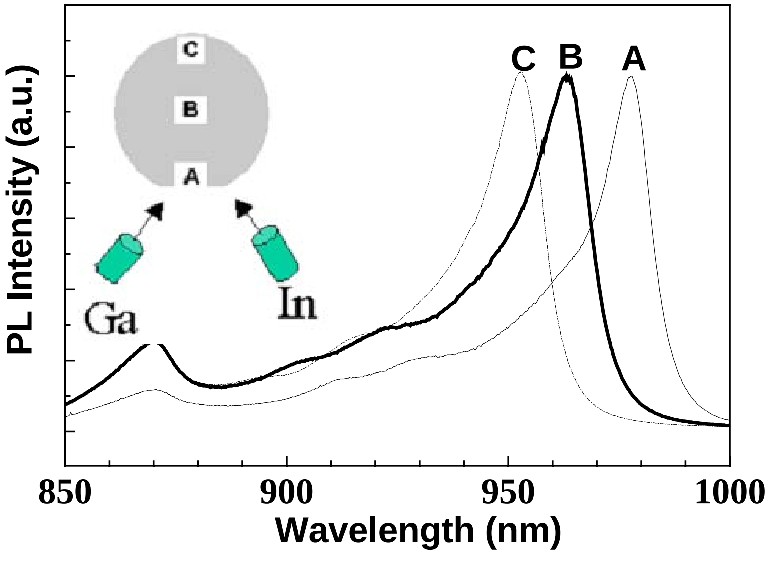

Fig. 6.4 Room temperature PL spectra at different points across the wafer.

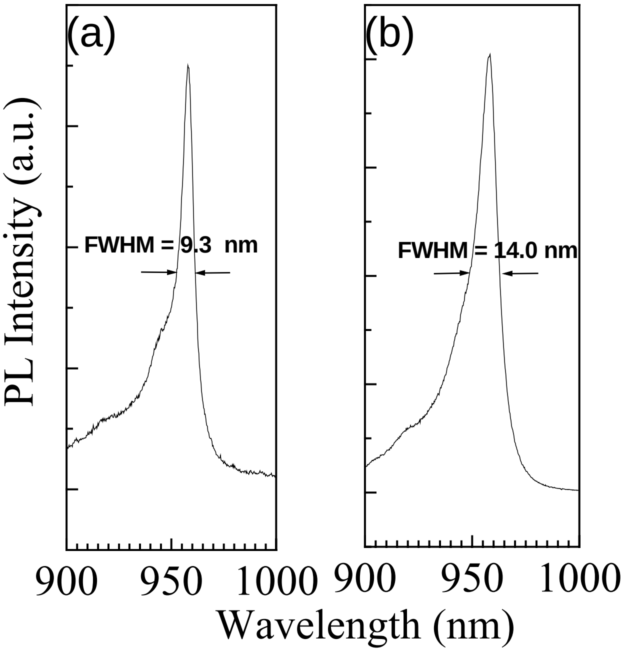

Fig. 6.5 Extremely narrow PL band from SML InGaAs/GaAs QDs at room temperature, (a) at the excitation power density of $50 W/cm^2$;(b) at the excitation power density of 136 W/cm^2. The emission wavelength is 958.2 nm.

For one sample between point B and C, when the excitation power density is as low as 50 W/cm^2, the FWHM of QD PL band is found to be as small as 9.3 nm (12.5 eV) at room temperature, as shown in Fig. 6.5. ***This is the lowest value for a self-assembled QD ensemble, to the best of our knowledge, indicating SML deposition technique is quite effective for growing QD arrays with high uniformity.*** At room temperature, the shortest emission wavelength (952 nm) among all the investigated samples is longer than 940 nm in Ref. [11,12], though the growth sequence and the nominal deposition amount are the same. This is probably due to the different growth conditions, such as growth rates, V/III flux ratios, and substrate temperatures.

6.2.4 Polarization of Photoluminescence

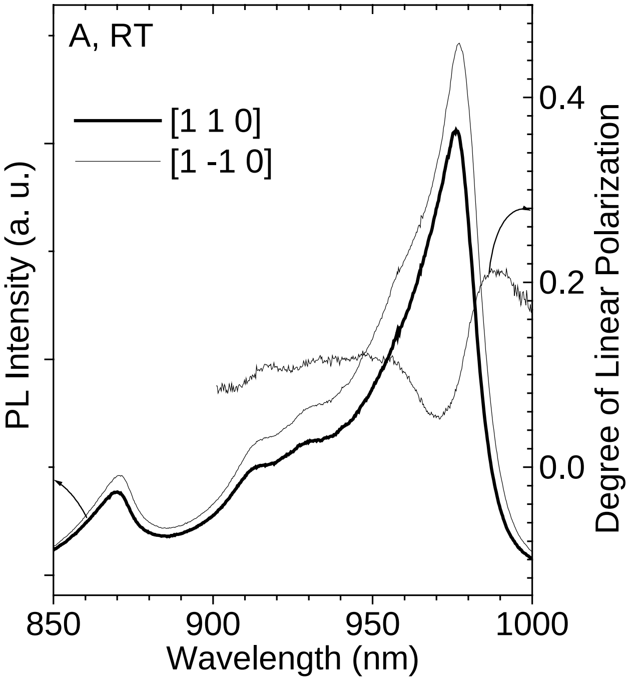

Fig. 6.6 PL spectra and the degree of linear polarization detected along the $[001]$ direction in the backscattering geometry.

Fig. 6.6 shows the PL spectra at Position A, polarized along the $[110]$ and the $[1\bar{1}0]$ directions. The PL signal was detected along the $[001]$ direction. The degree of linear polarization is defined as $\frac{I_{[1\bar{1}0]} - I_{[110]}}{I_{[1\bar{1}0]} + I_{[110]}}$. It is clearly shown that the intensity of PL polarized along the $[1\bar{1}0]$direction is stronger than that along the $[110]$ direction. The degree of the in-plane polarization ranges from 5% to 21%. The larger QDs emitting at longer wavelength show bigger in-plane optical anisotropy than smaller QDs emitting at shorter wavelength. Sample B and C also show similar polarization properties as Sample A.

6.3 Fabrication of Broad-Area SML InGaAs/GaAs QD Lasers

Several broad-area SML InGaAs/GaAs QD lasers were fabricated from wafer HCØ819, according to the following steps: 1) a 4000-nm thick SiO_2 film was formed on the surface of the wafer, by using a glass deposition facility; 2) 50 μm (or 100 μm)-wide SiO_2 stripes were removed by photolithography and chemical etching; 3) the substrate was mechanically polished until the thickness decreases to about 100 μm, in preparation for cleaving; 4) The n-side contact, consisting of 400 Å Germanium, 600 Å Gold, 270 Å Nickel and 2000 Å Gold, was evaporated onto the substrate; 5) The p-side contact was deposited and consisted of 100 Å Chromium and 1500 Å Gold. 6) Each sample was then cleaved into bars perpendicular to the stripes, forming cavity lengths between 500 μm and 2000 μm. No coatings were applied to the facets.

6.4 Basic Characterization of SML InGaAs/GaAs QD Lasers

In this section, the basic characteristics of a 628 μm-long SML InGaAs/GaAs QD laser with a 100 μm-wide stripe (Device A) will be presented.

6.4.1 Experimental Set-up

Fig. 6.7(a) shows the schematic diagram of the experimental set-up for characterizing the QD laser diodes. The device is mounted with the n-side down on a thermoelectric cooler. Lights emitted from the laser diode under current injection are collected by Lens L1 and then converted into a quasi-parallel beam by Lens L2. After a size-tunable hole H1, the emitted light is coupled into the slit of a monochromator, with the reflection mirrors M1, M2 and Lens L3. Inside the monochromator, the light is dispersed by two mirrors and a grating, and finally detected by a Si CCD. Between Lens L1 and L2, an attenuator A1 is used to adjust the beam intensity and a polarizer is used to investigate the polarization of emitted lights. The luminescence spectrum is processed and acquired by a computer. The use of a size-tunable hole H1 is to remove the interference of a large number of lateral modes, which will affect the measurement of the gain and the refractive index. This is called the "far-field spatial filtering" technique [87]. All measurements were performed under pulsed excitation to eliminate additional heating caused by the drive current. The pulse width is 0.2 μs, and the duty cycle is 0.1%. Fig. 6.7 (b) shows the picture of the set-up.

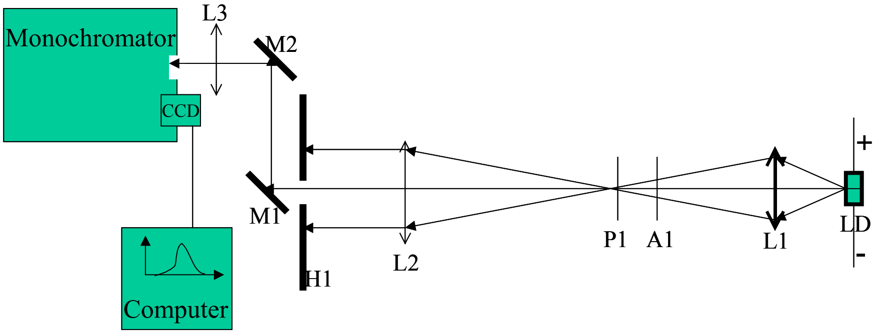

(a)

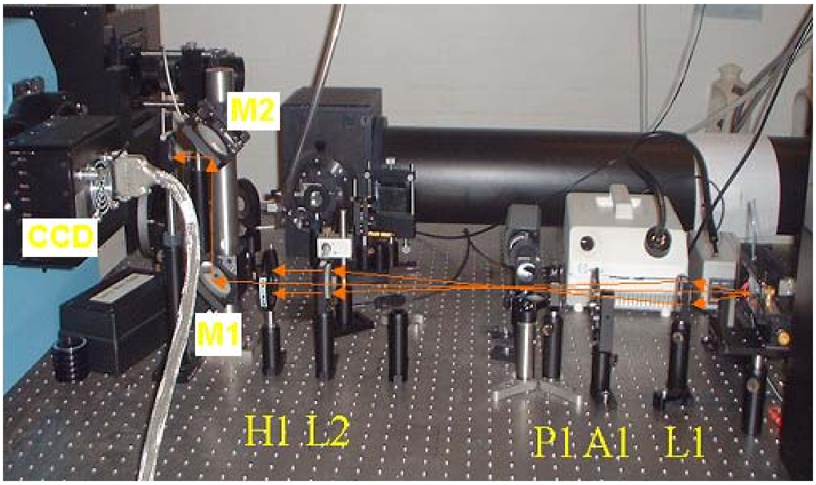

(b)

Fig. 6.7 Experimental setup for characterizing the laser diodes, (a) the schematic diagram, LD: Laser diode, L1,L2,L3: Lenses, A1: Attenuator, P1: Polarizer, H1: Size-tunable hole, M1,M2: reflection mirrors; (b) the picture of the setup.

6.4.2 Light-Current Characteristics

To measure the light-current characteristic, we put a power meter very close to the laser diode. The power of the output from one facet was measured while tuning the injection current at 30 ^{0}C. Fig. 6.8 shows the total output power from two facets versus the injection current. From Fig. 6.8, the threshold current is found to be 235 mA, corresponding to a current density of 373 A/cm^2. The slope efficiency is 0.32 W/A.

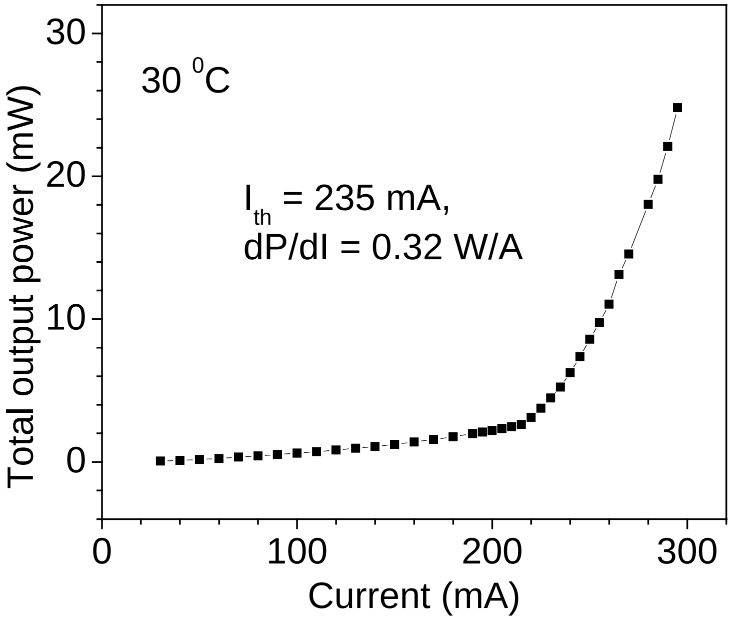

Fig. 6.8 Light output characteristic of a broad-area ($100\mu m \times 628\mu m$) SML InGaAs/GaAs QD laser.

6.4.3 Lasing Spectra

Fig. 6.9 shows the electroluminescence (EL) spectra of the transverse electric (TE) components at different currents at 30 ^{0}C. At 100 mA, the spectrum is broad with central emission wavelength at 964.8 nm and FWHM of 29.1 nm, corresponding to the spontaneous emission from the QD ground states. At 250 mA, the spectrum is very sharp and centred at 964.3 nm, corresponding to the stimulated emission. As the current increases, the lasing spectrum broadens and the central lasing wavelength gradually coincides with the peak wavelength of the spontaneous emission.

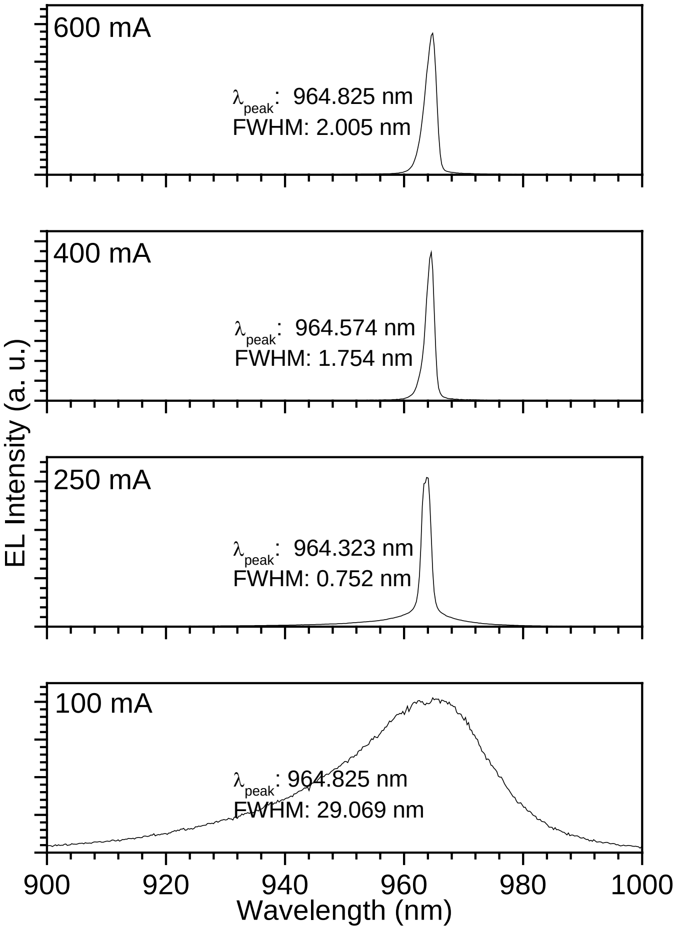

Fig 6.9 Electroluminescence spectra at different currents at 30 ^{0}C. A grating with 150 grooves per mm is used for the measurement.

6.4.4 Temperature Properties

6.4.4.1 Characteristic Temperature

Fig. 6.9 shows the current-power curves at different temperatures. It can be seen that the threshold current increases with the increase of temperature. For a certain range, the measured threshold current I_{th} of a laser can be described by an exponential temperature-dependence [88]:

$$I_{th} = I_0 \exp(T / T_0) . \tag{6.1}$$

In general, the parameters I_0 and T_0 depend on the temperature themselves but can be approximated with constant values for a certain temperature range. The relationship between the threshold current and temperature for the device is shown in Fig. 6.11. T_0 is found to be about 81K, lower than the recently reported value of 150K for the 0.94 μm SML QD lasers [12].

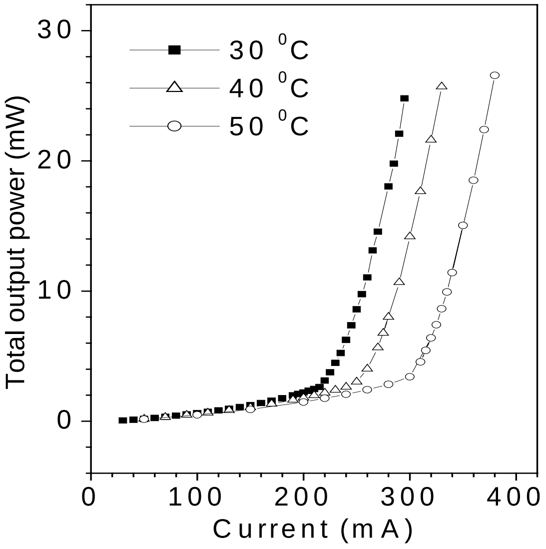

Fig. 6.10 Output power versus current at different temperatures.

6.4.4.2 Lasing Wavelength

The temperature dependence of the lasing wavelength for SML InGaAs/GaAs QD lasers has not been reported in the literature. Fig. 6.12 shows the lasing spectra at different temperatures, for Device A. The spectra red-shift as the temperature increases. The variation of the lasing wavelength with respect to temperature is shown in Fig. 6.13. It can be seen that, the wavelength increases almost linearly with a slope of 0.282 nm/K, which corresponds to a decrease of the emission energy of –0.38 meV/K. This value is 48% larger than the reported values (0.19 nm/K) of SK QD laser diodes emitting at 980 nm at room temperature [89], probably due to the lower potential confinement in the SML QD laser than that in the SK QD laser.

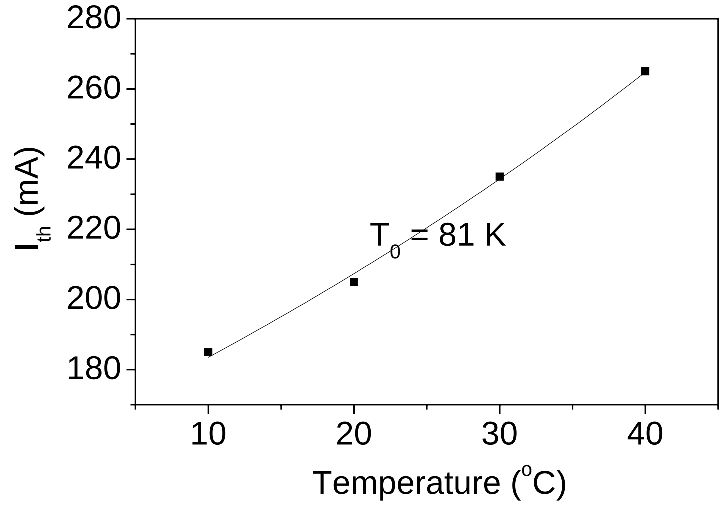

Fig. 6.11 Threshold current vs device temperature.

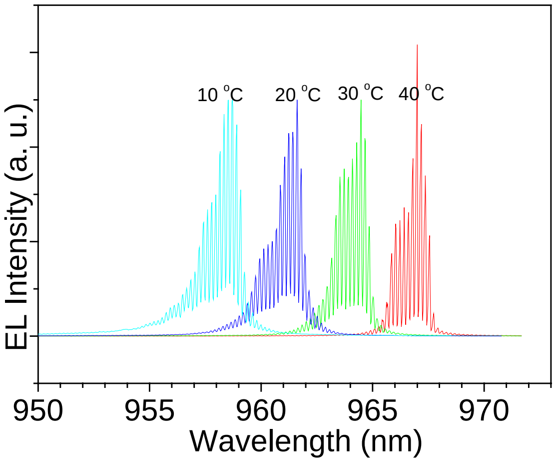

Fig. 6.12 Lasing spectra at different temperatures. A grating with 1200 grooves per mm is used for measurement. The injection current is 300mA.

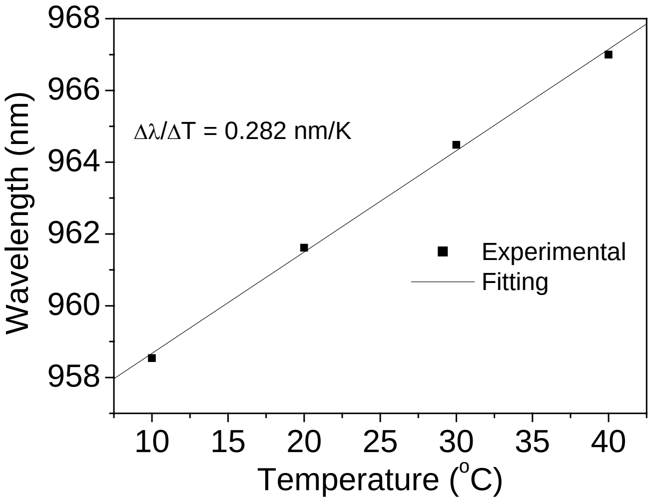

Fig. 6.13 Lasing wavelength versus device temperature.

6.4.5 Polarization Properties

We note that both the stimulated and lasing emission contain both TE and transverse magnetic (TM) components, which point to the QD nature of the emission. Fig. 6.14 shows the spectra in both modes at 100 mA (below the threshold) and 235 mA (at the threshold). The intensity ratio between the TE mode and the TM mode for the ground state transition (E-HH1) is 33 above the threshold, and it is 44 below the threshold. For comparison, the TE and TM spontaneous emission spectra of an $In_{0.2}Ga_{0.8}As/GaAs$ quantum well (QW) laser (HCØ799) below its threshold are shown in Fig. 6.15. The intensity ratio between the TE mode and the TM mode for the ground state of the QW laser is found to be 1.6×10^{6}, much higher than that of SML QD lasers. The stronger contribution of the TM mode to the luminescence signal for the SML QD laser, is due to the lateral confinement of carriers in QDs.

Two peaks can be clearly seen in the TM spectra both in Fig. 6.13 and in Fig. 6.14. The peak lying at higher energy originates from the excited state transition of E-HH2, as the transition of E-LH should be TM-polarized, which has not been observed here. The biaxial compressive strain separates the HH and the LH subbands by pulling down the HH bands and pushing away the LH subbands from the valence-band edge[90]. Here, the symbol “E” refers to the electron state, “HH” the heavy-hole state and “LH” the light-hole state. The gain difference in the TE and TM modes will be analyzed in Section 6.5.4.

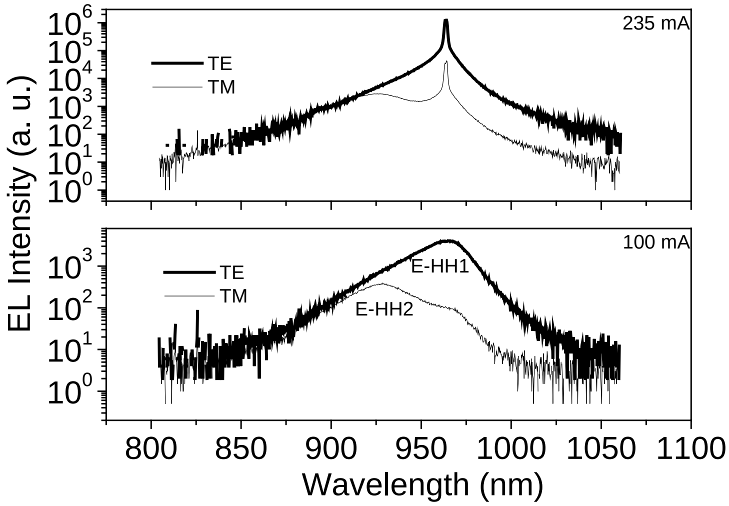

Fig. 6.14 TE- and TM- polarized electroluminescence spectra of an SML InGaAs/GaAs QD laser below (100mA) and above (235 mA) the lasing threshold.

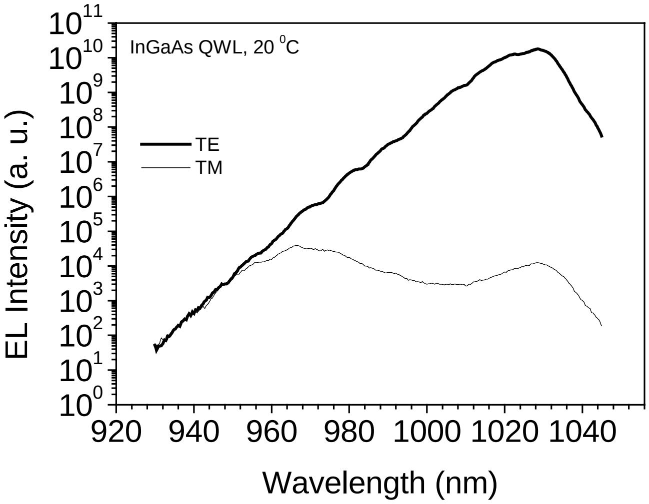

Fig. 6.15 TE- and TM- polarized electroluminescence spectra of an InGaAs/GaAs QW laser below (90mA) its lasing threshold.

6.5 Gain, Quantum Efficiency and Linewidth Enhancement Factor

In this section, the modal gain, the internal loss, the quantum efficiency, and the linewidth enhancement factor of an SML InGaAs/GaAs QD laser (Device A) are investigated in detail. The device temperature was set to be $30\,^{o}C$.

6.5.1 Gain Determined by Using the Hakki-Paoli Method

The gain spectrum of the laser is measured by using the Hakki-Paoli method [91]. Below the threshold, light spontaneously emitted within the laser cavity undergoes repeated reflections by the end mirrors and is subject to either constructive or destructive interference, depending upon the round-trip-path length. The intensity of the light emitted from the device is, hence, modulated by a series of Fabry-Perot-like oscillations (see Fig. 6.16). The difference between the modal gain g_{mod} and internal loss α_i, i.e., the so-called net modal gain $g_{net} = g_{\mathrm{mod}} - \alpha_i$, is related to the peak-to-valley ratio r of these oscillations by

$$g_{net} = \frac{1}{L}\ln\left(\frac{r^{1/2}-1}{r^{1/2}+1}\right) - \frac{1}{2L}\ln(R_1 R_2)\,, \tag{6.2}$$

where L is the cavity length and R_1 and R_2 are the power reflectivity of the cleaved facets. The last term in (6.2) is the mirror loss α_m. Hence, by measuring r as a function of wavelength, the spectrum of the net modal gain can be determined. In the long wavelength limit, g_{mod}

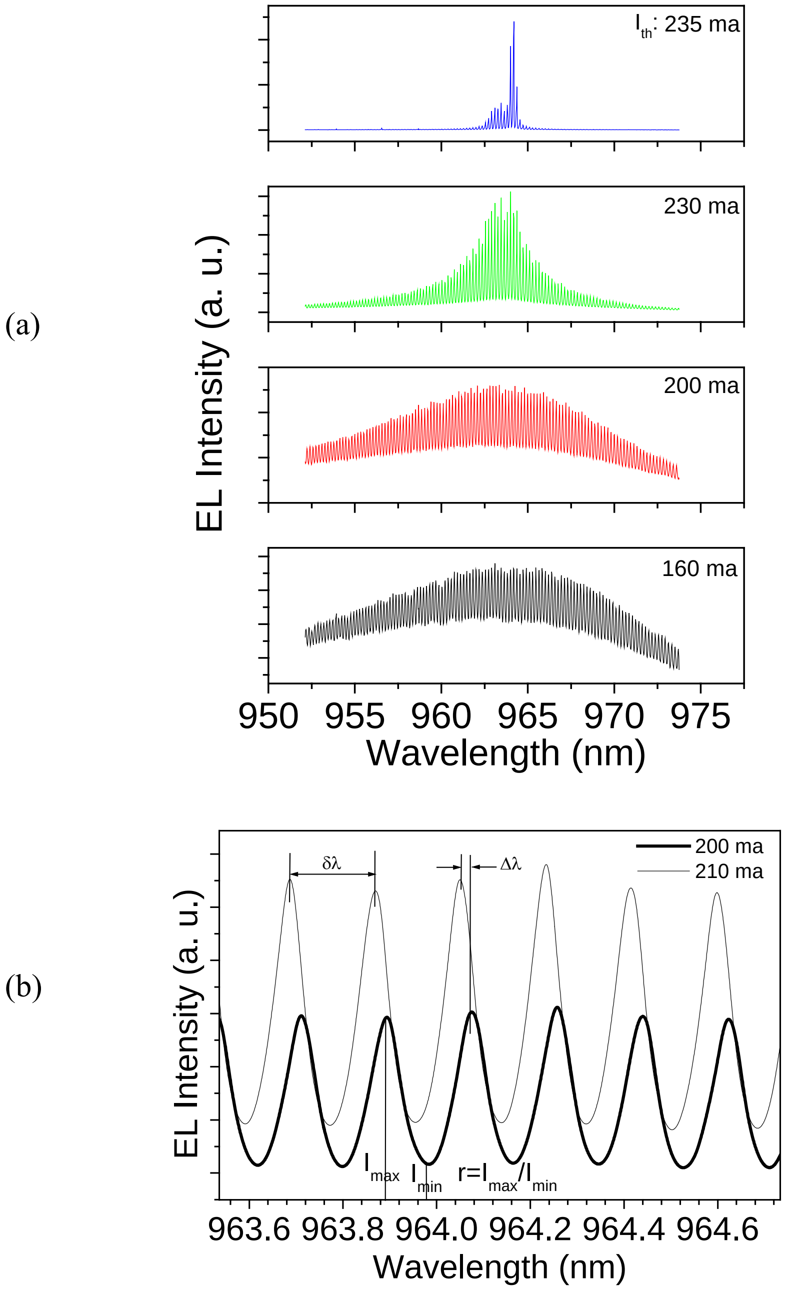

Fig. 6.16 (a) Amplified spontaneous spectra from an SML InGaAs/GaAs QD laser at different currents bellow the threshold. (b) Blushift in FP modes is observed near the threshold.

approaches zero, therefore, the measured g_{net} will be equal to $-\alpha_i$ [92] and then the spectrum of the modal gain can be obtained.

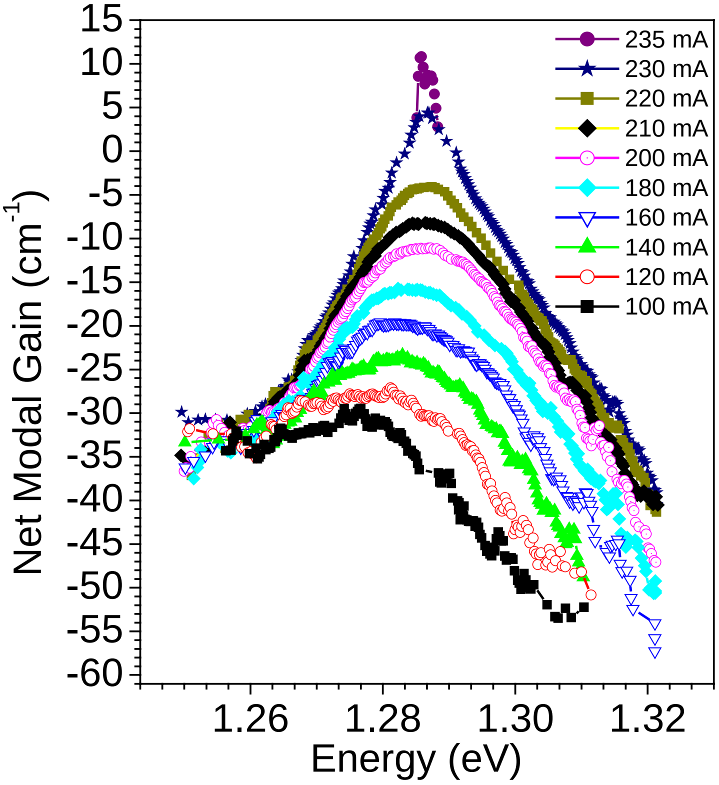

Fig. 6.17 Net modal gain spectra of an SML InGaAs/GaAs QD laser at different injection currents.

Fig. 6.16 (a) shows the typical emission spectra at 160 mA, 200 mA, 230 mA and 235 mA (I_{th}). It can be seen that the spectrum becomes symmetric with respect to the lasing wavelength when the current is 230 mA (0.98I_{th}). In Fig. 6.16(b), the blueshift in FP modes can be clearly seen when increasing the injection current near below the threshold. Fig. 6.17 shows the net modal gain spectra at several currents below threshold (I_{th}). The mirror reflectivity is assumed to be 0.35, corresponding to a mirror loss α_m of $16.7cm^{-1}$. As can be seen from Fig. 6.17, the maximum of the gain spectrum curve moves towards higher photon energies with increasing the injection current. As this takes place, the gain spectrum shape becomes more symmetric neat its maximum. When the current is 230 mA, just below the threshold, the half width of the gain spectrum is as narrow as 26.7 meV, comparable to kT at room temperature. This value is 2-3 times narrower than that of typical SK InAs/GaAs QD lasers at the lasing threshold [93]. The narrow gain spectrum of the SML QD laser is due to high uniformity of the QD arrays.

At the low energy limit (1.25 eV) the spectra converge ($g_{net} = -33 \pm 1cm^{-1}$), for the modal gain at this wavelength is zero at any current [92]. Therefore, the internal loss should be about $33\,cm^{-1}$. The internal loss of the SML QD lasers in Ref. 11 is only 2.3 cm^{-1}, much less than that of our device. The large internal loss in our device is probably induced by the doped waveguide region and can be related to the observed broadband emission in Section 6.2.2. The largest value of the internal loss in a SK InGaAs/GaAs quantum dot laser was reported to be 35 cm^{-1} in Ref. [94,95].

With the value of internal loss, we can simply convert the net modal gain spectra into the modal gain spectra. At the lasing threshold, only the spectra within a narrow region around the lasing wavelength can be used to evaluate the gain. The measured maximum net modal gain is found to be 10.9 cm^{-1}, corresponding to the maximum modal gain of about $43.9cm^{-1}$. The maximum modal gain of QD ground states for a single sheet of SK InGaAs/GaAs QDs is about $(11 \pm 4)\ cm^{-1}$ [96,97], 16.6 cm^{-1}[98], 18.5 cm^{-1}[99], 20 cm^{-1}[100], 24 cm^{-1}[101] and 33.8 cm^{-1}[102]. The maximum modal gain of QD ground states was reported to be about 30 cm^{-1} for an SML QD laser with two sheets of QDs [12], corresponding to 15 cm^{-1} per QD sheet. ***Our result represents the highest value of the modal gain of QD ground states for a single sheet of self-assembled QDs, to the best of our knowledge.*** The high modal gain is due to the high density of QDs embedded in our devices.

6.5.2 Internal Differential Quantum Efficiency

The external differential quantum efficiency of a laser diode η_D is defined as the ratio of the increase in the number of output photons for a given increase in the number of injected electrons, and can be written as

$$\eta_D = \frac{e}{\hbar\omega}\frac{dP}{dI}, \tag{6.3}$$

where $\hbar\omega$ is the laser emission energy and $\frac{dP}{dI}$ the slope of the light-current characteristic. η_D depends on the injection efficiency (the fraction of the injected carriers contributing to the emission process) and on the optical efficiency (the fraction of the generated photons that are transmitted out of the cavity). According to the slope efficiency determined in Section 6.4.2, η_D will be 0.233. The internal differential quantum efficiency η_i can be determined by[103]

$$\eta_i = \eta_d\left(1 + \frac{\alpha_i}{\alpha_m}\right) \tag{6.4}$$

From Section 6.5.1, $\alpha_i = 33cm^{-1}$ and $\alpha_m = 16.7cm^{-1}$, so η_i is 0.69. This is value is lower than 1.0, which was reported in Ref. 11 ,104, indicating the crystal quality of our SML QDs can be further improved by optimizing the growth conditions.

6.5.3 Linewidth Enhancement Factor

The linewidth enhancement factor, α, is a key parameter that determines the spectral properties of semiconductor lasers and semiconductor optical amplifiers. It characterizes the linewidth broadening due to fluctuations in the carrier density altering the refractive index. The α factor is the ratio of the real and the imaginary part of the differential susceptibility with carrier density. The real part of the susceptibility is related to the differential gain that is proportional to the imaginary part through the Kramers-Kronig (KK) transformation. Since the spectral linewidth of semiconductor lasers is proportional to $n_{sp}.(1+\alpha^2)$, where n_{sp} is the spontaneous emission rate, the α factor has to be reduced in order to obtain a narrow spectral linewidth. In high-power semiconductor laser applications, the linewidth enhancement factor must be minimized in order to reduce filamentation effect. The linewidth enhancement factor is given by the relation [105]

$$\alpha \approx -\frac{2\pi}{\delta\lambda \cdot L} \cdot \frac{\Delta\lambda / \Delta I}{\Delta g_{net} / \Delta I}, \tag{6.5}$$

where $\delta\lambda$ is the Fabry-Perot mode spacing, L is the cavity length, $\Delta\lambda / \Delta I$ is the change in wavelength with current (or equivalently, the change in refractive index with pumping current), and $\Delta g_{net} / \Delta I$ is the change in net modal gain with current. The wavelength shift with current, $\Delta\lambda / \Delta I$, can be obtained by measuring the change in wavelength of the Fabry-Perot mode near the threshold. $\Delta g_{net} / \Delta I$ can be obtained from the gain spectra in Section 6.5.1.

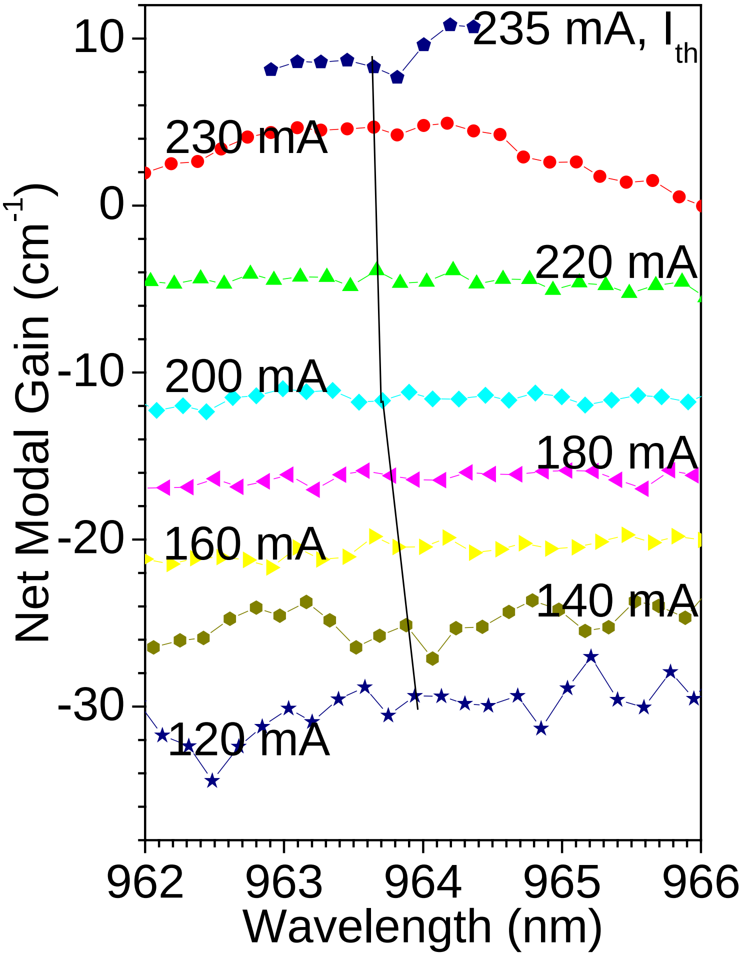

Fig. 6.18 Net modal gain versus wavelength derived from the ratio of peak to valley heights for different injection currents below the threshold. The graph markers denote the position of the fringe peaks.

Fig. 6.18 shows the gain spectra in a narrow region around the lasing wavelength. The dot markers in Fig. 6.18 are placed to indicate the location of the Fabry-Perot peaks. From 962 nm to 966 nm, the gain spectrum is relatively flat for each current set. This is quite different from QW lasers, which would show a definite gain roll-off across this range. The vertical line in Fig. 6.18 is to show the evolution of the Fabry-Perot peaks due to the change of current.

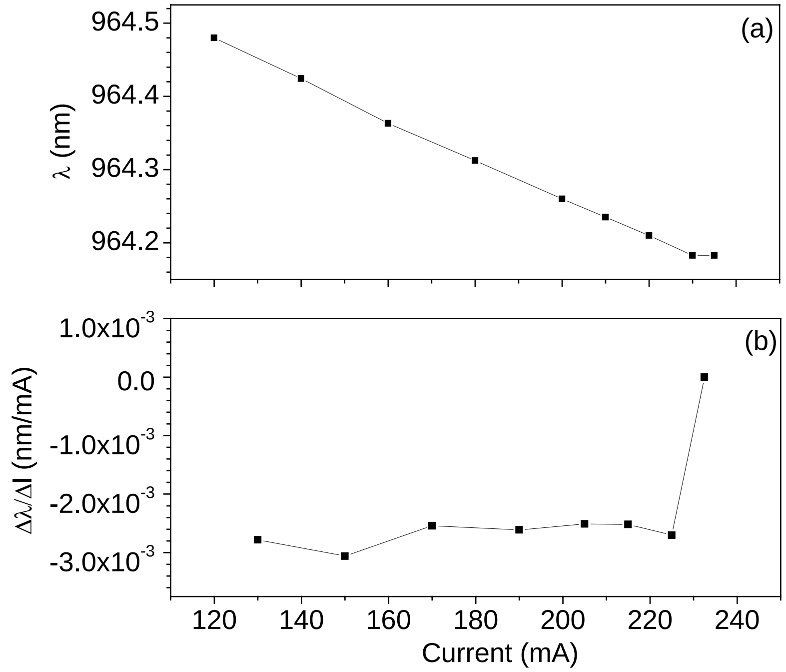

Fig. 6.19 Wavelength (a) and its shift (b) vs. current for the lasing mode.

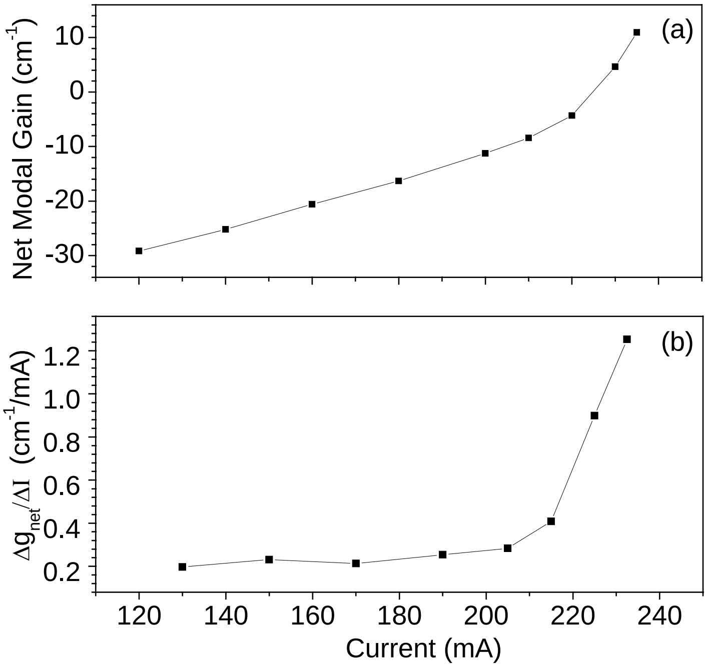

Fig. 6.20 Net modal gain (a) and differential gain (b) vs. current at lasing wavelength.

Fig. 6.19 shows the wavelength λ and the shift $\Delta\lambda/\Delta I$ as a function of current, for the lasing mode. In Fig. 6.19(b), the abscissa of the graph markers are placed at the average of the two current levels used from Fig. 6.19(a). As the current increase, the wavelength blueshifts at a constant rate $\Delta\lambda/\Delta I$ of $2.5\times10^{-3}\,nm/mA$ for the current below $0.98\,I_{th}$, and then almost does not shift, resulting in a drastic decrease of $|\Delta\lambda/\Delta I|$, which is zero from $0.98\,I_{th}$ to $1.0\,I_{th}$. Fig. 6.20 shows the net modal gain and the differential gain $\Delta g_{net}/\Delta I$ as a function of current at lasing wavelength. The abscissa of the graph

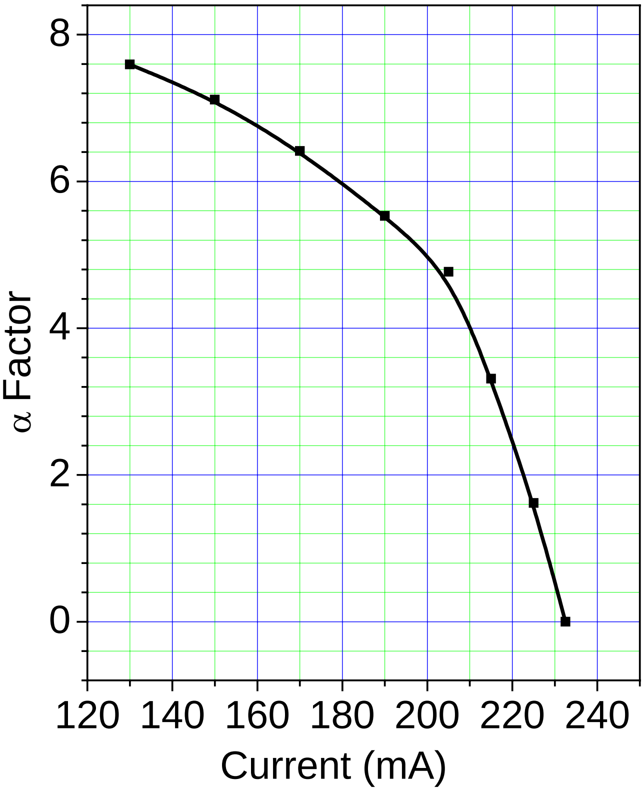

Fig. 6.21 Linewidth enhancement factor at the lasing wavelength as a function of current, for an SML QD laser. It becomes zero when the injection current approaches the threshold current. The line is the guide for the eye.

markers in Fig. 6.20 has the same meaning as in Fig. 6.19. The net modal gain increases linearly with the increase of current when the current is below 0.91 I_{th} , and then increases drastically. Correspondingly, $\Delta g_{net} / \Delta I$ is almost a constant below 0.91 I_{th} , and then increases drastically. These trends are in contrast to that of QW structures. In the latter case, the differential gain is highest at low current density, gradually decreasing with increasing the carrier density as the states associated with the $n=1$ transition fill. In addition, no saturation of the gain and the differential gain is observed below I_{th}, while saturation is very pronounced for typical SK-grown QD lasers[106,107], when the current is near to the threshold. This property results from the higher density of QDs in our lasers.

With the data in Fig. 6.19(b) and Fig. 6.20(b), the α factor is determined as a function of current for the lasing mode, as shown in Fig. 6.21. It can be seen that the α factor decreases to zero when the current increases to $0.98\,I_{th}$. ***This is the first observation of the zero linewidth-enhancement-factor at the lasing wavelength for QD lasers, to the best of our knowledge.***

When the current is far below the threshold current, the population probability of the carriers for different QDs with different energy levels is affected by the so-called phonon bottleneck [108], resulting in an asymmetric gain spectrum. However, when the current is very near to the threshold, the carrier-carrier scattering (Auger process) will be the dominant mechanism of carrier capture and relaxation [109], the population probability for all the QDs is almost the same, resulting in a very symmetric gain spectrum. In this case, the differential gain is also symmetric to the peak gain energy position where lasing occurs. Thus the change of the differential refractive index computed via the KK relation is exactly zero at the lasing energy (i.e., the peak gain position). For SK QD lasers with a single sheet of QDs, the ground states of QDs can be easily saturated due to the lower density of QDs. In that case, the contribution of excited states or wetting-layer states to the gain might cause an asymmetric gain curve, which increases the linewidth enhancement, depending on excitation level, to about 0.5 [110], 0.1[107] ,0.15 [106] or 0.7[111]. ***Our successful observation of the zero***

linewidth-enhancement-factor at the lasing wavelength is attributed to the high density of SML QDs in our devices.

6.5.4 Gain in the TE/TM Modes

Although the laser emission of our devices is TE polarized, the TM gain data are useful since they give us the information about the anisotropy of gain material. Fig. 6.22 shows the modal gain spectra measured in the TE and TM modes at 220 mA (0.936 I_{th}). It can be seen that the TE gain is larger than the TM gain, but the ratio between the maximum TE gain and maximum TM gain is only 1.21. This property is quite different from that for a QW laser. For compressively strained $In_{0.2}Ga_{0.8}As/GaAs$ QW lasers, the TE modal gain is expected to be substantially larger than the TM mode gain [90].

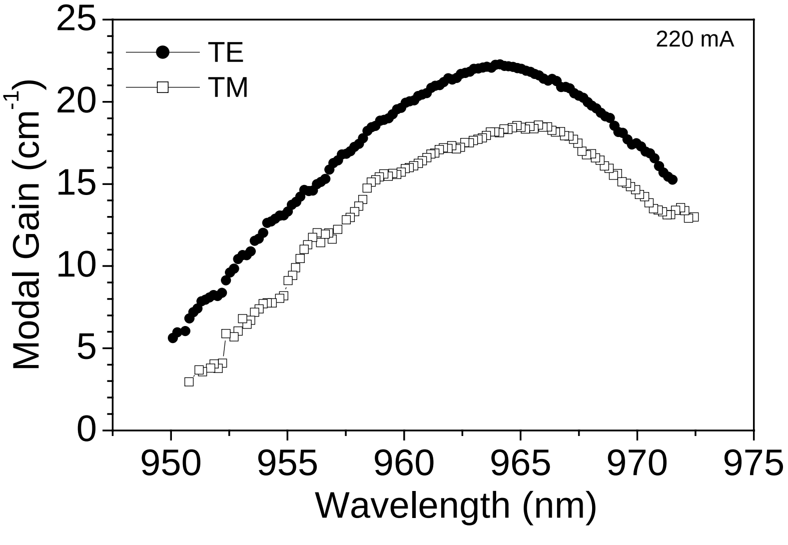

Fig. 6. 22 Modal gain in TE and TM mode at 220 mA (0.936 I_{th}).

6.6 Fourier Analysis of Amplified Spontaneous Emission Spectra

As we know, the formation of crystal defects at the facets or in the bulk of the epitaxial structure will limit the lifetime of semiconductor lasers. The internal defects or scattering centers will modulate the intensity distribution of the envelop of the amplified spontaneous emission (ASE) spectrum below the threshold [112]. Fourier transformation (FT) of the laser emission spectrum can be used to precisely determine the position of defects in diode lasers [113,114].

In this section, we will analyze the ASE spectra of three SML QD laser diodes fabricated from wafer HC0819, using the Fourier transform technique. Device A is the one that has been studied in the previous sections. Device B and C are other two laser diodes fabricated from HC0819, with a 525 μm-long cavity and a 100 μm-wide stripe. Device B and C are close to each other on the same laser bar.

Fig. 6.23 to 6.25 shows the ASE spectra and the corresponding FT of Device A, B, and C, respectively, below the threshold. The envelope of the spectrum of Device A is almost smooth, while those of Device B and C are distorted with a ripple-like modulation. This modulation indicates the presence of internal defects. In the FT spectra, the main peak at 628 μm for Device A (at 523 μm for Device B and C) corresponds to the longitudinal mode spacing and is related to the laser length according to $\Delta\lambda = \lambda^2 / 2nL$, where λ is the emission wavelength and n is the effective group index. For Device A, no additional peaks can be seen. However, two additional peaks at 91μm and 434 μm for Device B and four additional peaks at 87 μm, 120 μm, 400 μm and 438 μm for Device C, can be clearly seen. Because every defect creates

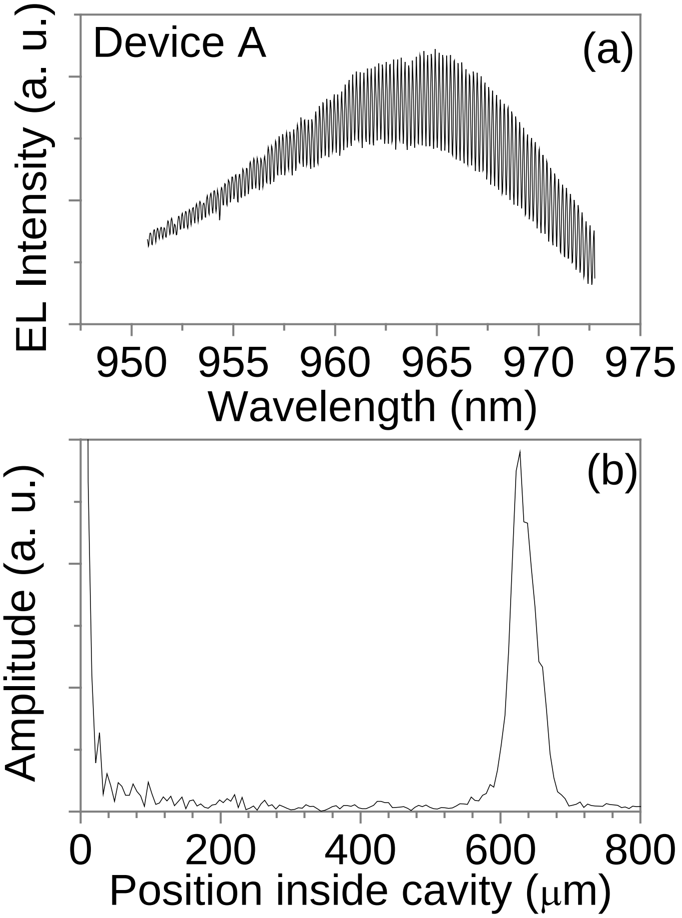

Fig. 6.23 The ASE spectrum (a) and the corresponding FT (b) of device A, at 200 mA (0.85 I_{th}).

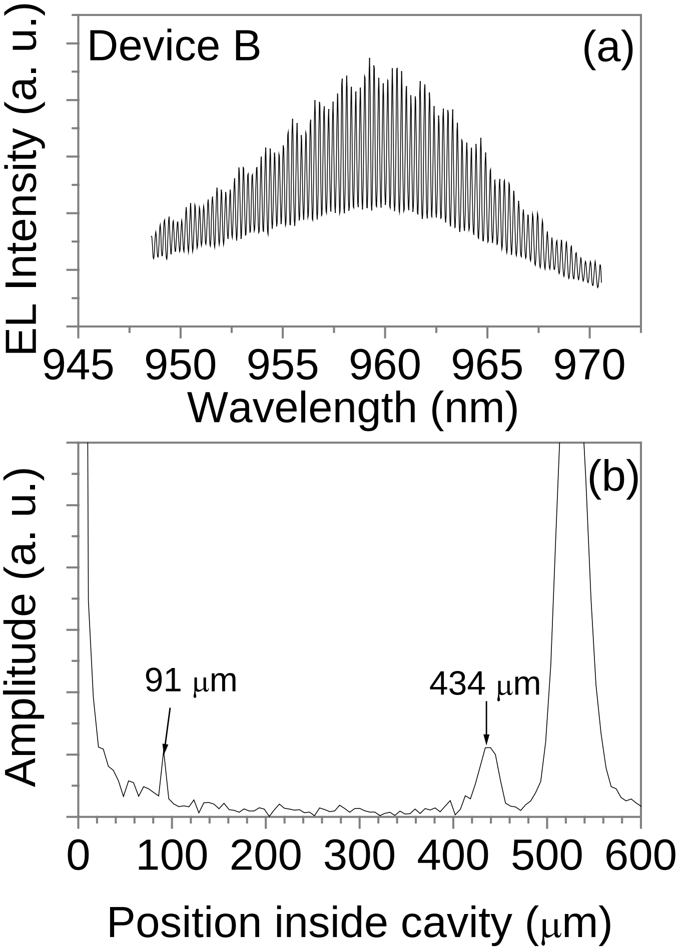

Fig. 6.24 The ASE spectrum (a) and the corresponding FT of Device B, at 210 mA (0.91 I_{th}).

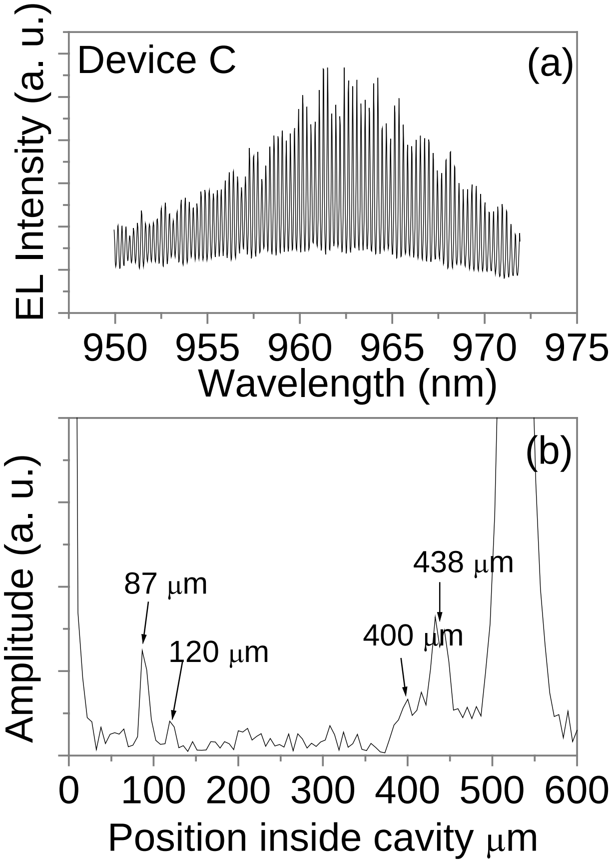

Fig. 6.25 The ASE spectrum (a) and the corresponding FT (b) of device C, at 210 mA(0.91 I_{th}).

two peaks at the location x and $(L-x)$, there is one detectable defect in Device B, while there are two in Device C. For Device C, the peaks at 87 μm and 438μm correspond to one defect, and the other two peaks correspond to a second one. From the FT analysis, Device A is better than Device B and C. This is the reason why Device A was studied in detail in the previous sections.

6.7 Conclusions

SML InGaAs/GaAs QD lasers, lasing from the QD ground states at room temperature, have been successfully realized. At 30 ^{o}C, the lasing wavelength, the threshold current density, and the characteristic temperature are 965 nm, 373 A/cm^2 and 81 K, respectively. The gain spectra of an SML InGaAs/GaAs QD laser diode, at 30 ^{o}C, have been measured by using the Hakki-Paoli method. It is found that the maximum modal gain for single-layer SML InGaAs/GaAs QD lasers is ***as high as 43.9*** cm^{-1} . No gain saturation takes place below the threshold, and the gain spectrum becomes symmetric with respect to the lasing wavelength when the injection current is about 0.98 I_{th}. ***The zero linewidth-enhancement-factor at the lasing wavelength for an SML InGaAs/GaAs QD laser has been observed, when the injection current is about 0.98*** I_{th}**.** These properties are attributed to the high density and the high uniformity of SML QDs in our devices. The gain in the TE mode is slightly larger than that in the TM mode, for an SML InGaAs/GaAs QD laser. Fourier transform of the ASE spectra of SML QD lasers is demonstrated to be a powerful method to recognize the defects inside the laser cavity.

Summary

In summary, this thesis mainly consists of two parts. In one part, the structure, optical properties and carrier dynamics of SML InGaAs/GaAs QD heterostructures are investigated. In the other part, SML InGaAs/GaAs QD lasers and their properties are studied. The SML InGaAs/GaAs QDs are formed by 10 cycles of alternate deposition of 0.5 ML InAs and 2.5 ML GaAs.

For the SML InGaAs/GaAs QDs grown at 480 ^{o}C, the following results have been obtained:

(a) Plan-view TEM observation shows that SML QDs are slightly elongated along the [1 –1 0] crystal direction, and the QD density is extremely high (> 10^{11} cm^{-2}).

(b) ***For the first time, the SML InGaAs/GaAs QD heterostructure is verified to be a quantum-dot-quantum-well structure,*** i.e., the Indium-rich QDs are embedded in a QW with lower Indium content, by using optical characterization techniques.

(c) As the temperature increases, a sigmoidal behavior of the PL peak energy and a narrowing of the PL linewidth of the SML QD ensemble are observed, and explained by carrier transfer from smaller dots to larger dots via QW states. At room temperature, the PL signal of QDs quenches due to the thermal escape of carriers from QD to QW states.

(d) Phonon-resonant PL bands and different local phonon modes, from the lateral QW, the QDs, the interfaces and the GaAs barrier are observed in the resonantly excited PL peaks.

(e) In the edge geometry, strong contribution of the TM mode to PL signal has been observed, indicating the vertical coupling of the SML InAs islands in the GaAs matrix.

(f) The PL rise time (~ 35 ps) and decay time (~ 700 ps) of the ground states of SML QDs, at 5 K, are found to be comparable to those of typical SK QDs. The decrease of the PL rise time when increasing the exaction power density has been observed, as result of the increasing probability of carrier capture to QD states via the Auger mechanism.

(g) The HRXRD analysis shows that the vertical lattice mismatch of the InAs monolayer with respect to GaAs is around 1.4%, while the lattice mismatch in the QW is negligible.

For the SML InGaAs/GaAs QDs grown at 500 ^{o}C, the PL signal from QD ground states is observable even at room temperature. In the edge geometry, strong contribution of the TM mode to PL signal is also observed.

We succeeded in fabricating SML InGaAs/GaAs QD broad area lasers. The growth temperature for the SML QDs inside the laser device was 500 ^{o}C. The lasing wavelength, the threshold current density, and the characteristic temperature of an SML InGaAs/GaAs QD broad area laser with a 628 μm-long cavity and a 100 μm-wide stripe, are 965 nm, 373 A/cm^2 and 81 K, respectively, at 30 ^{o}C. By using the Hakki-Paoli method, the gain spectra at 30^{o}C were measured. ***It is found that the maximum modal gain of QD ground states is 43.9 cm^{-1}, which is the highest value obtained for a single sheet of In(Ga)As/GaAs QDs, to the best of our knowledge.*** This property is very useful for high power lasers. Furthermore, no gain saturation takes place below the threshold, and the gain spectrum becomes symmetric with respect to the lasing wavelength when the injection current is about 0.98 I_{th} . The Zero linewidth- enhancement-factor at the lasing wavelength has been observed, when the injection current is about 0.98 I_{th} . ***This is the first time for the zero linewidth-enhancement-factor to be observed for a QD laser.*** These properties are attributed to the high density and the high uniformity of SML QDs in our laser diodes.

References

[1] D. Bimberg, M. Grundmann and N.N.Ledentsov, *Quantum Dot Heterostructures* (John Wiley & Sons, 1999).

[2] Y. Arakawa and H. Sakaki, “Multidimensional quantum well laser and temperature dependence of its threshold current”, Appl. Phys. Lett., **40**(1982)939.

[3] M. Aseda, et al., “Gain and the threshold of the three dimensional quantum-box lasers”, IEEE J. Quantum Electron., **22**(1986)1915.

[4] T. Fukui et al., “GaAs tetrahedral quantum dot structures fabricated using selective area metalorganic chemical vapor deposition”, Appl. Phys. Lett., **58**(1991)2018.

[5] H. Hirayama, et al., ” Lasing action of $Ga_{0.67}/In_{0.33}/As$/GaInAsP/InP tensile-strained quantum-box laser”, Electron. Lett., **30**(1994)142.

[6] N.Kirstaedter et al., “Low threshold, large T_0 injection laser emission from (InGa)As quantum dots”, Electron. Lett., **32**(1994)1416.

[7] D. Bimberg and N. Ledentsov, “Quantum dots: lasers and amplifiers”, J.Phys.: Condens. Matter,**15**(2003)R1063

[8] N.N. Ledentsov, D. Bimberg, “Growth of self-organized quantum dots for optoelectronics application: nanostructures, nanoepitaxy, defect engineering”, J. of Cryst. Growth, **255**(2003)68.

[9] V. Bressler-Hill et al., “Initial stages of InAs epitaxy on vicinal GaAs(001)-(2 x 4)”, Phys. Rev. B, **50**(1994)8479.

[10] A. F. Zhukov, et al., “3.9W CW power from sub-monolayer quantum dot diode laser”, Electron. Lett., **35**(1999)1845.

[11] S. S. Mikhrin, et al., “ 0.94 μm diode lasers based on Stranski-Krastanow and sub-monolayer quantum dots”, Semicond. Sci. Technol., **15**(2000)1061.

[12] A.R. Kovsh et al., “High power lasers based on submonolayer InAs-GaAs quantum dots and InGaAs quantum wells”, Microelectron. J., **34**(2003)491.

[13] I. L. Krestnikov, N. N. Ledentsov, A. Hoffmann and D. Bimberg, “Arrays of two-dimensional islands formed by submonolayer insertions: Growth, properties, devices”, Phys. Status Solidi (a), **183**(2001)207.

[14] B.A. Jorce, D.D. Vvedensky, C.T. Foxon, Handbook on semiconductors, Vol. 3, 1994, p. 275.

[15] J.R. Arther, “Interaction of Ga and As_2 molecular beams with GaAs surfaces”, J. Appl. Phys., **39**(1968)4032.

[16] A.Y. Cho, “Morphology of epitaxial growth of GaAs by a molecular beam method: the observation of surface structures”, J. Appl. Phys., **41**(1970)782.

[17] P. Smilauer, D.D. Vvedensky, “Step-edge barriers on GaAs (001)”, Phys. Rev. B, **48**(1993)17603.

[18] A. Zangwill, et al., “Equations of motion for epitaxial growth”, Surf. Sci. Lett., **274**(1992)L529.

[19] A.K. Myers-Beghton, D.D. Vvedensky, “Nonlinear equation for diffusion and adatom interactions during epitaxial growth on vicinal surfaces”, Phys. Rev. B, **42**(1990) 5544.

[20] M.A. Herman, H. Sitter, *Molecular Beam Epitaxy*, Springer, Heidelberg, 1996.

[21] T. Mattord et al., “Real-time flux monitoring and feedback control of a valved arsenic source”, J. Vac. Sci. and Tech. B, **11**(1993)1050.

[22] C. T. Foxon, “MBE growth of GaAs and III-V alloys”, J. Vac. Sci. and Tech. B, **1**(1983)293.

[23] J. Harris, B. Joyce, P. Dobson, “Oscillations in the surface structure of Sn-doped GaAs during growth by MBE”, Surf. Sci., **103**(1981)L90.

[24] J. Tersoff and F. K. LeGoues, “Competing relaxation mechanisms in strained layers”, Phys. Rev. Lett., **72**(1994)3570.

[25] Goldstein, L., F. Glas, J.Y. Marzin, M.N. Charasse, and G. Le Roux, “Growth by molecular beam epitaxy and characterization of InAs/GaAs strained-layer superlattice”, Appl. Phys. Lett., **47**(1985)1099.

[26] D.J. Eaglesham and M. Cerullo, Phys. Rev. Lett., “Dislocation-free Stranski-Krastanow growth of Ge on Si(100)”, Phys. Rev. Lett., **64**(1990)1943.

[27] Y. W. Mo, et al., “Kinetic pathway in Stranski-Krastanov growth of Ge on Si(001)”, Phys. Rev. Lett., 65(1990)1020.

[28] V. A. Shchukin, D. Bimberg, Rev. Mod. Phys., “Spontaneous ordering of nanostructures on crystal surfaces”, **71**(1999)1125.

[29] H. Saito, K. Neshi, S. Sugou, “Shape transition of InAs quantum dots by growth at high temperature”, Appl. Phys. Lett., **74**(1999)1224.

[30] N.N. Ledentsov, et al., “Quantum-dot heterostructure lasers”, IEEE J.Sel. Top. Quantum. Electron., **6**(2000) 439.

[31] O. Brandt, L. Tapfer, K. Ploog, “Direct synthesis of InAs quantum dots in single-crystalline GaAs matrix by molecular beam epitaxy”, Surf. Sci., **267**(1992)204.

[32] P.D. Wang, et al., “Optical characterization of submonolayer and monolayer InAs structures grown in a GaAs matrix on (100) and high-index surfaces”, Appl. Phys. Lett., **64**(1994)1526.

[33] V.I. Marchenko, “Possible structures and phase-transitions on the surface of crystals”, JETP Lett., **33**(1981)381.

[34] J. Tersoff, R.M. Tromp, “Shape transition in growth of strained islands: Spontaneous formation of quantum wires”, Phys. Rev. Lett., **70**(1993)2782.

[35] V.A. Shchukin, et al., “Vertical correlations and anticorrelations in multisheet arrays of two-dimensional islands”, Phys. Rev. B, **57**(1998)12262.

[36] A.F. Tsatsul’nikov et al., “Lasing in structures with InAs quantum dots in an (Al,Ga)As matrix grown by submonolayer deposition”, J. of Electron. Materials, **28**(1999)537.

[37] H. Schmidt, R. Pickenhain, G. Böhm, “Chemical and structural effects of two-dimensional isovalent substitutions in *A*(III)-*B*(V) semiconductors”, Phys. Rev. B, **65**(2002)45323.

[38] K. Shiraishi and E. Yamaguchi, “Electronic structure of an InAs monomolecular plane in GaAs”, Phys. Rev. B, **42**(1990) 3064.

[39] S. Takagi, “Dynamical theory of diffraction applicable to crystals with any kind of small distortion”, Acta Crysallogr. **15**(1962)1311.

[40] D. Taupin, “Dynamic theory of x-ray diffraction in crystals”, Bull. Soc. Fr. Mineral. Crystallogr., **87**(1964)469 .

[41] A. Krost, F. Heinrichsdorff, D. Bimberg, A. Darhuber, and G. Bauer, “High-resolution x-ray diffraction of self-organized InGaAs/GaAs quantum dot structures”, Appl. Phys. Lett., **68**(1995)785.

[42] D. Pal, E. Towe, and S. Chen, “Characterization of (In,Ga,Al)As/GaAs quantum-dot superlattice structures by high-resolution X-ray diffraction”, Appl. Phys. Lett., **78**(2001)4133.

[43] J. Hornstra and W. J. Bartels,“Determination of the lattice constant of epitaxial layers of III-V compounds”, J. Cryst. Growth, **44**(1978)513.

[44] D. M. Wood and A. Zunger, “Epitaxial effects on coherent phase diagrams of alloys”, Phys. Rev. B, **40**(1989)4062.

[45] O.Brandt, K. Ploog, R. Bierwolf, and M. Hohenstein, “Stability of coherently strained semiconductor superlattices”, Phys. Rev. Lett., **64**(1992)36.

[46] J. E. Bernard and A. Zunger, “Is there an elastic anomaly for a (001) monolayer of InAs embedded in GaAs ? ”, Appl. Phys. Lett., **65**(1994)165.

[47] T. L. Lee, M. R. Pillai, J. C. Woicik, G. Labanda, P. F. Lyman, S. A. Barnett, and M. J. Bedzyk, “Atomic-resolution study of lattice distortions of buried $In_xGa_{1-x}As$ monolayers in GaAs(001”, Phys. Rev. B, **60**(1999)13612.

[48] J.Y. Marzin, J. M. Gérard, A. Izraël, D. Barrier, and G. Bastard, “Photoluminescence of single InAs quantum dots obtained by self-organized growth on GaAs”, Phys. Rev. Lett., **73**, 716(1994).

[49] P.D. Wang, N.N. Ledentsov, and C.M. Sotomayor Torres, “Resonant exciton effect in InAs monolayer insertions in a GaAs matrix”, J. Appl. Phys., **79**(1996)7164.

[50] P.Y. Yu, Manuel Cardona, “Fundamentals of semiconductors”, Springer 19996, p. 368.

[51] R. Heitz et al., “Multiphonon-relaxation processes in self-organized InAs/GaAs quantum dots ”, Appl. Phys. lett., **68**(1996)361.

[52] S. Fafard, et al., " "Phonons and radiative recombination in self-assembled quantum dots", Phys. Rev. B, **52**(1995) 5752.

[53] M.J. Steer et al., "Electronic energy levels and energy relaxation mechanisms in self-organized InAs/GaAs quantum dots", Phys. Rev. B, **54**(1996)17738.

[54] I. Szafranek, M.A. Plano, M.J. McCollum, et al., "Growth-induced shallow acceptor defect and related luminescence effects in molecular beam epitaxial GaAs", J. Appl. Phys., **68**(1990)741.

[55] Z.G. Wang, H.P. Gislason and B. Monemar, " Acceptor associates and bound excitions in GaAs: Cu", J. Appl. Phys., **58**(1985)230.

[56] P. Altier, S. Lozzia, S. Sanguinetti et al., "Resonant quenching of photoluminescence in $In_xGa_{1-x}As/Al_yGa_{1-y}As/GaAs$ self-assembled quantum dots", Materials Science and Engineering B, **88**(2002)252.

[57] P. Altieri, M. Gurioli, S. Sanguinetti, et al., "Competition in the carrier capture between InGaAs/AlGaAs quantum dots and deep point defects", The European Physical Journal B - Condensed Matter, **28**(2002)157.

[58] L. Brusaferri, et al., "Thermally activated carrier transfer and luminescence line shape in self-organized InAs quantum dots", Appl. Phys. Lett. **69**(1996)3354.

[59] D.I. Lubyshev, P. Gonzalez-Borrero, J.E. Marega, et al., "Exciton localization and temperature stability in self-organized InAs quantum dots", Appl. Phys. Lett., **68**(1996)205.

[60] H. Lee, W. Yang, and P.C. Sercel, "Temperature and excitation dependence of photoluminescence line shape in InAs/GaAs quantum-dot structures", Phys. Rev. B, **55**(1997)9757.

[61] Y. Varshni, "Temperature Dependence of the Energy Gap in Semiconductors", *Physica*, **34**(1967)149.

[62] S. Tiwari, *Compound Semiconductor Device Physics*, Academic Press, 1992

[63] V. Wilkinson and A. Adams, "The effect of temperature and pressure on InGaAs band structure", in *Properties of Lattice-Matched and Strained Indium Gallium Arsenide* (P. Bhattacharya, ed.), section 3.2, pp. 70-75

[64] S. Fafard, S. Raymond, G. Wand, R. Leon, D. Leonard, S. Charbonneau, J. Merz, P. Petroff, and J. Bowers, "Temperature effects on the radiative recombination in self-assembled quantum dots", Surf. Sci., **361/362**(1996)778.

[65] Shun Lien Chuang, **"**Efficient band-structure calculations of strained quantum wells", Phys. Rev. B, **43**(1991)9649.

[66] J. Brubach, A.Yu. Silov, J.E.M. Haverkort, et al., "Coupling of ultrathin InAs layers as a tool for band-offset determination", Phys. Rev. B, **59**(1999) 10315.

[67] J.J. Hopfield, "Theory of the contribution of excitons to the complex dielectric constant of crystals", Phys. Rev. **112**(1958) 1555.

[68] G.W. Hooft, W.A. van der Poel, L.W.Molenkamp and C.T. Foxon, "Giant oscillator strength of free excitons in GaAs", Phys. Rev. B, **35**(1987)8281.

[69] L.C.Andriani, F. Tassone, and F. Bassani, "Radiative lifetime of free-excitions in quantum wells", Solid State Com., **77(**1991)641.

[70] B. Deveaud et al., "Enhanced radiative recombination of free excitons in GaAs quantum wells", Phys. Rev. Lett., **59**(1991)2355.

[71] A. Vinattieri et al., "Exciton dynamics in GaAs quantum wells under resonant excitation", Phys. Rev. B, **50**(1994)10868.

[72] D.S. Citrin, “Long intrinsic radiative lifetimes of excitons in quantum wires”, Phys. Rev. Lett., **69**(1992)3393.

[73] G. Wang, S. Fafard, D. Leonard et al., “Time-resolved optical characterization of InGaAs/GaAs quantum dots”, Appl. Phys. Lett., **64**(1994)2815.

[74] A. Kurtenbach, W.W. Ruhle and K. Ebel, “Intrinsic radiative lifetimes of InP/In0.48Ga0.53P quantum dots”, Solid State Com., **96**(1995) 265.

[75] G. Bacher, H. Scheizer, J. Kovac, A. Forchel, H. Nickel, W. Schlapp and R. Losch, “Influence of barrier height on carrier dynamics in strained $In_xGa_{1-x}As$/GaAs quantum wells”, Phys. Rev. B, **43**(1991) 9312.

[76] H. Yu, C. Roberts, and R. Murray, “Exciton recombination dynamics in $In_xGa_{1-x}As$/GaAs quantum wells”, Phys. Rev. B, **52**(1995) 1493.

[77] H. Born, R. Heitz, A. Ho.mann, and D. Bimberg, “Tuned exciton kinetics in self-organized InGaAs/GaAs quantum dots”, Physica E, **13** (2002) 233.

[78] M. Sugawara, “Theory of spontaneous-emission lifetime of Wannier excitons in mesoscopic semiconductor quantum disks”, Phys. Rev. B, **51** (1995)10743.

[79] A.Takeuchi et al., “Time-Resolved study of carrier transfer among InAs/GaAs multi-coupled quantum dots”, Jpn. J. Appl. Phys., **34**(1995)L1439.

[80] J.W. Tomm et al., “Transient luminescence of dense InAs/GaAs quantum dot arrays”, Phys. Rev. B, **67**(2003)45326.

[81] J. Shah, Ultrafast Spectroscopy of Semiconductors and Semiconductor Nanostructures, Solid-State Sciences (Springer-Verlag, Berlin 1999)

[82] A.V. Uskov et al., “Auger carrier capture kinetics in self-assembled quantum dot structures”, Appl. Phys. Lett., **72**(1998)58.

[83] J. Feldmann et al., “Carrier capture into InAs/GaAs quantum dots via multiple optical phonon emission”, J. Appl. Phys., **89**(2001)1180.

[84] B. Ohnesorge, M. Albrecht, J. Oshinowo, A. Forchel, and Y. Arakawa, “Rapid carrier relaxation in self-assembled $In_xGa_{1-x}As/GaAs$ quantum dots”, Phys. Rev. B, **54**(1996)11532.

[85] N.N. Ledentsov, et al., “Self-organized InGaAs quantum dots for advanced application in optoelectronics”, Jpn. J. Appl. Phys., **41**(2002)949.

[86] P.L. Souza and E.V.K. Rao, “Investigation of different Si-related photoluminescence emissions involved in a deep broadband in AlGaAs”, J. Appl. Phys., **67**(1990)7013.

[87] D.J. Bossert and D. Gallant, “Improved method for gain/index measurements of semiconductor lasers”, Electron. Lett., **32**(1996)338.

[88] L.A. Coldren and S. W. Corzine, Diode Lasers and Photonic Integrated Circuits (Wiley, New York), 1995.

[89] F. Klopf, J.P. Reithmaier and A.Forchel, “Highly efficient GaInAs/(Al)GaAs quantum-dot lasers based on a single active laser versus 980 nm high-power quantum-well lasers”, Appl. Phys. Lett.,**77**(2000)1419.

[90] D. Ahn and T.K Yoo, “Theoretical analysis of strained-layer InGaAs/GaAs quantum-well lasers with gain suppression and valance-band mixing”, Appl. Phys. Lett., **60**(1992)548.

[91] B.W. Hakki and T.L. Paoli, “Gain spectra in GaAs double-heterostructure injection lasers”, J. Appl. Phys., **46**(1974)1299.

[92] L. Ketelse, “Simple technique for measuring cavity loss in semiconductor-lasers”, Electron. Lett., **28**(1992)171.

[93] M.V. Maximov, Yu. M. Shernyakov, A.F. Tsatsul’nikov, et al., “High-power continuous-wave operation of a InGaAs/AlGaAs qunantum dot laser”, J. Appl. Phys., **83(**1998)5561.

[94] R. Mirin, A. Gossard and J. Bowers, “Room temperature lasing from InGaAs quantum dots”, Electron. Lett., **32**(1996)1732.

[95] R. Mirin, A. Gossard and J. Bowers, “Characterization of InGaAs quantum dot lasers with a single quantum dot layer as an active region”, Physica E, **2**(1998)738.

[96] E. Herrman, P.M. Smowton, H.D. Summers,J.D. Thomson, and Hopkinson, “Modal gain and internal optical mode loss of a quantum dot laser”, Appl. Phys. Lett., **77**(2000)163.

[97] P.M. Smowton, E. Herrmann, Y. Ning, H.D. Summers, and P. Blood, “Optical mode loss and gain of multiple-layer quantum-dot lasers”, Appl. Phys. Lett., **78**(2001)2629.

[98] F.Y Chang, C. C. Wu, and H.H. Lin, “Effect of InGaAs capping layer on the properties of InAs/InGaAs quantum dots and lasers”, Appl. Phys. Lett., **82(**2003)4477.

[99] P.G. Eliseev, H. Li, A. Stintz et al., “Transition dipole moment of InAs/InGaAs quantum dots from experiments on ultralow-threshold laser diode”, Appl. Phys. Lett., **77**(2000)262.

[100] S. Bognar, M. Grundmann, O. Stier, et al., “Large model gain of InAs/GaAs quantum dot lasers”, Phys. Stat. Sol. (b) **224**(2001)823.

[101] A.E. Zhukov, A.R. Kovsh, S.S. Mikhrin et al., “High external differential efficiency and high optical gain of long-wavelength quantum dot diode lasers”, Physica E, **17**(2003)589.

[102] B. Sumpf, S. Deubert, G. Erbert et al., “High-power 980 nm quantum dot broad area lasers”, Electron. Lett., **39**(2003)1655.

[103] M. Arzberger, G. Bohm, M.C. Amann, and G. Abstreiter, “Gain characteristics of self-assembled InAs/GaAs quantum dots”, Phys. Stat. Sol. (b), **224**(2001)827.

[104] S. S. Mikhrin, A. R. Kovsh, A. E. Zhukov, et al., “6W CW power and 58% conversion efficiency½ of 0.94-μm submonolayer quantum dot laser”, Proceedings of the 26th International Conference on the Physics of Semiconductors (29 July - 2 August 2002, Edinburgh, UK), L2.3.

[105] A. Schonfelder, S. Weisser, J.D. Ralston, and J. Rosenzweig, “Differential gain, refractive index in high speed GaAs-based MQW lasers: Influence of strain and p-doping”, IEEE Photon. Technol. Lett., **6**(1994)891.

[106] P.K. Kondratko, S.L. Chuang, G. Walter et al., “Observation of near-zero linewidth enhancement factor in a quantum-well coupled quantum-dot laser”, Appl. Phys. Lett., **83**(2003)4818.

[107] T.C. Newell, D.J. Bossert, A. Stintz, B. Fuchs, and K.J. Molloy, “Gain and linewidth enhancement factor in InAs quantum-dot laser diodes”, IEEE Photon. Technol. Lett., **11**(1999)1527.

[108] M. Sugawara, K.Mukai, and H. Shoji, “Effect of phonon bottleneck on quantum-dot laser performance”, Appl. Phys. Lett., **71**(1997)2791.

[109] A.V. Uskov, Y. Boucher, J. Le Bihan and J. Mclnerney, “Theory of a self-assembled quantum-dot semiconductor laser with

Auger carrier capture: Quantum efficiency and nonlinear gain", Appl. Phys. Lett., **73**(1998)1499.

[110] D. Bimberg, N. Kirstaedter, N.N. Ledentsov, et. al., "InGaAs-GaAs quantum dot lasers", IEEE J. of Selec. Topics Quantum Electron., **3**(1997)196.

[111] S. Fathpour, P. Bhattacharya, S. Pradhan, and S. Ghosh, "Linewidth enhancement factor and near-field pattern in tunnel injection $In_{0.4}Ga_{0.6}As$ self-assembled quantum dot lasers", Eletron. Lett., **39**(2003)1443 .

[112] L.F. DeChiaro, S. Ovadia, C.J. Sandroff, and L.M. Schiavone, "Recent progress in semiconductor laser reliability and failure analysis", Proceedings LEOS 1993(IEEE, New York, 1993), p.480.

[113] A. Klehr, G. Beister, G. Erbert, et al., "Defect recognition via longitudinal mode analysis of high power fundamental mode and broad area edge emitting laser diodes", J. Appl. Phys., **90**(2001)43.

[114] D. Hofstetter, R.L. Thornton, "Measurement of optical cavity properties in semiconductor lasers by Fourier analysis of the emission spectrum", IEEE J. Quantum Electron., **34**(1998)1914.

List of Publications

(2001.2 ~ 2004.2)

1. **Z. C. Xu**, D. Birkedal, J. M. Hvam, Z. Zhao, Y. Liu, K. Yang, A. Kanjilal and J. Sadowski., " Structure and optical anisotropy of vertically correlated submonolayer InAs/GaAs quantum Dots", ***Applied Physics Letters***, **82**(2003)3859.

2. **Z. C. Xu**, K. Leosson, D. Birkedal, J. M. Hvam, J. Sadowski, Z. Y. Zhao, X. S. Chen, Y. M. Liu and K. T. Yang, " Effect of annealing on the structure and optical properties of InGaAs/GaAs quantum dots", ***Journal of Crystal Growth***, **251**(2003)177.

3. **Z. C. Xu**, K. Leosson, D. Birkedal, V. Lyssenko, J. M. Hvam and J. Sadowski., "InGaAs/GaAs quantum-dot-quantum-well heterostructure formed by submonolayer deposition", ***Nanotechnology***, **14**(2003)1259.

4. **Z. C. Xu**, D. Birkedal, J. Sadowski, V.G. Lyssenko, K. Leosson, I. Magnusdottir, M. v. d. Poel and J.M. Hvam, "Optical properties of submonolayer deposited InGaAs/GaAs quantum Dots", ***ICPS 2002 - 26th International Conference on the Physics of Semiconductors***, paper H160, Edinburgh, Scotland (2002).

5. **Z. C. Xu**, K. Leosson, D. Birkedal, J. Sadowski and J.M. Hvam, "Temperature dependence of photoluminescence from submonolayer deposited InGaAs/GaAs quantum dots", ***NANO-7 - 7th International Conference on Nano-Science and Technology***, paper A2326, Malmö, Sweden (2002).

6. **Z. C. Xu**, K. Leosson, D. Birkedal, J.M. Hvam, J. Sadowski, Z. Y. Zhao, X. S. Chen, Y. N. Liu and K. T. Yang, "Effect of annealing on the structure and optical properties of InGaAs/GaAs quantum Dots", *Tehcnical Digest,* ***MBE XII - 2002 International Conference on Molecular Beam Epitaxy***, pp. 373-374, San Francisco, USA (2002).

7. **Z. C. Xu**, T. Sakamaki, K. Sakai , " X-ray analysis instrument", ***Japan Patent***, P2002-189004A

8. **Z. C. Xu,** "Analysis instrument of Samples ", ***Japan Patent***, P2001-272361.

9. J. Sadowski, D. Hrabovsky, E. Vanelle, **Z. C. Xu** and J. Kanski, "Magnetic and optical properties of InGaMnAs quantum dot structures", ***2nd International Conference on Physics and Application of Spin-Related Phenomena in Semiconductors***, paper PII, p.22, Würzburg, Germany (2002).

10. H. Matsueda, K. Lesson, **Z. C. Xu**, J. M. Hvam, Yann Ducommun, Arno Hartmann, Eli Kapon, "Dynamic dipole-dipole interactions between excitons in quantum dots of different sizes", Submitted to ***IEEE Journal of Quantum Electronics***, 2004.

11. **Z. C. Xu**, et al., "Sub-monolayer InGaAs/GaAs Quantum-dot Lasers with High Modal Gain and Zero Linewidth Enhancement Factor", Submitted to ***Appl. Phys. Lett***., 2004

Curriculum Vitae

Zhangcheng Xu was born in Anhui, China, on Nov. 14, 1970. He received his BSc (1992) and MSc (1995) in Physics, from Department of Physics, Anhui University, Hefei, China. From May 1995 to August 1996, he worked on "Synchrotron Radiation x-Ray Dynamical Diffraction", as a research assistant at Department of Electric Engineering, Saitama Institute of Technology, Saitama and at Photon Factory, National Institute of High Energy Physics (KEK), Tsukuba, Japan. In July 1998, he received the Doctor of Engineering Degree in Inorganic and Non-metal Materials, from Shanghai Institute of Ceramics, Chinese Academy of Sciences, Shanghai, China, for the work on "Resonant x-Ray Dynamical Diffraction and its Application in Material Sciences". He was awarded the "Excellent Prize" from the president of Chinese Academy of Sciences in November 1998. From August 1998 to January 2001, he worked on x-ray detectors and analysis instruments, as a postdoctoral engineer at JEOL (a world leader in electron optics), Akishima, Tokyo, Japan. From February 2001 to March 2004, he worked on "MBE Growth and Characterization of Self-assembled Semiconductor Quantum Dots", as a PhD student at Research Center COM (Communication, Optics and Materials), Technical University of Denmark, Lyngby, Denmark. The MBE growth was carried out at III-V Nanolab, Niels Bohr Institute, Copenhagen University, Copenhagen, Denmark. From April 2004, he is working on "Fundamental Studies of Thin Film Growth and Etching", as a postdoctoral research associate at Department of Physics, University of Vermont, in Burlington and at Brookhaven National Laboratory in NewYork, USA. Email: xuzhch@yahoo.com.cn